Investigation of Particle Trajectories and Flow Patterns in a Hydrocyclone by Positron Emission Particle Tracking (PEPT)

Åshild Skorpen

Master Thesis in Process Technology, Multiphase Systems (M.Sc.)

Department of Physics and Technology
University of Bergen

June 2012

Acknowledgements

First I would like to thank my supervisor Professor Alex C. Hoffmann for his help and guidance throughout the thesis. I would also like to thank Ph.D. student Yu-Fen Chang for good discussions and cooperation through the thesis. She was also very helpful with the execution of the experiments.

I am very grateful for the work of the staff at the radiology department at Haukeland University Hospital who operated the PET camera when we were carrying out our experiments. Especially thanks to Chief Radiochemist Ph.D. Tom Christian Adamsen who labelled the tracer particles. Their work was essential for the execution of the experiments for the thesis and are highly appreciated.

I would also like to thank my fellow master students at the University of Bergen. The discussions on CFD simulations and other subjects, and the good working environment were highly appreciated. Thanks to Karoline Sønnesyn for proofreading this thesis.

Last I would like to thank my boyfriend Oddgeir Randa Heggland for his love and support throughout the master. I am very grateful for his effort in reviewing this thesis. I would also thank the rest of my family for support and encouragement throughout my studies.

Abstract

Cyclone separators are widely used for separation of solids or droplets from gaseous or liquid fluids in several industries. Cyclones can be used for many purposes and each cyclone can be fitted to its area of use. In the oil and gas industry there are problems with too much sand in the produced oil. Separation of the solids are critical for other separation and processing equipment and when concerning the environment effective hydrocyclones are very important.

The purpose of this thesis is to investigate particle trajectories in a hydrocyclone to achieve a better understanding of the particle flow. A *Positron Emission Tomography* (PET) scanner and a technique called *Positron Emission Particle Tracking* (PEPT) are used to detect the trajectories. The PET scanner is placed at Haukeland University Hospital and is originally used to detect cancer cells in patients.

In this thesis the PET scanner is used to track particle behaviour in a hydrocyclone which is done by making the particle radioactive and injecting it into the hydrocyclone. Based on cross-triangulation of *lines of response* (LOR) obtained from the output of the PET camera, the particle trajectory can be followed throughout the hydrocyclone. The use of this technique makes it possible to see details in the particle trajectory, and hence discover flow abnormalities and trends connected to the operating settings. The PEPT technique has been developed over twenty years and is currently used for process technology research just a few places in the world.

Some numerical simulations has been performed to supplement the experimental results, rather than to perform a detailed comparison of the experiments.

The detailed particle trajectories obtained in this thesis show a flow abnormality appearing in almost all the experiments. The flow phenomenon *end of vortex* (EoV) is also present in some of the experiments. The numerical simulations of the experiments coincide well with the experimental results. Additionally the Burgers model of flow gives good results when fitted to the tangential velocity of the particle.

Contents

List of Figures

List of Tables

Nomenclature

Abbreviations

CAD	Computer-aided design
CT	Computed tomography
CFD	Computational fluid dynamics
CS	Control surface
EoV	End of vortex
FOV	Field of view
GEC	Grade-efficiency curve
HSMA	High-speed motion analyser
LDA	Laser-Doppler anemometry
LDV	Laser-Doppler velocimetry
LES	Large eddy simulation
LOR	Line of response
LSO	Lutetium Oxyorthosilicate
PIV	Particle image velocimetry
PEPT	Positron emission particle tracking
PET	Positron emission tomography
RANS	Reynolds-averaged Navier-Stokes
URANS	Unsteady Reynolds-averaged Navier-Stokes

Greek symbols

α	Alpha particle
β^+	Positive beta particle
β^-	Negative beta particle

$\Delta\rho$	Density difference between particle and fluid
Δp	Pressure drop
Γ	Circulation
λ	Wavelength
μ	Viscosity
η_T	Total separation efficiency
$\eta_T{}'$	Reduced total separation efficiency
$\bar{\nu}$	Antineutrino particle
ν	Kinematic viscosity
ν	Neutrino particle
η_x	Separation efficiency
Ω	Angular velocity
ρ	Density
θ	Angular coordinate in a cylindrical coordinate system
ρ_p	Density of the particle

Symbols

a	Inflow gradient
A_0	Amount of initially present activity
A_t	Amount of activity present after a time interval
a	Acceleration
C	Constant
c	Parameter in the Burgers equation
c	Speed of light
D	Diameter of the cyclone body
D_x	Diameter of the vortex finder
E	Energy
F_c	Centrifugal force
F	Force
H_{CS}	Height of the CS

k	Decay constant
m	Mass of the particle
M_c	Mass flow rate of collected underflow
M_e	Mass flow rate of emitted overflow
M_f	Mass flow rate of the feed
n	Parameter depending on the roughness, geometry and particle in the cyclone
Q	Volumetric flow rate
Q_{feed}	Volumetric feed rate
$Q_{underflow}$	Volumetric underflow rate
r	Radial coordinate in a cylindrical coordinate system
r	Radius
Re	Reynolds number
re	Viscous radius
R_f	Volumetric underflow to feed ratio
Stk	Stokes number
Stk_{50}	Stokes number at 50% separation efficiency
t	Time
$t_{\frac{1}{2}}$	Half-life
v	Velocity
v_{in}	Inlet velocity
v_{rCS}	Average radial velocity in CS
v_{ch}	Characteristic velocity
v_r	Radial velocity
v_θ	Tangential velocity
v_z	Axial velocity
x	Particle diameter
x_{50}	Cutsize
z	Axial coordinate in a cylindrical coordinate system

Chapter 1

Introduction

1.1 Relevance

There are big challenges in the oil and gas industry regarding excessive amounts of sand and other solid particles in the produced oil and gas. Increased oil recovery has made the reservoirs produce oil much longer than what was expected when the production started decades ago. This leads to more solids in the produced oil and water. Preserving the environment has become increasingly important in recent years and there are strict rules for waste discarded to sea. The laws will probably become stricter over the years as the environment, and how to take care of it, comes more and more into focus. It is therefore fundamental to have good processes for separation of solids from oil and water. Knowledge about the separation processes is important to improve the equipment and to know what equipment to use at each stage of the separation process.

In this thesis the trajectory of a solid particle in a hydrocyclone have been investigated. It is not easy to obtain particle tracks through a high-speed flow field but by use of the Positron Emission Particle Tracking (PEPT) technique the trajectories can be studied. Knowledge about the particle trajectory in equipment is a limited but important field to investigate. The particle track obtained can detect flow abnormalities and help improve the hydrocyclones separation efficiency.

1.2 Background

Sand and solids can create many problems in the producing, separating and processing equipment and are therefore unwanted. To achieve sufficient oil quality separation of solids from oil and gas is important, cyclones are among other separation equipment used for the separation. Cyclones are applied in the process technology to separate compounds with different density by use of the centrifugal force.

A cyclone has no moving parts and is only driven by an external pump, it is also cheap and compact. A cyclone separator is easy to maintain, have a simple construction and is versatile. This makes cyclones advantageous compared to scrubbers, filters and settlers [1]. Cyclones especially designed for liquid components are called hydrocyclones.

As mentioned can sand and other solid particles cause many problems in the producing, separating and processing equipment, in addition to the environmental issues. Some examples of these problems are listed below:

- Solids in process equipment can cause erosion which reduce the lifetime of the equipment.
- Solids may interfere with controls and instruments which can reduce reliability and safety in the process.
- Clogging of valves can cause reduced capacity, reliability and safety.
- Solids can create problems with injection pumps and injection wells.
- Solids fill up the separation tanks which cause the particle to spend more time through the equipment, prolonged residence time. This will eventually cause a need for manually removal of the solids.

1.2.1 Application in the Industry

Cyclones come in many sizes and shapes and can easily be adapted to each individual separation process. They are therefore widely used in several types of industries. Oil and gas industry, iron and steel industry, sand-, cement- and coking plants, and grain processing facilities are some of the industries where cyclones are used extensively [2]. Cyclones are normally continuously operated with the collected particles removed at all times while new feed are lead into the cyclone. This type of equipment is often cheaper to operate than other separation equipment such as filters. [3].

Hydrocyclones can also be used to produce thick underflows (thickening) and for solid-solid separation. When used for thickening the hydrocyclone cannot be used for separation simultaneously. Hydrocyclones can typically achieve underflow concentrations of 50 volume% or more. When used for solid-solid separation the particles are separated by particle size and the solids of the feed can be split into fine particles and coarse particles. Hydrocyclones can also be used to improve the performance of other filtration or separation systems [3].

1.2.2 History of Cyclones

In 1885 the first patent for a cyclone was granted to John M. Finch. The cyclone was based on the same principle as today's cyclones except the dust was allowed out on the side of the cylindrical body instead of the conical shaped bottom. The idea of using centrifugal force to separate particles from a gas or liquid, rather than gravity, was unconventional and quite radical back in the late 1800's. The design was improved over the years that followed and in the early 1900's conical cyclones appeared as we know them today. Cyclones were at the beginning mostly used in mills for processing grain and wood products.

Cyclones continued to grow in popularity due to low manufacturing cost, no moving parts, simple construction, and relatively easy maintenance. Cyclones have now found a place in every industry that needs to separate solids form gas or fluids and the cyclone is an important part of the separation process in today's oil industry.

Cyclone design and operation fields have changed over the years, and it has been preformed numerous investigations in both fields that have resulted in significant improvements. Today the cyclone is used in many different industries and comes in different sizes and shapes defined by the area of use [2].

1.3 Previous Work

This thesis continues the work and research of the *Solid Separation from Highly Viscous Liquids by Cyclone Technology (CLEANSAND)* project. A collaboration project between the University of Bergen and Aker Kværner Process Systems (AKPS) from 2008 to 2011. Several master theses have been written, and one Phd. student have been working on this project the entire period. Several articles have also been published.

The experimental equipment, built by the workshop at the physics department at University of Bergen, is therefore already active and well tested.

Earlier master students have focused on different parts considering the particle trajectory in the cyclone, although all experiments have been done on the same rig. First the focus was mostly concerning the function of the rig and to investigate the possibilities to achieve good trajectories. A few experiments were preformed and it was proved that the results gave good experimental data on particle trajectories by use of the Positron Emission Particle Tracing (PEPT) technique.

Several improvements on the rig were done later in the project. Two ultrasound flow meters, a larger tank and larger hoses were installed. There were preformed many experiments with several different viscosities, adjustments of the underflow and different feed which gave good results.

In this thesis some of the material found in the earlier work have been put into use. Some of the experimental data was done in cooperation with a previous master student in the spring of 2011.

1.4 The Thesis

Both experimental work and numerical work have been carried out in this thesis. The focus of the thesis is to investigate the flow pattern of a particle in a high-speed flow field through a hydrocyclone. This is done by the PEPT technique which has enabled tracking of a single solid particle through the flow. The trajectories give a better understanding of the separation in hydrocyclones. Flow abnormalities in the particle flow can be discovered and problematic areas of the hydrocyclone can be detected. There have also been done some numerical simulations to supplement the experimental results more than being a total comparison of the results.

- In Chapter 2, Theory, the basic theory and the fluid dynamics aspects concerning the cyclone is discussed.

- In Chapter 3, Positron Emission Particle Tracking, are radiation and the principles of the PET scanner and the PEPT technique discussed.

- In Chapter 4, Literature study, a short review of the work on subjects concerning this thesis is presented. Research done in areas such as experimental and numerical investigation of the flow in cyclones and other research involving the PEPT technique is presented.
- In Chapter 5, Experimental Method and Analysis, the procedure of the execution of the experiments are presented as well as how to analyse the results.
- In Chapter 6, Computational Fluid Dynamics, a small introduction to numerical simulation is given as well as the set-up for the simulations executed in this thesis.
- In Chapter 7, Results and Discussion, are the results from the experiments along with CFD simulations presented and analysed. The results are discussed and the sources of error is presented.
- In Chapter 8, Conclusion, the conclusion of the thesis is presented.
- In Chapter 9, Suggestions for Further work, suggestions for further work on this thesis are discussed.

This thesis is written as scientific work and it is therefore an advantage for the reader to have basic knowledge about process technology, fluid dynamics and multiphase systems. It also requires some knowledge in the fields of mathematics, physics and chemistry.

Chapter 2

Theoretical Background for the Cyclone

In this chapter the theory concerning the cyclone is looked at in more detail. The forces acting on fluid elements in swirling flow is discussed. Different types of cyclones and how the cyclone work is also presented. Models of the flow in the cyclone and how particles move in the flow are discussed in detail. The separation efficiency and pressure drop in the cyclone are also among the topics in this chapter.

2.1 Forces in a Swirl Flow

2.1.1 Centripetal Force

To describe the forces acting on a fluid element in a swirling flow consider a cylindrical coordinate system (r, θ, z) fixed in space with the axis of rotation, z-axis, pointing out of the paper. The element accelerates toward the center as it rotates. This acceleration is called the centripetal acceleration, Figure 2.1. If the element did not accelerate it would continue in a linear path tangent to the orbit toward the axis of the rotation [2]. This means that there are velocity changes due to the acceleration, which indicate that there is a force acting towards the center. This force is known as the centripetal force.

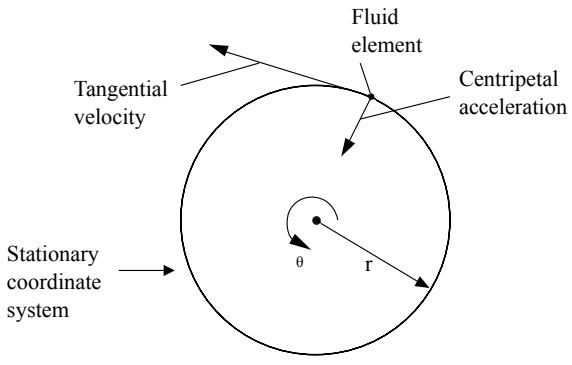

Figure 2.1: Centripetal force in a fixed coordinate system adapted from [2]. The element accelerate as it rotate toward the center. Velocity changes due to the acceleration indicates that there is a force acting towards the center, this force is called centripetal force

2.1.2 Centrifugal Force

If the element is considered from a coordinate system that is not fixed in space but rotating with the element, the centripetal acceleration can no longer be observed but will appear as an apparent force directed away from the axis of rotation. This is known as the centrifugal force. The centrifugal force, F_c, acts away from the rotating axis and is similar to gravity. The magnitude of the force is equal to the mass of the element times the centripetal acceleration, Equation (2.1) [2], where r is radius, v_θ is the particles tangential velocity, and m is the mass of the particle,

$$F_c = mv_\theta^2/r. \tag{2.1}$$

2.2 The Centrifugal Separator - The Cyclone

Mass forces acting on particles due to an internal or external field of acceleration is the base of separation in centrifugal separators. The field of acceleration that separates the particles and the fluid in centrifugal separators, called cyclones, is the centrifugal force. For separation to take place in a cyclone there must exist a density difference between the fluid and the particles [3].

2.2.1 Cyclone Types

Cyclones come in several different shapes and geometries specially designed for their area of use. The separated fluid and the geometry of the cyclone body and inlet are the main differences of the cyclone types.
The two main types of cyclones are:

- Cyclone
- Swirl tubes

In a cyclone the swirl motion is created by how the flow stream is lead into the cyclone, the most common is the tangential inlet. A cyclone with main fluid of air or gaseous solution and dispersed phase of particles or droplets, is called a cyclone. Cyclones with liquids, e.g. water, as its main fluid are called hydrocyclones. A hydrocyclone has been investigated in this thesis. Since it is just the fluid that different between a cyclone and a hydrocyclone, ergo no geometrical differences, they share the same theory and will be discussed as one.

In the swirl tubes, however, the swirling motion is not created by how the fluid is lead into the separation body (tangential inlet), but is created by swirl vanes at the top of a cylindrical section (axial inlet). Hence, some of the theory for the cyclones/hydrocyclones and the swirl tubes are different. In this thesis the swirl tubes are not of interest and are therefore not discussed.

2.2.2 How Cyclones Work

The cyclone body is divided into two parts, a cylindrical and a conical. The cylindrical section is placed on top of the conical section, which is also called a cylinder-on-cone

cyclone. The cylindrical section is closed at the top with an overflow pipe coming out, which is also called the vortex finder. The end of the vortex finder is located some distance into the cyclone body where it stabilizes the inner vortex and shields it from the high inlet velocity.

The conical and cylindrical sections are joined together, Figure 2.2. The underflow is lead out of the cyclone and into the underflow box through the bottom of the cyclone. The underflow carries most of the solids separated out of the cyclone. On the upper level of the cylindrical section there is a rectangular inlet, Figure 2.2. By leading the flow into the cyclone tangentially to the cyclone body the swirling motion is produced [4].

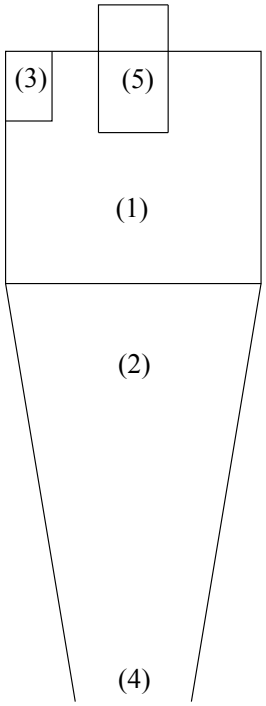

Figure 2.2: Sketch of a cyclone body: (1) Cylindrical section, (2) conical section, (3) inlet, (4) underflow, and (5) vortex finder

The swirl motion is created when a fluid enters the cyclone inlet under pressure [5]. The fluid moves axially downwards in the outer vortex in the cylindrical section of the cyclone. As it moves into the lower part of the conical section, the fluid is forced into the inner vortex which moves axially upwards, and exits through the vortex finder (the overflow). The particles in the fluid are flung out to the wall in the cylindrical section and stays in the downward outer vortex through the conical section until they exit through the underflow, Figure 2.3. This kind of cyclone is called a reversed-flow cyclone [2].

The particles suspended in the fluid are separated due to size and specific gravity (density). The swirl flow creates a vortex in the cyclone that give rise to a low pressure zone along the vertical axis, called the inner vortex. The vortex flow in the cyclone consists of two vortices; one downward outer region and one inner upward region, Figure 2.3. Stokes law tells us that heavy fast settling particles move to the wall of the cyclone and follow the flow out through the underflow. The lighter and slower settling particles move into the low pressure zone in the center of the cyclone, and follow the overflow up

along the axis and exit through the vortex finder [6]. This proves that gravity does not significantly affect the separation in cyclones, except in large cyclones used to separate large particles, it is the flow itself. Hence the cyclones do not need to be operated in vertical position.

It is common to talk about two flow vortices in a cyclone, an inner and an outer vortex, but there are no permanent boundary between the two vortices. This means that the particles and fluid transfer from inner to outer vortex due to turbulence at all lengths through the cyclone body [7].

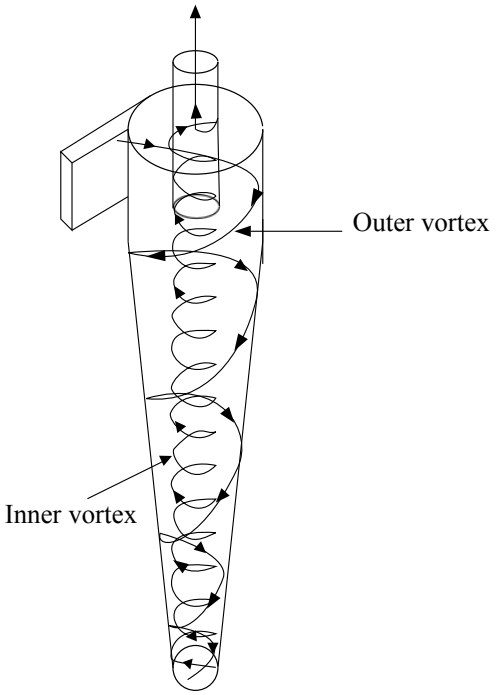

Figure 2.3: Sketch of the two flow patterns in a reversed-flow cyclone adapted from [8]. The inner upward directed vortex pass out through the vortex finder. The outer downward directed vortex pass out through the underflow.

2.3 Models of the Vortex Flow

The vortex flow in a cyclone consist of three velocity components; radial, tangential and axial velocity. In swirling flow the tangential velocity, v_θ, is the most important of the three velocity components. Hence the flow in cyclones is described by models of the tangential velocity. There are several different models for describing a swirling flow and in this thesis the Rankine model and the Burgers model are in focus.

2.3.1 Rankine Model

The equations for tangential velocity distribution in a swirling flow can be divided into two types of ideal flow:

1. "Forced vortex flow" which is the same as solid body rotation with a constant angular velocity in the radial direction.

2. "Free vortex flow", also called loss free rotation. In such a vortex the moment-of-momentum of fluid elements is constant in the radial direction [2].

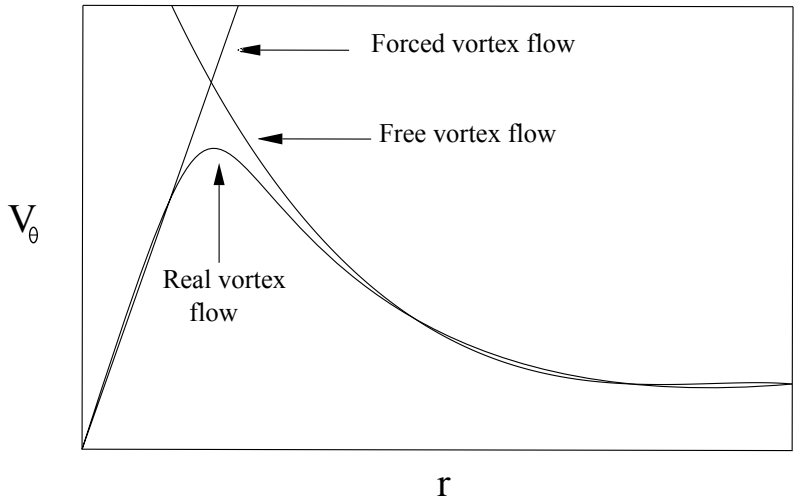

Figure 2.4: The Rankine vortex model consists of two ideal vortex flows, a forced vortex flow and a free vortex flow. This is an illustration of the two ideal vortex flows and a real vortex flow adapted from [2]

In the forced vortex flow the swirling fluid is assumed to act like a solid body. This means that the fluid elements at all radial positions, r, have the same angular velocity, Ω, and therefore follow a straight line drawn by Equation (2.2), Figure 2.4,

$$v_\theta = \Omega r. \tag{2.2}$$

In the free vortex flow the fluid elements are assumed to have no viscosity which means that the fluid elements act like the flow. If an element in this case moves to a smaller radius, the moment-of-momentum will be conserved, and the tangential viscosity will increase. This is described by Equation (2.3) and can be seen in Figure 2.4,

$$v_\theta = \frac{C}{r}, \tag{2.3}$$

where v_θ is tangential velocity, C is a constant, and r is radial position. The tangential velocity distribution in a real swirling flow is an intermediate flow between the ideal forced vortex flow and the free vortex flow. In a real swirling flow there is normally a region of near loss-free rotation surrounded by a core of near solid-body rotation, which can be seen in Figure 2.4. This model is called a Rankine vortex. The two Equations (2.2) and (2.3) can be combined to one equation that almost follows the real swirling flow [9], Equation (2.4).

$$v_\theta = \frac{C}{r^n}, \tag{2.4}$$

where n is depending on roughness and geometry of the cyclone and the concentration of particles. The value of n normally varies between 0.5 and 0.8 [9]. Equation (2.4) can

be used for free and forced vortex flow as well. In the outer region near the wall n is close to 1 and in the inner region near the cyclone axis n is close to -1 [8].

2.3.2 Burgers Model

In the Burgers model the viscosity of the fluid is taken into account, which makes it possible to smooth the peculiarities that appear in the vortex core in the Rankine model. The model was developed from the Lamb vortex to describe a three-dimensional steady-state Burgers vortex of turbulent swirl flows, by Burgers (1940, 1948) and Rott (1958) [10].

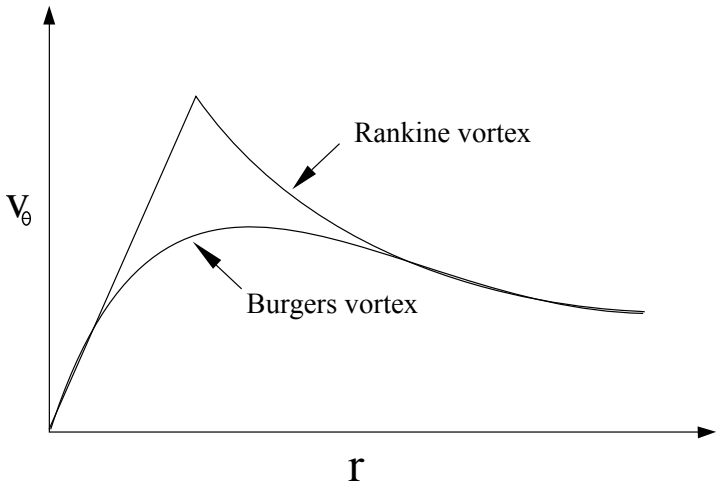

Figure 2.5: Sketch of the Burgers vortex and the Rankine vortex. The differences between the two models of the flow are clear from this illustration

The Burgers equation (2.5), [10] gives the tangential velocity, v_θ, as a function of the radial position in the cyclone.

$$v_\theta = \frac{\Gamma}{2\pi r}\left[1 - exp\left(-\frac{ar^2}{4\nu}\right)\right], \Gamma = \Gamma|_{r=\infty}, \tag{2.5}$$

where Γ is the circulation, r is the radius of the cyclone body, a is the *inflow gradient*, and ν is the kinematic viscosity of the fluid. The circulation, Γ, in the cyclone can be approximated by Equation (2.6), where r is the radius and v_{in} is the inlet velocity in the cyclone,

$$\Gamma = 2\pi r v_{in}. \tag{2.6}$$

To simplify Equation (2.5) a viscous radius, re, is found [11]. It is determined by the inflow-gradient, a, and the kinematic viscosity, ν, Equation (2.7),

$$r_e = \sqrt{\frac{2\nu}{a}}. \tag{2.7}$$

Another parameter is developed, parameter c. The c comes from Equation(2.8) which is developed from the equation for circulation (2.6) and the Burgers equation (2.5).

$$\Gamma = rv_{in} = c \tag{2.8}$$

By substitution of Burgers Equation (2.5) with the equation for circulation, Equation (2.6), and the equation for viscous radius, Equation (2.7), the simpler Burgers Equation (2.9) is produced,

$$v_\theta = \frac{c}{r}\left(1 - exp\left(-\frac{r}{re}\right)^2\right). \tag{2.9}$$

Equation (2.7) is plotted in Figure 2.6 where $c \to 1$ and $re \to 1$. When the simpler Burger Equation (2.5) and the original Burgers Equation (2.9) is compared it is clear that the circulation, Equation (2.6), is equivalent to the parameter c, Equation (2.8). Hence c can replace Γ in Equation (2.9).

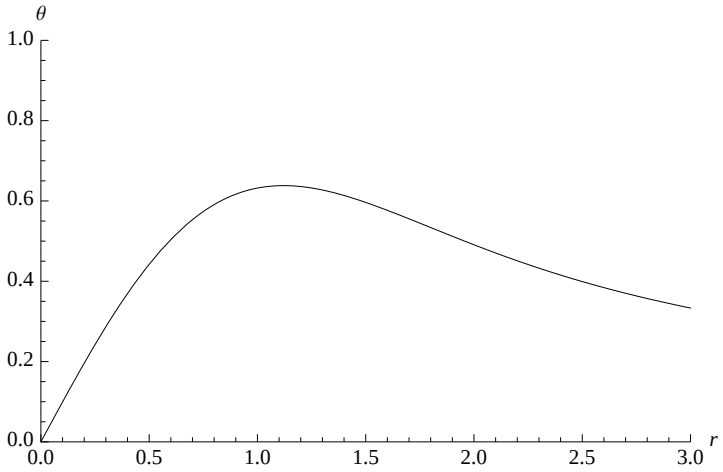

Figure 2.6: Plot of the tangential velocity by the Burgers equation (2.9), where $c \to 1$ and $re \to 1$

2.4 Flow Pattern

Flow pattern in cyclones is described by velocities i three directions; the radial, tangential, and axial velocity. In cyclones the velocity distribution in the near-wall region and in the control-surface (CS) are the most important. CS is the imaginary cylindrical surface made when continuing the vortex finder all the way to the bottom of the cyclone body, Figure 2.7. The velocity distribution is used for modelling the flow pattern in the cyclone.

2.4.1 Radial Velocity, v_r

Compared to the two other velocity distributions, tangential and axial velocity, the radial velocity is small. Velocities in the radial direction give the solid particles resident time, so the cyclone can separate them from the fluid. The radial velocity is a function of the axial velocity and the geometrical parameters of the cyclone. Radial velocity is neglected

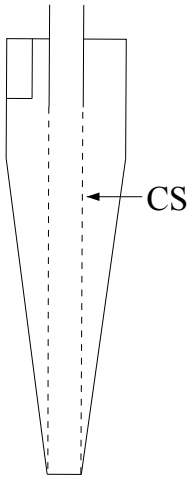

Figure 2.7: Illustration of the control surface, CS, in a cyclone adapted from [2]

near the wall and is assumed uniform in the control surface. This means that the radial velocity can be calculated in CS by Equation (2.10),

$$v_{rCS} = \frac{Q}{\pi D_x H_{CS}}, \tag{2.10}$$

where v_{rCS} is average radial velocity in CS, D_x is the diameter of the vortex finder, the diameter is also diameter over CS, Figure 2.7, Q is volumetric flow rate and H_{CS} is the height of the CS.

There is not enough information about the radial velocity to illustrate it graphically. Radial velocity is also difficult to measure accurately and is generally much smaller than the tangential velocity. The radial velocity is not uniform in reality because just below the vortex tube there are always some *lip leakage*. Lip leakage means that some fluid goes straight up through the vortex finder right after entering the cyclone, which is one reason for non ideal grade-efficiency curves [2], Section 2.6.3.

2.4.2 Tangential Velocity, v_θ

The drive force in centrifugal separation is the tangential velocity. As the radius decrease through the cyclone body the tangential velocity distribution will change due to conservation of momentum. At a given radius the tangential velocity will be constant for frictionless flow.

In real cases the tangential velocity will decrease as the fluid moves down the cyclone, Figure 2.8. When modelling the flow pattern in a cyclone the tangential velocity is the most important component. The tangential velocity can be modelled by many different models, e.g Rankine and Burgers model.

2.4.3 Axial Velocity, v_z

The axial velocity is directed downwards in the outer region and upwards in the inner region of the cyclone, Figure 2.9. The axial velocity makes the flow of particles to the wall and down through the underflow possible, and provides lighter particles/fluids to

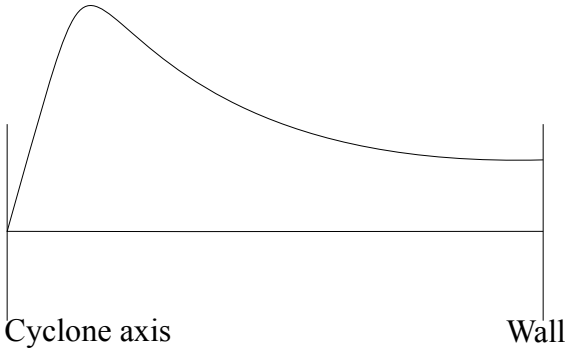

Figure 2.8: Illustration of radial distribution of the tangential velocity in a cyclone adapted from [2]

move to the middle of the cyclone and up through the vortex finder [6]. In Figure 2.9 the crossing of the x-axis represents the fluid crossing over from inner to outer vortex. The outer region of the downward flow are separated from the upward flow by the control surface. The axial velocities in each region are assumed to be uniform over the cross section. This together with the equation for v_r, Equation (2.10), allows calculation of the axial velocity from simple geometrical considerations [2].

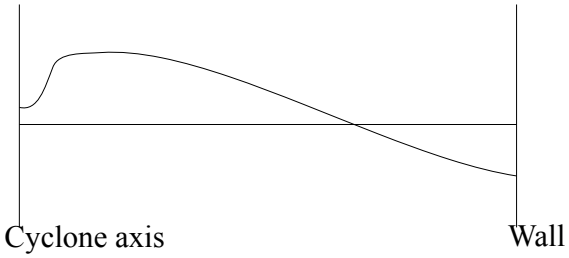

Figure 2.9: Illustration of the radial distribution of the axial velocity in a cyclone adapted from [2]. At the crosspoint of the x-axis the fluid cross from inner to outer vortex flow in the cyclone

2.4.4 Locus of Zero Vertical Velocity

In the cyclone one flow is going upwards, the inner vortex, and one flow is going downwards, the outer vortex [12]. The two flows move in opposite vertical directions, and hence there is a position between the two flows where there is no vertical velocity. The locus of zero vertical velocity can be traced and is assumed to be equal to the surface CS as seen in Figures 2.7 and 2.11 [9].

2.4.5 The End of Vortex

The end of vortex (EoV) is a flow abnormality which occurs in the flow pattern low in the conical section. The inner vortex core bends to the wall in the conical section instead of going straight to the bottom of the cyclone, as illustrated in Figure 2.10. A weaker

secondary induced vortex, which goes all the way down to the collection box, is created below the EoV. The EoV phenomenon depends on the operating conditions and does not always occur.

The EoV influence the separation effect and can cause clogging. The phenomenon is therefore important to the separation performance of the cyclone [13]. When the core attaches to the wall it turns around at the same place at the inner wall. As the EoV circulates at the the wall, hard solids will cause damage to the inner wall which can cause localized erosion or depositions on the wall and significantly shorten the lifetime of the cyclone.

The EoV swirl with intense velocity and "collected" particles around the wall can be recycled back into the inner vortex causing significant influence on the separation performance. When an EoV occurs the whole effective length of the cyclone is not utilised and the separation performance is reduced with more than the shortened length of the cyclone [2].

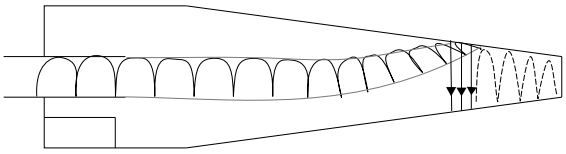

Figure 2.10: Illustration of the end of vortex phenomenon adapted from [2]. The core vortex bend to the wall some place in the conical section of the cyclone, attach and turns around at the same place at the wall. The EoV may cause erosion and depositions at the wall which can shorten the lifetime of the cyclone

2.5 Motion of Particles

Particles in a swirling flow move with a terminal velocity relative to the fluids movement in the flow. The terminal velocity determines if the particle is collected or lost. The terminal velocity is equivalent to a particle settling under steady-state conditions in the earth's gravitational field, except that in a cyclone the gravitational field is replaced by a radial directed centrifugal force field. Calculation of the terminal velocity for a particle in a cyclone is therefore interesting. Newton's law for a particle moving in a flow field is the mass times acceleration and the sum of forces acting on the particle, Equation (2.11),

$$\begin{pmatrix} mass \\ \times \\ acceleration \end{pmatrix} = \begin{pmatrix} body \\ force \end{pmatrix} + \begin{pmatrix} fluid \\ drag \end{pmatrix} + \begin{pmatrix} unsteady \\ force \\ terms \end{pmatrix}, \tag{2.11}$$

where the body force is normally due to gravitational field or centrifugal force. The term centrifugal force is as mentioned not a real force. Hence the above force balance is performed in a reference coordinate system rotating with the particle. The unsteady force terms accounts for the acceleration of the particle relative to the fluid and the fluid drag accounts for the drag of the particle as it moves with steady velocity relative to the fluid [2].

Due to intensive turbulent mixing in the inlet of the cyclone particles who enters the cyclone near the wall can be dispersed inwards. The main separation is thought to be in the conical section and information on the flow pattern in the cylindrical section of the cyclone is therefore limited [12].

When a particle enters the separation space in the cyclone the particle is influenced by an outward directed centrifugal force and an inward directed drag force. At the point where the incoming fluid starts to experience rotation and the solids first experience centrifugal force directed radially outwards, the separation space in the cyclone starts [2].

When describing how particles are influenced by the rotational flow pattern the size of the particle is very important. The centrifugal force is proportional to the mass of the particle and also the cube of the diameter of the particle, Equation 2.12.

$$m = \rho_p \times \frac{\pi}{6} \times x^3, \tag{2.12}$$

where m is the mass of the particle, x is diameter, and ρ_p is the density of the particle.

The drag force which is due to the flow of fluid from outer to inner vortex is proportional to the diameter of the particle when Stokes law applies. In practice Stokes law does often apply and for that reason are the large particles easier to separate.

2.6 Separation Efficiency

When the feed concentration is increased the separation efficiency falls rapidly. Cyclones where high total mass recovery is wanted are therefore, operated with dilute feed concentration [4]. Highest separation efficiency in the cyclone body is found in the outer vortex. Due to high swirling motion solids and particles will be flung out to the wall and follow it down and out trough the underflow. Some of the solids are too small and too light to be flung out to the wall, and will therefore be thrown into any part of the vortex by the turbulence in the flow.

In the center of the vortex low rotating movements lead to low separating power. Most of the small particles that enter this region will follow the fluid out through the overflow. Hence complete collections of solids with smaller particles than those entirely deposited by the outer vortex are unlikely [7].

The efficiency of the cyclone is measured by the fraction of solids separated and the pressure drop. As the solids move to the wall of the cyclone by centrifugal force the drag forces counteract the centrifugal forces. The size and shape of the solid particles and the turbulent intensity of the flow are factors that the drag force is dependent of. The centrifugal force is therefore eliminated by drag force and turbulent diffusion for small particles. Small particles flow in a similar flow as water and the ratio of these particles are the same in the underflow and the overflow. The larger solid particles are moved to the wall by centrifugal force and flow out through the underflow [5].

2.6.1 Total Efficiency

The ratio of total mass collected in the underflow to the total particle mass in the feed is the total separation efficiency in the cyclone, Equation (2.13). The flow rates through

the exits, underflow and overflow, are not taken into account in the total separation efficiency which makes it a poor way to measure the efficiency [4].
Total separation efficiency η_T is given by Equation (2.13),

$$\eta_T = \frac{M_c}{M_f} = 1 - \frac{M_e}{M_f} = \frac{M_c}{M_c + M_e}, \tag{2.13}$$

where M_f is mass flow rate of the feed, Mc is mass flow rate of collected underflow, and M_e is mass flow rate of emitted overflow [2].

Reduced Total Efficiency

The reduced total efficiency give the actual separation effect of the cyclone. The flow split to underflow and overflow is taken into account by subtracting the volumetric underflow to feed ratio, R_f, Equation (2.15), from the total efficiency, η_T, Equation (2.14) [4].

$$\eta_T{}' = \frac{\eta_T - R_f}{1 - R_f} \tag{2.14}$$

$$R_f = \frac{Q_{underflow}}{Q_{feed}}, \tag{2.15}$$

where $Q_{underflow}$ is the volumetric underflow rate and Q_{feed} is the volumetric feed rate.

2.6.2 Separation Efficiency Models

Normally two concepts of modelling the cyclone separation efficiency are considered:

- The *equilibrium orbit* model
- The *time-of-flight* model

The equilibrium orbit model considers the forces acting on a particle rotating at CS, or locus of zero vertical velocity, Figure 2.11 a). The centrifugal force, which is directed outwards, is balanced against the inward directed drag force caused by the flow through, and perpendicular to CS. The centrifugal force is proportional to the mass of the particle and the drag force is proportional to the diameter of the particle. Small particles are therefore dragged into the inner vortex and large particles are separated to the outer vortex. The particle size at which these two forces balance, the particles have a 50-50% chance of exit through the underflow or the through the overflow, Figure 2.11 b). This particle size is called the cutsize, x_{50}, of the cyclone and is important for the separation capability of the cyclone.

The time-of-flight model considers the time the particle use to get from the inlet to the wall of the cyclone. In the original time-of-flight models it was investigated if the injected particle had time to reach the wall and be collected before reaching the bottom of the cyclone. Newer time-of-flight models use ideas form the equilibrium orbit model in addition to the old time-of-flight models. The concept in the newer models is that both the particle movement towards the cyclone wall and the particle exchange across the CS, due to centrifugal force and turbulence respectively, are considered.

Both the equilibrium orbit model and the time-of-flight model give good measurement of the separation efficiency. The results from the two models agree well and give reasonable resemblance to each other even though being different in nature [2].

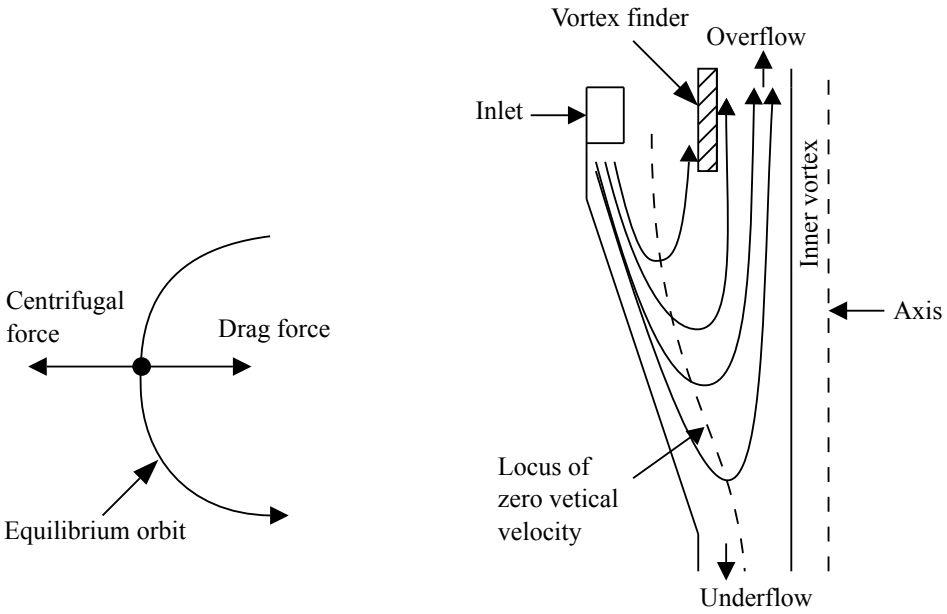

Figure 2.11: Illustration of the equilibrium orbit model adapted from [14]. In a) the forces acting on a particle in a cyclone and in b) the locus of zero vertical velocity is illustrated. Cutsize particles lie on the locus of zero vertical velocity line and have 50-50% chance of exit through the underflow or overflow

2.6.3 Grade-Efficiency Curve

The overall separation efficiency does not consider the particle size in the feed and is therefore not a good method to measure the separation efficiency for a cyclone. For better measurement a grade-efficiency curve (GEC) is used. The grade-efficiency curve is a specific function for a given feed particle size in a given cyclone [2], Figure 2.12.

To obtain a GEC a series of batches with mono sized particles, or one batch containing particles in the required size range is fed into a cyclone, the latter method being the easiest and most used. In both methods the total efficiency has to be measured. For the latter method the particle size distribution for two of the material streams (feed, underflow, and overflow) has to be analysed [4].

The cutsize of a cyclone can be found in a grade-efficiency curve where the efficiency $\eta(x)$ is 50%, Figure 2.12. The grade-efficiency curves for several different viscosities have been plotted in Figure 2.13. The curves show that the cutsize increases with increasing viscosity [14], [15].

Reduced Grade-Efficiency Curve

The efficiency in a cyclone is influenced by the effect of the flow splitting. Figure 2.12 shows a typical grade-efficiency curve. The curve does not start from the origin instead it has an intercept. The intercept is almost equal to the volumetric underflow to feed ratio, R_f. For large particles the curves are nearly the same, which is connected to the effectiveness of separation of large particles and that these particles are not affected by

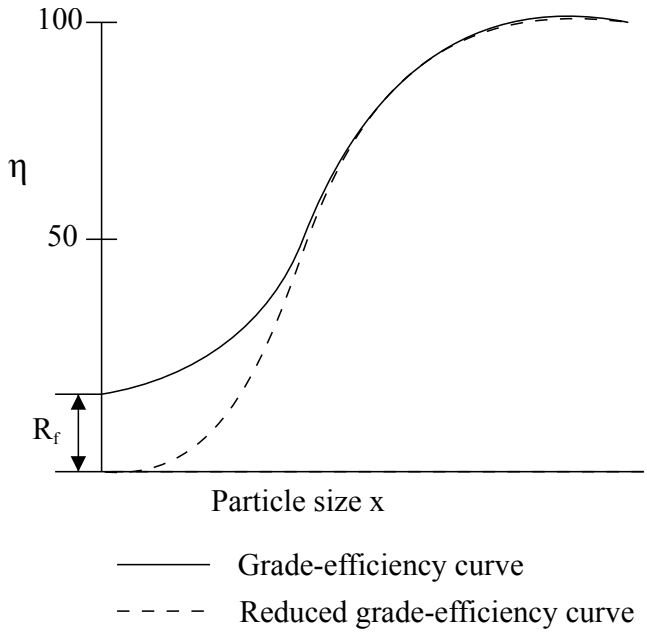

Figure 2.12: Sketch of a grade-efficiency curve and a reduced grade-efficiency curve adapted from [4]. The curves are typically s-shaped

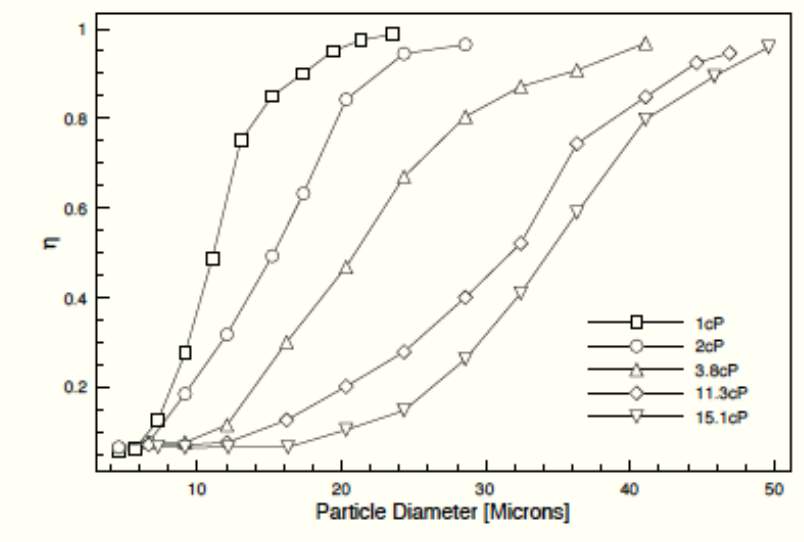

Figure 2.13: Experimental grade-efficiency curves for several viscosities taken from [15] p. 67. The cutsize increases with increasing viscosity.

the underflow ratio. The smallest particles will not be separated by the cyclone and the recovery factor for these particles will therefore be equal to the underflow ratio [4].

2.6.4 Cutsize

The cutsize is the particle size that corresponds to 50% collection efficiency. According to the original equilibrium-orbit model, two parameters need to be estimated to calculate the cut-size for a specific cyclone geometry; the length of the cyclone core and the tangential velocity of the flow at the edge of the cyclone core. This means that the geometrical dimensions of the cyclone have to be taken into account when calculating the cutsize [16]. A particle at the cutsize has 50-50% chance of exiting through the overflow or the underflow, this is illustrated in Figure 2.14.

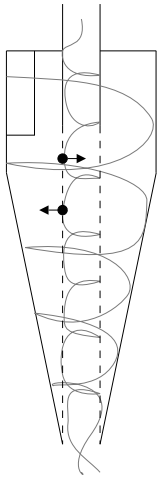

Figure 2.14: Illustration of a particle with the cyclone cutsize. The particle has a 50% chance of exit through the overflow

2.7 Cyclone Scale-up

Grade-efficiency curves have the same shape for a given family of geometrically similar cyclones, hence scale up for cyclones is based on the cutsize [4]. A cyclones separation efficiency can also be found by dimension analysis of the parameters effecting the separation efficiency. Equation (2.16) is a simplified expression of the separation efficiency;

$$\eta(x) = f(x, \Delta\rho, \rho, \mu, v_{ch}, D). \tag{2.16}$$

Where $\eta(x)$ is the separation efficiency, x is the particle diameter, and $\Delta\rho$ is the density differences between the fluid and the particle. The fluid density is described with ρ, μ is the fluid viscosity, v_{ch} is a characteristic velocity (e.g. inlet velocity), and D is the diameter of the cyclone body. Classical techniques for dimension analysis are used to obtain the separation effect in Equation (2.17),

$$\eta(x) = f(Re, Stk, \frac{\Delta\rho}{\rho}), \tag{2.17}$$

where Reynolds number, Re, is calculated from Equation (2.18) and Stokes number, Stk, from Equation (2.19) [2].

The Reynolds number, Equation (2.18), depends on viscosity, μ, density, ρ, velocity of the flow, v, and on the diameter of the cyclone body, D [17],

$$Re = \frac{\rho v D}{\mu}. \tag{2.18}$$

The Stokes number, Equation (2.19), depends on differences in density between particle and fluid, $\Delta\rho = \rho_p - \rho$, the particle size, x, velocity, v, viscosity, μ, and on the diameter of the cyclone body , D [2],

$$Stk = \frac{\Delta\rho x^2 v}{18\mu D}. \tag{2.19}$$

The density ratio, $\Delta\rho$, in Equation (2.16), is already taken into account in the Stokes number, Equation (2.19). The separation efficiency can therefore be expressed as a function of the Stokes number and the Reynolds number,

$$\eta(x) = f(Re, Stk). \tag{2.20}$$

The cutsize is often needed when applying scaling rules for cyclones. Then $\eta(x)$ in Equation (2.20) is set to 0.5 and the Stokes number is denoted correspondingly giving Equation (2.21) [2],

$$Stk_{50} = f(Re). \tag{2.21}$$

The Stokes number is needed for calculations of the cutsize. The Stokes number at 50% efficiency, Stk_{50}, is constant over a wide range of Reynolds numbers and can therefore be used for cutsize calculations for geometrically similar cyclones. When Stk_{50} is known for a cyclone a specific cutsize for an other cyclone can be calculated. The relationship between the square root of Stk_{50} against Re is demonstrated in Figure 2.15.

From Figure 2.15 it can be seen that for cyclones with Re over 2×10^4, Stk_{50} is reasonable independent [18]. The weak dependency of Stk_{50} on Re leads to the widely used *Stokesian scaling* of cyclones. In Stokesian scaling geometrical similar cyclones are assumed to have the same separation efficiency for the same value of Stk [2].

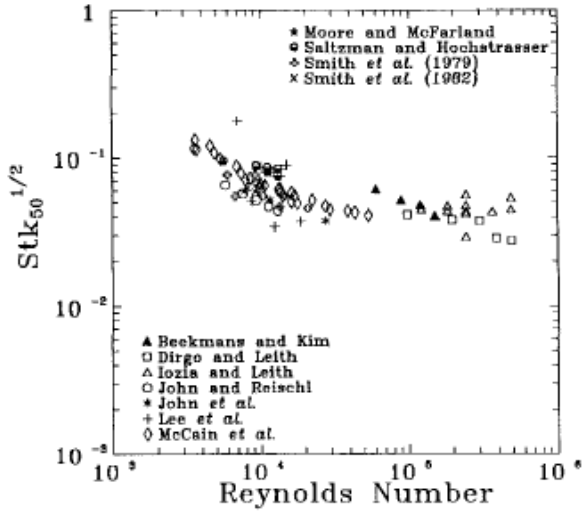

Figure 2.15: Stk_{50} versus Re for a range of different cyclones taken from [18] p. 369. The inlet velocity v_{in} have been used to define Stk_{50} and Re. The weak dependency of Stk_{50} on Re leads to the widely used Stokesian scaling of cyclones

2.8 Pressure Drop

It is not easy to measure the pressure drop, Δp, in cyclones. Pressure drop in process industry is normally measured by measuring the upstream and downstream static pressure in the piping. In cyclones the swirling motion of the fluid cause problems for the measurement of the pressure drop. The static pressure at the wall is higher than the cross-sectional average due to swirling flow and there is dynamic pressure stored in the swirling motion. The term *pressure drop* in cyclones is therefore the sum of static and dynamic pressure, Figure 2.16.

There are three main contributions to the pressure drop; losses in inlet, cyclone body, and vortex finder. The loss in the inlet is negligible compared to the two other losses, especially with tangential inlet. The cyclone body mainly limits the intensity of the swirl in the vortex, which mean less intensive vortex due to more frictional loss at the wall. The pressure drop in the vortex finder may be an order of magnitude larger than the other two contributions and are the largest of the three pressure drops. As in all other process equipment with turbulent flow the pressure drop is proportional to the square of the volumetric flow rate [2].

Static pressure in the cyclone is transformed into dynamic pressure by the vortex. The fluid is accelerated as it moves from the outer to inner vortex in the cyclone. The acceleration is due to the principle of conversion of moment-of-momentum (or angular momentum). The vortex is intensified by less frictional loss which gives a more effective conversion from inner to outer vortex, and it lowers the central static pressure the fluid enters the vortex finder with. Cyclones with aerodynamically smooth walls and geometries produce the highest spin in the vortex and the largest decrease in static pressure within the core, which leads to the best separation performance.

With increasing solid load, wall roughness and cyclone body length the pressure drop

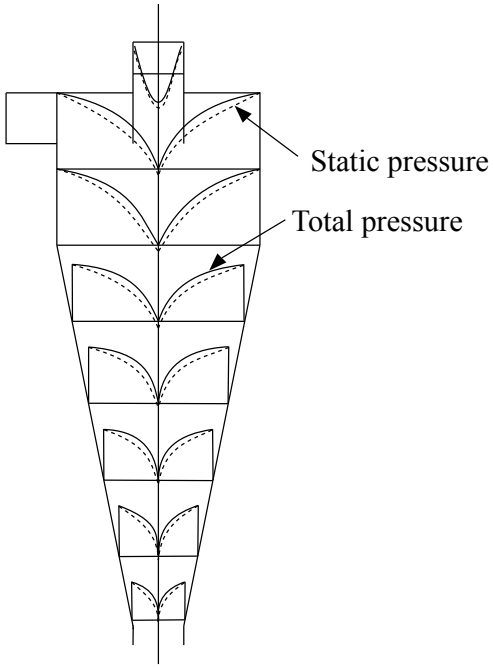

Figure 2.16: Sketch of static and dynamic pressure profiles in a cyclone adapted from [2]. The term pressure drop in cyclones is the total pressure drop, sum of static and dynamic pressure drop. This is because dynamic pressure drop is stored in the swirling motion, and the static pressure at the wall is higher than the cross sectional average due to the swirling motion

in the cyclones will decrease. In a cyclone with heavy solid load the fluid will be robbed for much of its energy from drag between the particles and the fluid. This is clear as the core spin velocity and static pressure loss is reduced. A cyclone with very rough wall conditions will have increased energy dissipation along the walls but less overall pressure loss. If there are not installed any pressure recovery devices the true dissipative loss over the cyclone is the static pressure measured at the wall of the outlet tube minus the static pressure at the inlet [2].

Chapter 3

Positron Emission Particle Tracking

In this chapter the principles of the PET scanner and the PEPT technique are presented. Information about radiation and how the particles are labelled are discussed. How the PET scanner detects the particles and how the data are post processed in the PEPT algorithm is also presented.

3.1 Radiation

Natural radioactivity in potassium uranyl sulfate was first discovered in 1896 by Antoine-Henri Becquerel. Tremendous contributions to the discovery of many other natural radioactivity elements were made by Pierre and Marie Curie, Ernest Rutherford and Frederick Soddy. In 1934 did Irène Joliot-Curie and Jean Frédéric Joliot report the first artificial radioactivity. They had managed to irradiate boron and aluminium targets with alpha- (α) particles from polonium. Even after removal of the α-particle source they observed emitted positrons from the target. The cyclotron, neutron and deuteron were discovered by various scientists around the same time, which facilitated production of more artificially produced radioactive sources. In nuclear medicine artificially produced radionuclides are the most common and are primarily produced in a cyclotron or a reactor [19].

In this thesis the planetary model will be used to describe the atom. The part of the atom consisting of protons and neurons is called the nucleus. Radiation is distributed across the electromagnetic spectrum and can be divided into two types; electromagnetic and radioactive decay (also called particulate radiation).

Ionisation is caused by radiation with enough energy to remove electrons from atoms, this radiation is called ionising radiation. Only high-energy electromagnetic radiation such as x- and γ -radiation, and charged particles (α, β^-, β^+), have enough energy to cause ionisation. Light and microwaves are examples of non-ionising electromagnetic radiation. Ionising radiation of radioactive decay is of interest considering PET [20].

Electromagnetic Radiation

The human senses can detect some electromagnetic radiation, e.g. visible light ($\lambda \approx 10^{-7}$ m) and heat, i.e. thermal radiation, with wavelength $\lambda \approx 10^{-5}$ m. The electromagnetic radiation is pure energy and the amount of energy is defined by the length of waves escaped from the radioactive source, called wavelengths (λ).

The properties of electromagnetic radiation can be handled as waves and as particles, this view of properties are known as the wave-particle duality. Electrons can pass from one electron position to another by passing a *forbidden zone* where electrons cannot exist, which is not possible when electrons are viewed as particles. This behaviour, however, is possible when the electromagnetic radiation are viewed as a wave with zero amplitude in the forbidden zone [20].

3.1.1 Radioactive Decay

Antoine-Henri Becquerel showed that natural uranium produced radiation spontaneously a year later than Wilhelm Röntgen produced the x-rays. At the time it was believed that the particle emission of natural radioactive decay was the same type as the x-rays, but Rutherford proved that some radiation were more penetrating than others. He called them alpha- (α) rays and beta- (β) rays, where β-rays were more penetrating than α-rays. Later it was shown that this type of radiation carried charge, which means they could be deflected by a magnetic field. This proved that the radiations where not electromagnetic waves but particles.

Among the first observations of radioactivity was particle emission of natural radioactive decay, today this type of radiation is also called particulate radiation. As mentioned nuclei spontaneously undergo radioactive decay. The nucleus is characterised by the rate it undergoes radioactive decay, called the half-life parameter [20] .

Half-life

Half-life is the time it takes for the nucleus activity to be reduced to half of its original state. This is an exponential function where the

> "numbers of atoms decaying at any particular instant in time is determined by the number of unstable nuclei present and the decay constant (k) of the nuclide" [20] p 19.

Equation (3.1) is the half-life equation [20],

$$t_{\frac{1}{2}} = \frac{1}{k} ln2, \tag{3.1}$$

where $t_{\frac{1}{2}}$ is the half-life and k is the decay constant.

Activity

Activity of the radionuclide is the rate of decay of unstable nuclei at any point in time. The activity of a nuclide is the number of atoms decaying each second. The activity of a particle after a given time t is given by Equation (3.2),

$$A_t = A_0 e^{-kt}. \tag{3.2}$$

Where A_t is the amount of activity present after a time interval t, A_0 is the amount of activity present initially, and k is the decay constant [20].

Alpha Decay

Alpha decay, α-decay, is helium nuclei, ${}^{4}_{2}\mathrm{He}^{2+}$, and is emitted from atoms with large number of protons in the nucleus. Many naturally occurring radioactive decay series are formed by α-particles. It is easy to shield and stop the α-particles due to their large mass. They deposit a large amount of energy in a very small distance in matter which can cause big medical problems if ingested [20].

Beta Decay

Beta decay, β^{-}-decay, is negatively charged electrons emitted from the nucleus as part of the radioactive disintegration. The energy range of the beta particles increases up to a maximum. This was first thought to be a violation on the law of conservation of energy but in 1931 the neutrino particle (ν) was introduced . The neutrino particle is a particle with very small mass and no charge, which

> "could carry away the excess momentum to account for the difference between the maximum beta energy and the spectrum of energies that the emitted beta particles displayed" [20] p. 21.

The neutrino emitted in β^{-}-decay is referred to as the *antineutrino*, indicated by $\bar{\nu}$. β^{-}-decay is not conserved and is therefore considered a weak interaction [20].

Positron Decay

Positron decay can be produced from either a nuclear transmutation or by pair production, in this thesis the pair production is in focus. In positron decay a proton is converted into a neutron, a positron and a neutrino. The process can also be referred to as a positive beta decay, β^{+} decay [21]. This means that both a positron and an electron are emitted and the nucleus after the decay are two electron masses lighter than before. Equation (3.3) is the general positron decay equation [20],

$$ {}^{A}_{Z}\mathrm{X} \rightarrow {}^{A}_{Z-1}\mathrm{Y} + {}^{0}_{1}\beta^{+} + \nu + Q(+e^{-}). \tag{3.3} $$

Where Q is energy and X is a proton-rich atom which convert a proton into a neutron to achieve stability, and the positive charge is carried away with the positron β^{+}.

Positron-Electron Annihilation

Positron-electron annihilation happens outside the nucleus. For each positron decay an annihilation of two photons are produced, Figure 3.1.

When a positron is ejected from the nucleus it travels a finite distance through matter where it looses its energy by interaction with other nuclei and electrons along the way. The positron continues to move until it comes to a rest and combines, annihilates, with an electron. When the positron and electron annihilates two photons, γ-rays, with the energy equivalent to the rest-mass energy of the particles 511 keV each, Equation (3.4), is emitted back-to-back (180 °) from each other.

It is these approximately anti-collinear photons that are used to localize and defining the lines of response (LOR) in the PET scanner [20].

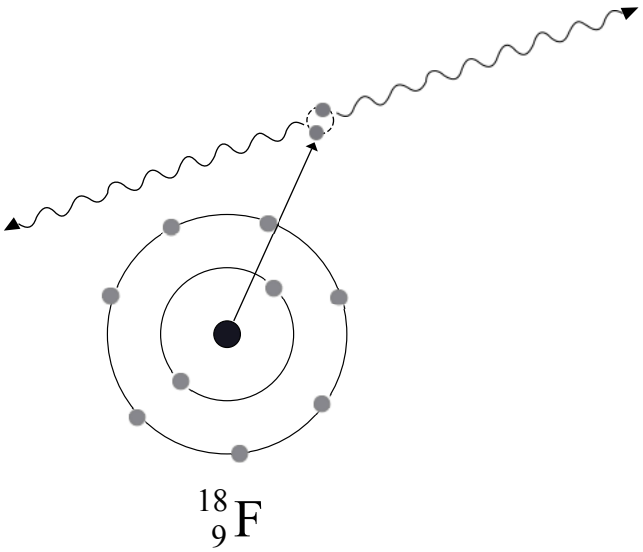

Figure 3.1: Illustration of annihilation radiation adapted from [20]. In annihilation two photons, γ-rays, with each the energy equivalent to the rest-mass energy of the particles are emitted back-to-back (180 °) from each other. It is these approximately anti-collinear photons that are used to localize events in PET

$$E = mc^2, \tag{3.4}$$

Where c is the speed of light[1] and m is rest-mass. For a positron or electron the rest-mass is equal to 9.11×10^{-31} kg. The rest-mass energy is then calculated,

$$E = 9.11 \times 10^{-31}\text{kg} \times (3 \times 10^{8}\text{ms}^{-1})^2 = 8.2 \times 10^{-14}\text{J}.$$

Electron volt (eV), is defined as the energy required to move a unit charge through an electric field with a potential difference of one Volt. 1 eV is equal to $1.6 \times 10^{-}19$ Joule,

$$E = \frac{8.2 \times 10^{-14}}{1.6 \times 10^{-19}} = 511 \times 10^{3}\text{eV} = 511\text{keV}.$$

3.1.2 Interaction With Matter

Energy from high-energy radiation can be transferred to the material when it interacts with matter. Particles with larger mass have a higher chance of being absorbed by the surrounding material than smaller particles. This is why the β-particle is more penetrating than the α-particle, which has a short penetrating range in matter. The neutrino is very hard to stop or detect, which is due to a very small mass and no charge. The massless high-energy photons are highly penetrating.

There are three mechanisms for how photons interact with matter, depending on the energy of the radiation. The mechanisms are: pair production, Compton scattering, and the photoelectric effect. The last interaction mechanism, photoelectric effect, does not

[1] c= 3×10^{8} m s^{-1}

have a large impact on the PET scanner and is therefore negligible. In human tissue the photoelectric effect dominates at energies lower than 100 keV, which is why the photoelectric effect has to be taken into account in PET/CT scanners when the CT, *Computed tomography*, is used for correction of the PET results for patients [20].

Pair Production

Pair production happens when high energy photons (1022 keV) come close to a nucleus. The photons may then convert into two electrons; one positive, also called positron, and one negative to conserve charge, Figure 3.2. The conversion happens spontaneously. The pair production is the dominated mechanism for photons with high energies and the probability for pair production increase over 1022 keV as the amount of energy increases [20]. Pair production demonstrate both the law of conservation of energy and the law of conservation of momentum.

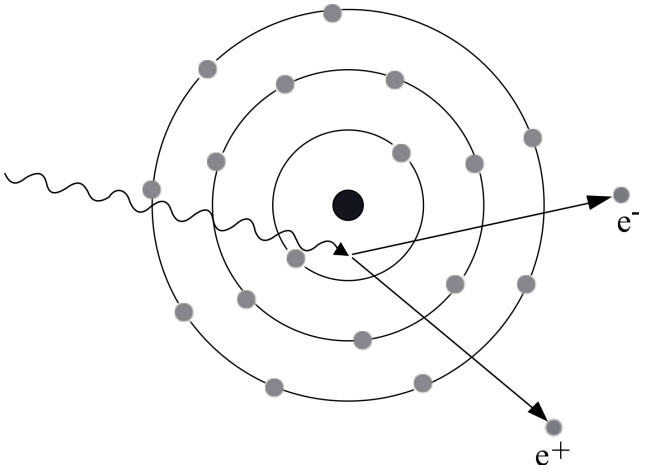

Figure 3.2: Illustration of pair production adapted from [20]. When high energy photons come close to a nucleus they can spontaneously convert into two electrons with opposite signs, one electron and one positron, this interaction mechanism is called pair production

Compton Scattering

Interaction between a loosely bound orbital electron, recoil electron, and a photon is called Compton scattering. The direction of the photons is changed after the interaction and the recoil electron is ejected from the atom, Figure 3.3. In the interaction the photon loose part of its energy and this energy is transferred to the ejected recoil electron. The energy loss is independent of the electron density and the properties of the material. The angle the recoiled electron is deflected by is proportional to the amount of energy loss in the interaction [20]. Since the photon change direction, i.e. is scattered, and loose energy the signal detected in the PET scanner will be wrong.

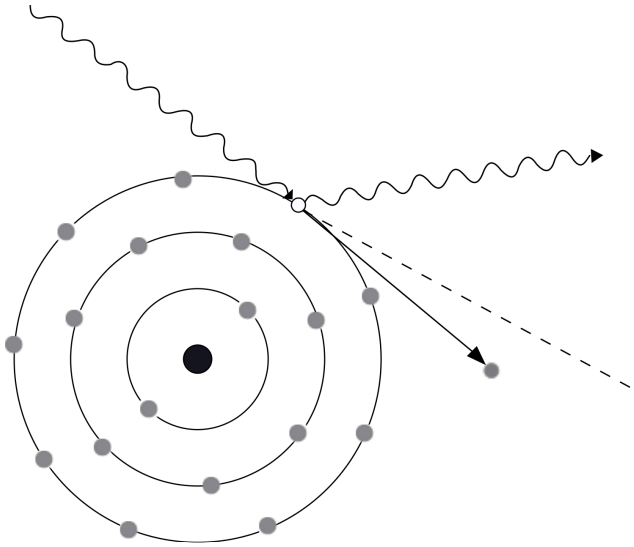

Figure 3.3: Illustration of Compton scattering adapted from [20]. Part of the energy of the incoming photon is transferred to an electron, the recoil electron, in Compton scattering. The angle the photon is deflected through is proportional to the amount of energy lost

3.2 Positron Emission Tomography

Positron emission tomography (PET) has been developed as a functional imaging technique in medicine over the last decades. PET is an imagining technique where detailed images of the metabolism is detected. The PET technique for medical use is based on techniques for reconstruction of images and spatially distributed radioactive sources. The distribution and concentration of the radioactive substances are time dependent, and hence images can be obtained [21].

When PET is used for clinical purposes the scanner detects the concentration of radioactively labelled species as a function of time after introduction. The detected signals makes it possible to obtain detailed images of the metabolism [22]. PET is mainly used to detect cancer cells and other diseases. The detailed images revolutionised the nuclear medicine and are in some cases used to change decisions on surgical treatment, both enabling potential lifesaving operations and avoiding unnecessary operations. PET is mostly used for diagnosing and treatment for lymphoma and other cancer types [20].

3.2.1 Cyclotron

A cyclotron produce artificial radionuclides by accelerating charged particles, such as protons, deuterons, α-particles and so forth, in circular paths in so-called dees A and B, Figure 3.4. The particles are accelerated under vacuum by means of an electromagnetic field. The energy of the particles increases as the radius of the particle trajectory increases since the charged particles move along circular paths in a magnetic field with increasing energy. This relationship between radius and energy is definitely established in a given cyclotron. The accelerated particles irradiate the target nuclei and a nuclear reaction takes place when stable target elements are placed in the external beam of the

accelerated particles, or in the internal beam at a given radius in the cyclotron. Energy is either absorbed or released in the reaction and each nuclear reaction for the production of a nuclide has a definite threshold of energy [19].

Radionuclides which decay by positron emission, hence annihilation radiation of 511 keV γ-rays, Section 3.1.1, are important for PET imaging. These radionuclides such as ^{11}C, ^{13}N, ^{15}O and^{18}F are short-lived radionuclides, which means that they have a very short half-life. Because of the short half-life of the radionuclides a cyclotron or a medical cyclotron must be placed on site of the PET laboratory. The primary use of a medical cyclotron is to produce radionuclides for medical applications and provide low-energy charged particles of high intensity. The medical cyclotron is a small version of a cyclotron [19].

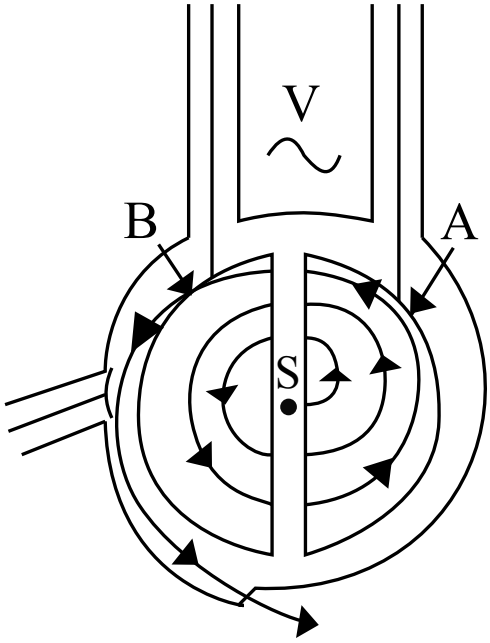

Figure 3.4: Sketch of a cyclotron adapted from [19]. The cyclotron produce artificial radioactivity by accelerating charged particles in circular paths in so-called dees A and B under vacuum by means of an electromagnetic field

Fluorine-18 have a half-life of 110 min and is produced by the ^{18}O(p,n)^{18}F reaction on a pressurised ^{18}O-water target. By passing the mixture through a column of quaternary ammonium resins, ^{18}F can be recovered as $^{-}$F ions and ^{18}O-water can be reused as target [19]. It is the short-lived radionuclei ^{18}F that is used for particle labelling in this thesis.

3.2.2 Detectors in PET

To detect the radioactive signals in a PET scanner scintillation detectors are used. The scintillation detector is made of an inorganic crystal that will emit visible light photons after interaction with photons within the detector. To measure the amount of photons a photo-detector is used [20].

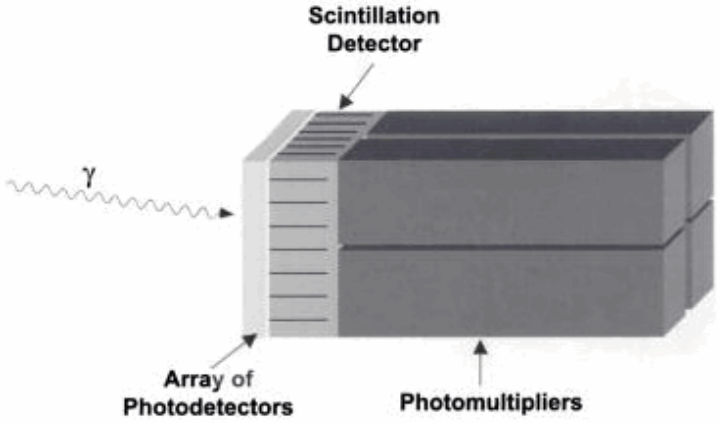

Figure 3.5: Illustration of a scintillation detector taken from [20] p. 38

3.3 The Positron Emission Particle Tracking Technique

Over the years chemical engineers have researched the use of PET to study flow fields by use of a positron emission tracer. There have been several studies and good results from use of this technique. Today there are a few PET scanners around the world used for research by engineers and physicist. The technique is called positron emission particle tracking (PEPT). When the PET scanner is used for the PEPT technique a tracer particle is introduced into the equipment that is investigated. Information about how particles or solids move through the flow field of different equipment is important in further development of optimal equipment design and operating conditions for a wide range of industrial process designs [23].

3.3.1 Principles of the PEPT Technique

The tracer particle is labelled with a radioactive isotope before being introduced into the equipment. Hoffmann et al. [24] showed that it is possible to follow a tracer particle through a high-speed flow field by use of the PEPT technique.

When the tracer particle is sent through the *field of view* (FOV) in the PET scanner it emits back-to-back radioactive signals. Detectors in the PET camera detect the back-to-back signals as lines of response (LOR). There is only one tracer particle in the field of view, hence all the detected LOR's should meet at the point of the tracer particle's position within the resolution of the PET camera, Figure 3.6. It is therefore possible to trace the movement of a particle through a flow field [22].

When two annihilation signals are detected within a narrow time window, called the coincidence window, it is decided that the signals are emitted from the same annihilation and a LOR can be drawn between the two detectors, Figure 3.7.

"The position of the LOR is stored as

- its radial distance to the camera axis (z-axis),

- its azimuthal angle with the vertical (y-axis), and
- the axial distance of each of the two detectors from the back of the detection volume (z-axis)" [24] p. 2.

The coincidence time window has to be narrow enough to reject γ-rays emitted from two annihilations close in time but broad enough to include all true photons [21]. Some of the detected events are in practice corrupt. It means that one or both photons might be scattered before detection, or the detected events do not come from two photons annihilated in a single positron decay [22].

Signals detected in the same narrow time window is not guaranteed to form a good LOR, it can also be a corrupt event called *random coincidence*. Random coincidences can appear when two different events give rise to single detection within the same time window. The other two photons, not detected, is either falling outside the detection zone or penetrating the detector without being detected. The detector will draw a LOR between such events but the annihilation will not exist on the LOR. To deal with this problem the PET camera uses a *delayed time window* technique to estimate the rate of random coincidence, but it cannot actually tag the LOR's formed by random coincidence. If more than two detections are done in the same time window they are considered to be random coincidence and are rejected.

There is also a possibility that such error LOR's can arise form Compton scattering, and one or both photons can be scattered on the way to the detector causing deflection and decrease in energy. To deal with these events the camera uses an energy window, normally between 350 and 650 keV, and if the events are within the window they cannot be recognised as Compton scattered [24].

Some of the corrupt events is discarded by the PEPT algorithm and the scattered events are smoothed out in the post processing of the results.

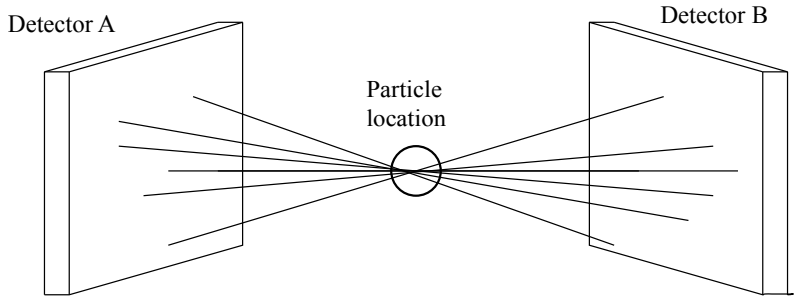

Figure 3.6: The PEPT location method. In PEPT there is only one tracer particle in the field of view, and hence all detected LOR's has to come from this particle. The meeting point of all the detected LOR's should therefore be the position of the tracer particle [22]

A challenge to the PEPT research is that the investigated equipment needs to be scaled down to fit into the scanners FOV. Some processing equipment cannot be properly studied when down scaled to fit into the scanner. Parker et al. [22] are investigating the possibilities of building a modular PET camera that can be fitted to the equipment. This would make it easier to investigate how solids move in large process equipment that will not give a real result when down scaled to fit into the medical PET scanner.

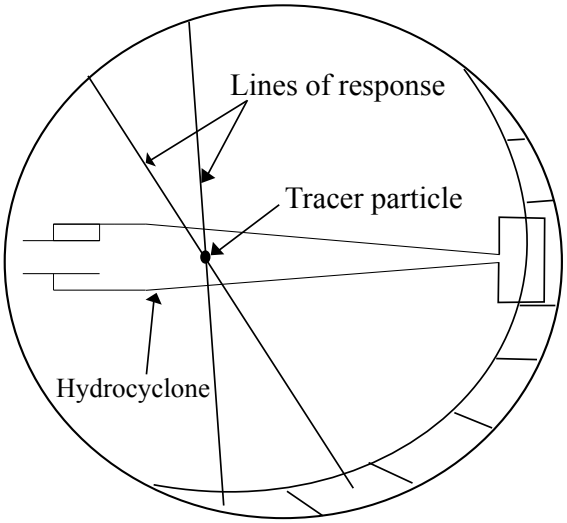

Figure 3.7: The PEPT technique enables the following of a single particle through a flow field, here demonstrated by a hydrocyclone

3.3.2 Particle Labelling

For the detectors to detect the tracer particle in the PET scanner the particle needs to be labelled with a radionuclide that decays β^+-decay with the emission of a positron. Annihilation between the positron and an electron gives rise to two back-to-back γ-rays. Since γ-rays can penetrate a distinguished thickness of material PEPT can, without disturbing the flow, be used for detecting the inside of flow and mixing processes in process equipment [25].

An indirect labelling technique is used, Section 5.2.1. The activity on a particle labelled by this indirect technique does not leak out into the fluid during the experiment [21].

3.3.3 The PEPT Algorithm

An algorithm is developed to find the exact position of the tracer particle in the flow field called the PEPT algorithm. The PEPT algorithm assumes that there is only one single point source in the field of view at all times and can therefore discard all corrupt events and place the accurate location of the tracer particle. The PEPT algorithm triangulates the LOR's and finds the position of the particle at all times.

The first estimate of the tracer location is found by calculating the center of the LOR's from all the events. This is calculated by minimising the sum of distances from the center point to the surrounding LOR's in the FOV. The algorithm discards the LOR's that are furthest from the calculated center point and find a new center point with the remaining LOR's. The algorithm continues this iterative process until a predefined fraction of the initial events are used. The point of minimum distance from the final sets of events is given as the location of the tracer particle [22]. The velocity of the tracer particle is found from successive locations the particle pass throughout the field of view of the PET camera [23].

Chapter 4

Literature Study

Hydrocyclones/cyclones have been used in the industry for about a hundred years, and have over the years been further developed and investigated. The internal flow pattern of the cyclone was for a long time unknown. Many different techniques has been used for investigation of the internal flow pattern and in the later years the particle path in the cyclone has been researched. The PEPT technique is a rather new investigation technique for this kind of work but have been used to track particles in different processing equipment. *Computational fluid dynamics* (CFD) has also been used in later years to investigate the flow and particle trajectories in cyclones and other processing equipment. In this chapter earlier investigations in the fields of interest for this thesis are presented.

4.1 Experimental Investigation of Flow in Cyclones

Hoekstra et al. [16] investigated the flow in a gas cyclone by Laser-Doppler velocimetry (LDV). Seeds were injected into the gas stream and the LDV detected the velocity of the seeds in four different axial measurement stations. Experiments were performed with three different vortex finder diameters. CFD was also performed on the subject of turbulence in the flow field of the cyclone. The results of the experiments show that for all three vortex finder diameters the Burgers vortex can be seen in the swirl distribution. There were, however, differences in maximum tangential velocity and in the size of the core region for the profiles. When the vortex finder diameter was reduced the maximum tangential velocity increased. The diameter of the vortex finder also affect the free-vortex profile in the outer region of the cyclone. The axial velocity profiles also depends on the diameter of the vortex finder. In the LDV measurements pseudo-turbulent fluctuations were introduced, this was caused by the so-called precessing vortex core that dominates the core region. Form the CFD results Hoekstra et al. concluded that either the $\kappa - \epsilon$ model nor the RNG-$\kappa - \epsilon$ were suitable for modelling the turbulent flow in the vortex. The Reynolds stress transport model gave reasonable results for the axial and tangential velocity profiles compared to the experimental results.

Peng et al. [9] studied the reversed experimental flow patterns in a conventional cylinder-on-cone cyclone and in a swirl tube by use of Laser-Doppler anemometry (LDA). Several differences between the swirling tube and the cylinder-on-cone cyclone were discovered. E.g. the locus of zero axial velocity was higher in the cylinder-on-cone cyclone than in the swirl tube, which indicates that the separation should be slightly better in the cylinder-on-cone cyclone than in the swirl tube. Peng et al. conclude that in the

cylinder-on-cone cyclone the tangential velocity was axially constant in parts of the cyclone with small radius. The tangential velocity in swirl tubes decreases slightly as it moves axially downwards. Results from the LDA and CFD agree that the radial velocity was uniform in the separation zone in the cylinder-on-cone cyclone, except for a small but strong lip-leakage under the vortex finder. In the swirl tube radial velocity was present all through the separation zone with strong presence under the vortex finder and at the bottom of the tube. It was also found both by LDA and CFD that the locus of zero axial velocity was determined more by the geometry of the separation body than by the vortex finder.

Wang et al. [26] used a high-speed motion analyser (HSMA) to track injected particles in a hydrocyclone. Particles with different sizes were injected at three different points in the inlet of the hydrocyclone. The high-speed camera obtained a film of the particles injected and the film was transformed into frames. From the frames the particle trajectories could be obtained by plotting the position of particles at different times. The results showed that the larger the particle the more centrifugal force was acting on the particle, hence more particles were separated to the underflow. More of the smaller particles were separated out to the overflow without entering the conical section. It was also observed that some of the particles had longer residence time than others. The reason was that the particle moved in circles up and down in the cyclone before entering the underflow. One explanation for this behaviour can be that the particle fell into the locus of zero vertical velocity. When particles with the same size were injected at different points in the inlet, Wang et al. observed some differences in the trajectories and concluded that the particle trajectory in a hydrocyclone was featured with stochastic characteristic, but the overall samples of trajectories hold the statistical property. The separation performance and the particle trajectory in the hydrocyclone were heavily affected by the initial position of the particle injection point.

Marins et al. [27] investigated the three components of the mean velocity in a hydrocyclone. The velocity components were characterised by Laser-Doppler anemometry (LDA) (two components) and Particle Image Velocimetry (PIV) (three components) in a hydrocyclone with a cone angle of 15°. The PIV technique cross-correlate frames of a number of particles and determines the mean velocity from the result. The LDA technique determines the mean velocity by detecting light scattered by two angles. Some turbulence could also be seen with these two techniques but even with some optical noise problems, the results can be used for model validation. Marins et al. concluded that the experimental data was a good fit to theory, and can be used for validation of numerical simulation for flow in a hydrocyclone.

Experimental investigations of the flow in cyclones have been performed by several other research groups e.g. Kang and Hayatdavoudi, [6], Coelho and Medronho [28], Kawatra et al. [14], Hoffmann et al. [29], Severino et al. [30], and Hararah et al. [31].

4.2 Investigation of a Flow Field by PEPT

Hoffmann et al. [24] successfully followed small particles through a small fluidized bed by use of the PEPT technique. This proved that it was possible to follow a high-speed particle through processing equipment by PEPT. A PEPT algorithm was developed that averaged good cut-points and eliminated bad cut-points in a successive elimination

method. The algorithm gave final optimal window size of 10 millimetre and a resolution of 1 millimetre per millisecond. The resolution achieved proves that it is possible to track faster moving particles. It was also shown that a potential for even higher temporal and/or spatial resolution exists.

Parker et al. [22] investigated the possibilities for PEPT use in process technology. One of the challenges is that the medical PET scanner has a rather small diameter. Hence the model must be very small to fit into the field of view in the scanner. Some processing equipment cannot be truly investigated by such small models. The medical PET scanner consists of one or more rings of detectors, this works great for medical purposes, but for PEPT investigations there is another geometrical need. Parker et al. has investigated the possibilities of making a PET scanner where the geometry of the FOV can be altered. This would make a huge difference for further PEPT work in the future. For building the new PET scanner the group had four second-hand PET scanners and components of two more. Parker et al. used one of the scanners for powder blending and one for *small-ring* and *large-ring* PET systems. A transportable modular positron camera was built from components from the other PET cameras. With this new modular positron camera PEPT can be performed on a range of scales from small-scale to full-scale plants. Parker er al. has in [32] used the modular camera on a large fluidised bed at BP's Hull site and used it to study the casting of molten aluminium. The modular positron camera is a major breakthrough in the PEPT technique development. Due to the components age the reliability of the camera suffers. Parker et al. wish to build a modular positron camera from components of newer PET scanners in the future [22].

Chang et al. [21] followed a single particle through a hydrocyclone by use of the PEPT technique. The experiments were done on a Stairmand high-efficiency hydrocyclone with prolonged cone. The pump was located downstream of the tank, the fluid was further lead into the hydrocyclone and out through the overflow and underflow. There was installed a venturi flowmeter at the inlet tube of the hydrocyclone and pressure indicators at the overflow and inlet. The inlet flow and the underflow were controlled by valves. The particle was injected before the pump. There were performed several experiments and Chang et al. concluded that it was possible to detect a detailed particle trajectory with a PET scanner in high-speed flows with sufficient spatial and temporal resolution. It was also found that the particle trajectory was more random than expected i.e. the particle moved in radial direction inwards to the inner vortex, then out to the outer vortex again. There were also indications of the end of the vortex in some of the trajectories.

Other researchers have also investigated different process equipment by the PEPT technique, such as Chan et al. [33], Parker et al. [23], Leadbeater and Parker [34], and Chan et al. [35].

4.3 Numerical Investigation of Flow in Cyclones

Cortès and Gil [8] investigated several models for calculation of the flow in cyclones both by algebraic models and CFD models. The unsteady complex flow in cyclones makes it difficult to make good models for prediction of the flow. Although some of the more complex algebraic models had the most accurate results compared to experimental data, they were not the best suited models to predict the flow when dealing with flow phenomenon as the EoV. To predict the complex flow in cyclones Cortès and Gil concluded

that there was need for unusual high precision and an unsteady simulation model. The *Large Eddy Simulation* (LES) model and the *unsteady Reynolds-averaged Navier-Stokes* (URANS) model were models suited to simulate the whole complexity of the unsteady flow inside the cyclone. Cortès and Gil have also studied two-phase CFD simulations for the flow.

Stegowski and Nowak [5] performed experiments with a radiotracer through a cyclone before simulating the same experiments with CFD. In the radiotracer method a radioactive tracer was injected into the input of the system. The gamma-radiation emitted from the radiotracer was detected by scintillation probes placed at the inlet, overflow and underflow. The detected signals were then analysed. The experiments were also simulated by CFD. The experimental and computational results showed similarities. Stegowski and Nowak also state that the water-solid mixture in a hydrocyclone was sufficiently described by the applied model and CFD simulations. They also state that prediction of the separation of solids for the specified feed and hydrocyclone geometry was possible and that the circulation mixture flow was strongly constrained. The slip velocity effect for the large solids dominate and the turbulence diffusion and particle interactions could be left out.

Derksen [36] used large eddy simulation (LES) for simulations of the turbulent flow in swirl tubes with tangential inlet. The LES model was chosen for the simulations because it can incorporate particle transport much more realistic than other models. The result from the CFD simulations with LES represented the experimentally observed flow well. The simulations were compared to LDA data for quantitative assessment.

Several other aspects of the flow in cyclones have been studied by numerical methods e.g. Hreinz et al. [37], Strutt et al. [38], Pisarev and Hoffmann [39] Raoufi et al. [40], Bhaskar et al. [41], and Pisarev et al.[42].

Chapter 5

Experimental Method and Analysis

A hydrocyclone rig is needed for investigation of the particle trajectory in a hydrocyclone by PEPT. The rig was built by the workshop at the physics department at the University of Bergen, and has been used throughout the whole project. The experiments were executed at the radiology department at Haukeland University Hospital in the spring and autumn of 2011. Many different aspects of the data logged from the PET scanner was investigated, hence several programs for analysing of the particle tracks were developed.

5.1 Apparatus and Instrumentation

The hydrocyclone used for the experiments is incorporated in a recirculation system and is configured to resemble the geometry of a Sairmand high-efficiency cyclone with a modified prolonged cone. The hydrocyclone is operated without an air core since the system is completely filled with water. The hydrocyclone has a tangential inlet and the design has the following measurements, Figure 5.1 and Table 5.1.

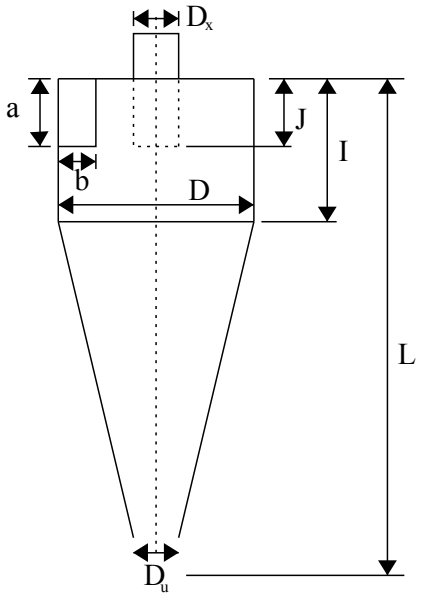

Figure 5.1: Geometry of the hydrocyclone

Table 5.1: Size characteristics for the hydrocyclone

Symbols	L	I	J	D	D_u	D_x	a	b
Hydrocyclone [mm]	414	60	30	40	10	10	29	9

The system is driven by a Cotech XKJ-1305S pump installed downstream of the tank. The tracer particle is injected into the system through a syringe upstream of the pump. There are two ultrasound flowmeters; one measuring the flow of the feed and the other the underflow. A venturi flowmeter is measuring the feed for backup of the ultrasound flow measurements. Three pressure gauges are installed, one on the underflow, overflow, and inlet feed, Figure 5.2.

The underflow of the cyclone should always be made variable, because it is vital to be able to adjust the underflow to get optimal operation opening since this can not be properly predicted [4]. Hence valves are installed for manually control of the inlet flow, underflow and overflow. Both the underflow and overflow are led back to the tank. A valve for emptying the underflow box is installed and the underflow can also be led into the overflow pipe before the tank, Figure 5.2. A thermometer was installed to measure the temperature in the tank.

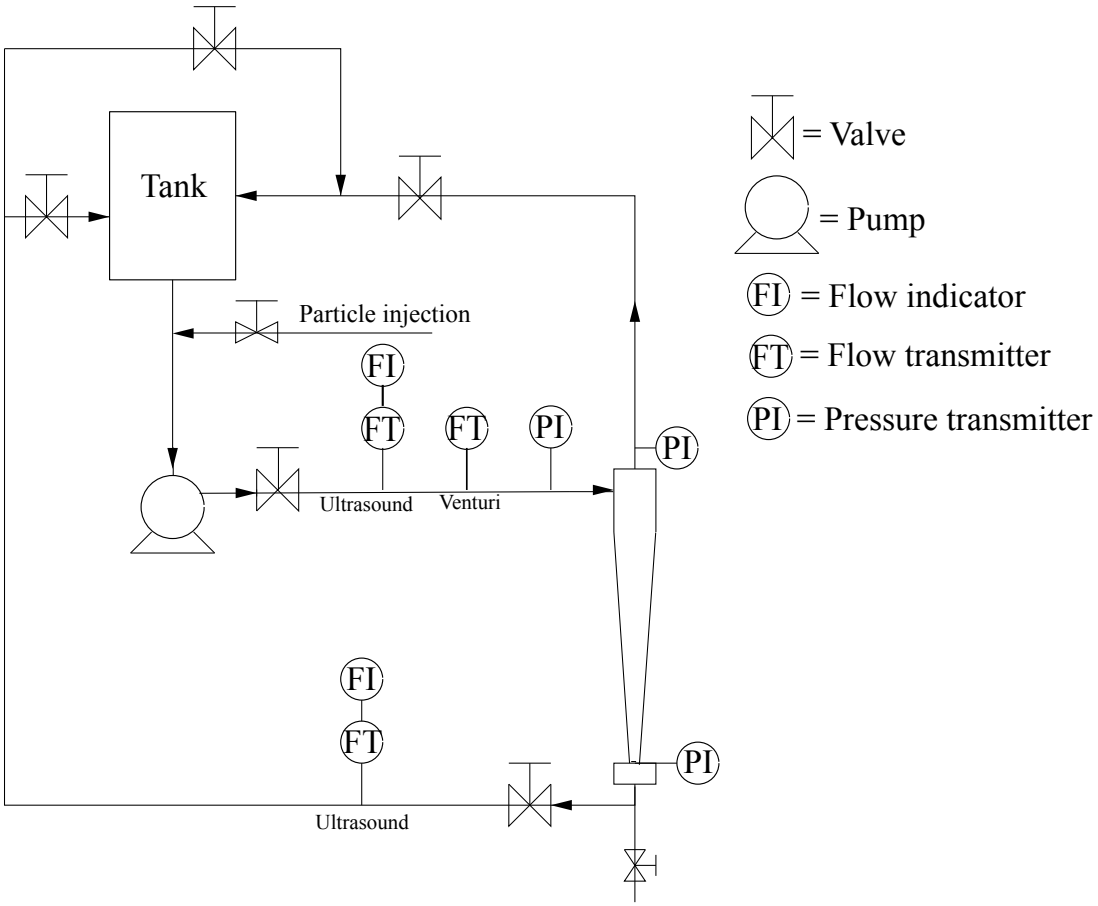

Figure 5.2: Illustration of the experimental set up of the cyclone rig in the circulating system

The hydrocyclone body has a pressure resistant smooth surface. It is manufactured by a *wet lay-up technique*, and is made of a glass-fibre reinforced polymer. Technique and material are suited for a cyclone with small diameter.

A medical PET scanner was used to carry out the experiments. The field of view was small in the scanner and the equipment therefore had to be small as well. This was not a problem for the hydrocyclone since the real size of the apparatus normally is small. The range of the cyclone diameter varies from 10 mm to 2.5 m and the cutsize for most solids vary from 2 to 250 μm in the industry [3]. The particle trajectories obtained in this thesis are therefore reliable as the real size hydrocyclones are of the same magnitude. The hydrocyclone was made as large as possible to fit into the PET scanners FOV, Figure 5.3.

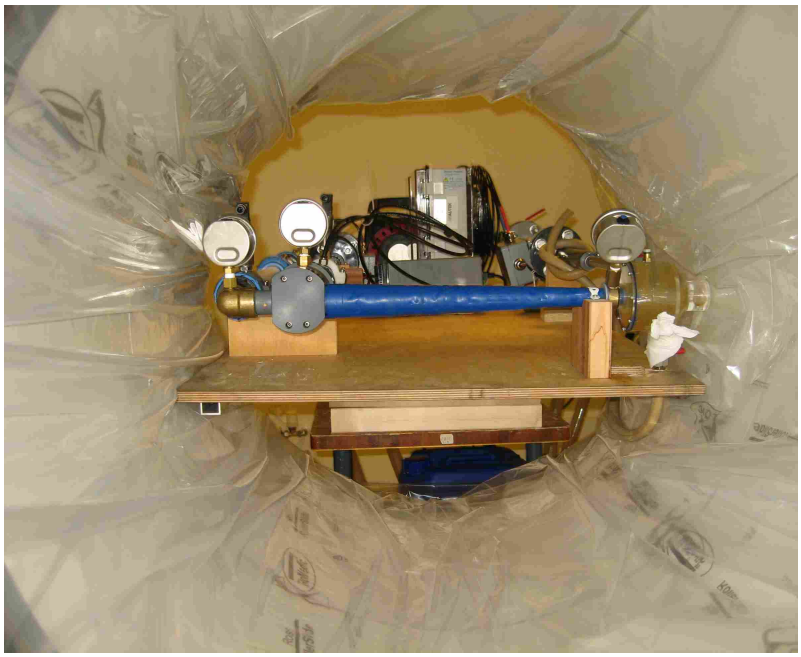

Figure 5.3: Picture of the hydrocyclone inside the PET scanner

5.1.1 Instrumentation

Flow rate and pressure measurement through process equipment are extremely important and a wide number of different flowmeters are available on the market. It was important to measure of the flow rate for the hydrocyclone system since the flow rate was adjusted between each experiment. Two ultrasound flowmeters and one venturi flowmeter were chosen for measurements in the recirculate hydrocyclone system. One ultrasound flowmeter was placed to measure the inlet and the other the underflow, Figure 5.2. The venturi flowmeter was also placed on the inlet pipe to check the reliability of the ultrasound flowmeter. Pressure gauges were installed to measure the inlet, overflow and underflow pressure.

Venturi Flowmeter

A venturi flowmeter is a differential pressure flowmeter. In a differential pressure flowmeter a constriction is placed in the tube, and the pressure is measured before and after the constriction. In a venturi flowmeter the cross-section of the pipe decreases to a minimum before it increases to the original pipe size.

The advantages with a venturi flowmeter is that it is robust, has no moving parts and is easy to maintain. It has disadvantages such as a permanent pressure loss which means it may need extra pumping capacity which leads to higher costs, and it can only be used for clean fluids [43].

Ultrasound Flowmeter

A sketch of the ultrasound flowmeters installed on the hydrocyclone system are seen in Figure 5.4. The flow is lead into a bent pipe and the flow rate is measured by ultrasound signals. The ultrasound flowmeters had some problems showing the right flow rate for the inlet when dealing with high viscosity fluids. The measurements from the venturi flowmeter was therefore used when this problem occurred.

The problem of measuring the high viscosity fluids could be due to air in the system. Observations showed that the ultrasound flowmeter needed some time to stabilize the flow rate even when the fluid was water. These problems could be due to air in the circulating system before start-up. The high viscosity fluids contained a lot of air bubbles which could be the reason the ultrasound flowmeter had problems with measurements of the flow rate.

The underflow ultrasound flowmeter was assumed to show correct flow rate. The underflow flowmeter showed a decreasing flow rate as the inlet valve was opened. When the inlet valve was fully open the underflow flowmeter showed zero flow rate, which was also visually verified through the transparent hoses on the underflow.

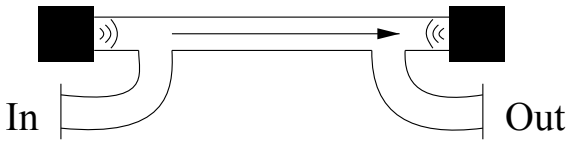

Figure 5.4: Illustration of the ultrasound flowmeter adapted from [44]

5.2 The Tracer Particle

The particles used in the experiments were strong anion exchange beads, Amberlyst A21 Hydroxide Form. The particle size was measured in the group to be 430 ± 56 μm. The particles provide more binding sites due to their macro reticular and porous structure. This is beneficial for the radioactivity uptake on the particle [21].

The density of the particle was found by settling in water. When the particle is submersed in water the pores will be filled with water. The density is measured in the group to be between 1068 and 1120 kg m^{-3}.

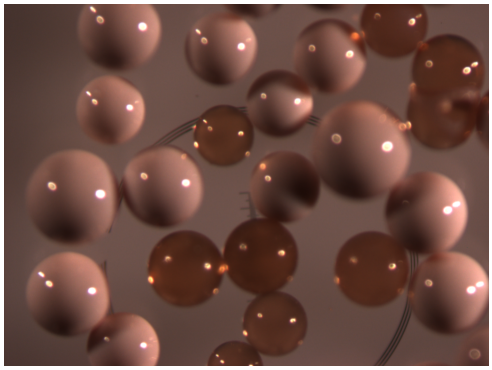

Figure 5.5: Picture of the Amberlyst A21 Hydroxide Form particles taken in a microscope

5.2.1 Labelling the Particle

The tracer particle is labelled by an indirect labelling technique. By the labelling procedure used in this project the activity on the particles could reach 450-1440 μCi [21]. When labelling the tracer particles they were brought into a 0.6 mL ^{18}F-water solution, which was then shaken for about 10 minutes while ^{18}F attach to the porous particle surfaces. The activity on the particle after labelling depends on the concentration of ^{18}F in the water solution. The activity on each particle depends on how many particles that were inserted in the fluoride solution. All particles in the batch gained equal activity from the radioactive water, hence the more particles the lower activity on each particle.

Chang et al. [21] measured the activity on the particle by measuring the effective cut-points, the final cut-points used to determine the particle position, of a particle in water for 30 seconds. As seen in Figure 5.6 there is no drop in effective cut-points during the 30 seconds. This confirms that the activity on the particle does not leak out into the water during a long time period and that the radionuclide, ^{18}F, by a indirect labelling technique form a stable bond with the particle.

5.2.2 Detecting the Particle

Hundreds of small γ-ray detectors in the PET-scanner detect the back-to-back γ-ray pairs emitted from the tracer particle. Detection of a back-to-back γ-ray pair defines a line of response that indicates that the β^+ decay event happened some place along the line.

The PET scanner at Haukeland University Hospital is a Siemens TruePoint scanner, Figure 5.7, which has an energy window of 425-650 keV. There are three rings in the scanner and each has a diameter of 855.2 mm and consists of 48 sensor blocks. In each block there are 13 $\times$ 13 Lutetium Oxyorthosilicate (LSO) scintillator crystals, with size $4 \times 4 \times 20$ mm. A crystal gap between every block separate them in the axial and radial directions. The rings have 672 crystals each in the radial direction; 48 crystal gaps and 13 $\times$ 48 crystals. In the axial direction there are in total 41 crystals; 2 crystal gaps and 3 $\times$ 13 crystals. This makes the length of the field of view 164 mm in the axial direction [21]. Due to high density the scintillation detectors provide high stopping efficiency for γ-rays (511 keV photons), they also provide good energy resolution [20]

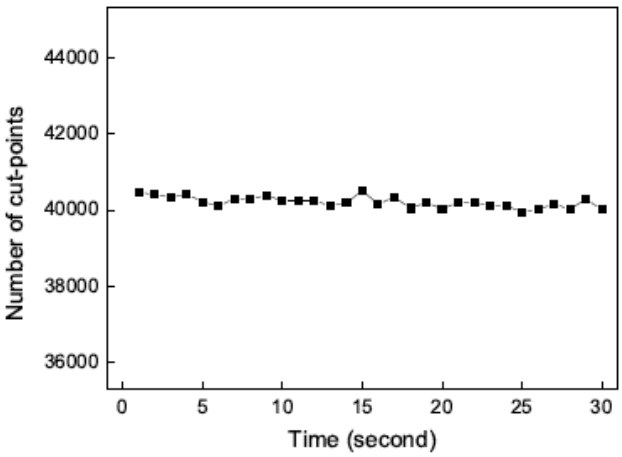

Figure 5.6: The effective cut-points of a particle in water for 30 seconds taken from [21] p. 13. The number of effective cut-points do not drop which means that the activity on the particle does not leak out into the water

The coincidence window for the Siemens TruePoint scanner is 4.5 nanoseconds. This

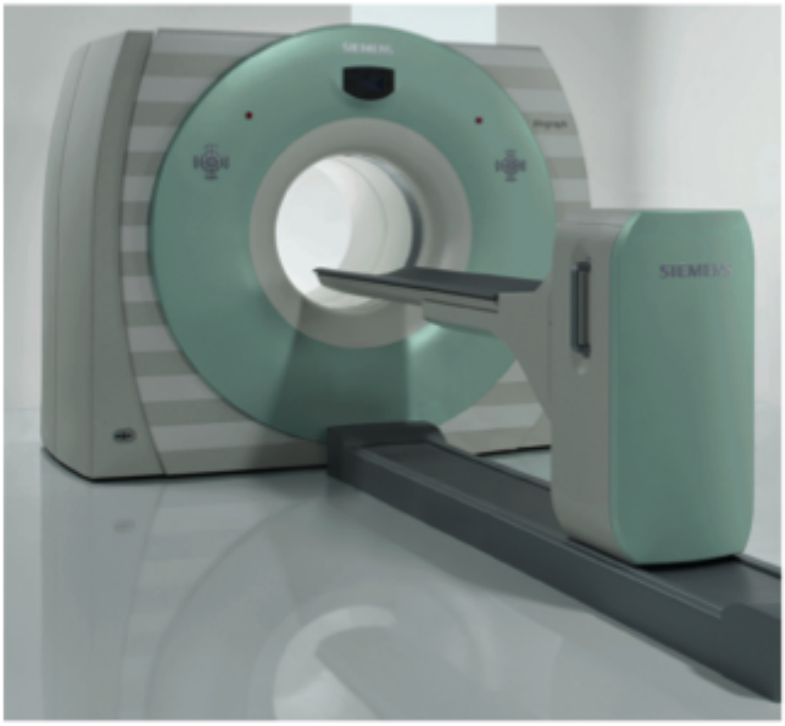

Figure 5.7: The Siemens TruePoint PET [1] scanner used to perform the experiments in this project

[1] http://www.medicalexpo.com/prod/siemens-ag-healthcare-sector/x-ray-ct-scanners-combined-with-pet-scanners-for-full-body-tomography-70075-430731.html

means that if two photons are detected by two sensors within this narrow time window, they are considered to come from one annihilation.

Data generated from the scanning gives the locations of two sensors that have detected an event, then a LOR can be drawn between the two sensors. The LOR's location is the base of the PEPT algorithm. Figure 5.8 shows LOR's recorded in a small time window, the crossing points called the cut-points are scattered and must be smoothed in order to locate the particle [21]. The PEPT algorithm, Section 5.4.1, is designed to eliminate false LOR's that is not eliminated in the coincidence window. These events are called random coincidences.

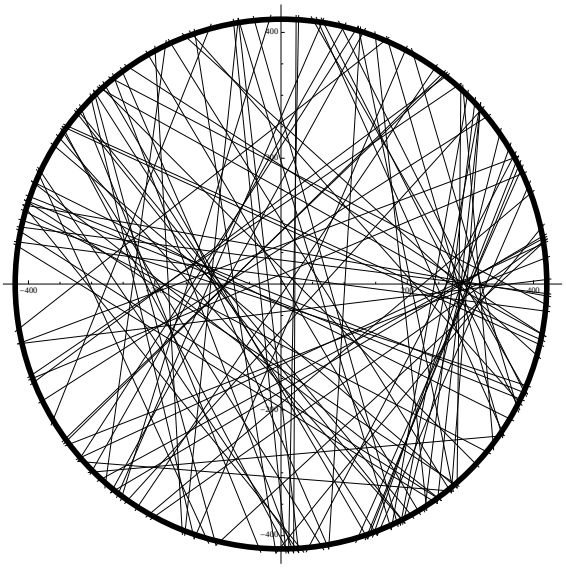

Figure 5.8: LOR's obtained from a millisecond of data logging

5.3 The Experiment

The experiments were performed at the radiology department at Haukeland University Hospital with assistance from the radiochemists for preparing the tracer particle and operating the PET camera, Figure 5.9. The PET camera was running for 90 and 120 seconds, depending on the underflow opening, 90 seconds was used for experiments with closed underflow and 120 seconds for the rest, Table 5.2. The procedure for the experiment was as follows:

- label the particle
- start the pump
- set the preferred flow rate and underflow
- start the PET scanner
- inject the tracer particle
- stop the pump when the PET scanner is finished

- use a dosimeter to detect were the tracer particle is in the system
- (remove the tracer particle, if possible)

In order to minimize the start up effect of the pump it was started a while before the particle injection allowing the flow to stabilise. The flow rate and underflow were adjusted to the preferred value, and the particle was injected into the cyclone system while the PET camera was running. The pressure and the temperature in the system was supervised.

A dosimeter was used to determine the position of the tracer particle when the experiment was terminated. If the particle was in the underflow box it could be extracted out through an outlet. If the particle was in the tank it was not extracted because it was a lot of work to remove the particle from the tank without changing all the fluid in the system. There was also minimal chances that the newly injected particle and the one in the tank would pass through the FOV at the same time.

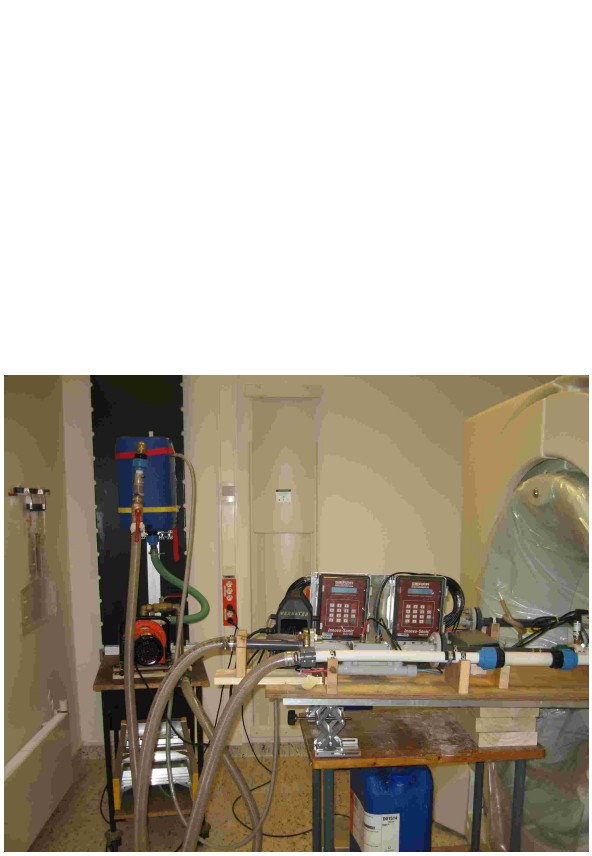

Figure 5.9: Pictures of the rig in the PET camera

25 experiments were executed in this thesis, Table 5.2. Several more experiments were performed but they gave insufficient results and were discarded. The insufficient results were usually due to too few detected LOR's. Few LOR's indicate either low activity on the particle or leakage of the activity into the fluid, which in both cases gave insufficient results and a particle trajectory could not be obtained. This was experienced when salt solution was used as fluid.

Table 5.2: List of experiments

Experiment nr.	Fluid	Flow rate [m^3h^{-1}]	Underflow (%)
1	Water	3.4	10
2	Water	3.4	10
3	Water	3.4	10
4	Water	3.4	10
5	Water	3.4	10
6	Water	2.8	5
7	Alginate (20 cP)	3.3	5
8	Alginate (20 cP)	3.3	5
9	Alginate (15 cP)	3.3	5
10	Alginate (15 cP)	3.3	10
11	Alginate (15 cP)	3.3	0
12	Alginate (10 cP)	3.3	5
13	Alginate (5 cP)	3.3	5
14	Alginate (5 cP)	3.3	10
15	Salt water solution	3.4	5
16	Salt water solution	3.4	10
17	Water	2.0	0
18	Water	3.4	0
19	Water	3.4	0
20	Water	3.0	5
21	Water	3.0	10
22	Water	2.1	0
23	Water	2.1	10
24	Water	2.1	24
25	Glycerol solution	3.2	22

5.3.1 Viscosity and Density Modifiers

Alginate and glycerol were used to increase the viscosity of the fluid. Alginate was used to get high viscosity fluids and glycerol was used to slightly increase the viscosity of the fluid. A salt water solution was used to get approximately neutral density between the particle and the fluid.

Alginate

Alginate has negligible impact on the density of the fluid and has a large effect on viscosity of water solutions in small concentrations. Several viscosities were prepared with alginate solution. For a viscosity of approximately 20 cP 0.6 weight% alginate was needed.

The alginate-water solution is slightly shear thinning which could be a problem. Shear thinning means that the effective viscosity changes due to the shear stress the fluid is exposed to, i.e. increased shear reduce the viscosity. In [44] the shear thinning of alginate was tested which confirmed the shear thinning effect in alginate-water solution varying

from approximately 21 cP to 15 cP for a shear rate of 1 to 1000 s^{-1}. Since the shear stress in the hydrocyclone vary there would be different viscosities in different parts of the hydrocyclone which could be a source of error in the experiments.

The experiments with highest viscosity (20 cP) were executed first. Afterwards a third of the high viscosity fluid in the hydrocyclone system was replaced with pure water to get a viscosity of approximately 15 cP. For the next experiments half of the fluid in the system was replaced with pure water to get lower viscosity. Thus the different values of the viscosities should be seen as estimates but the ratio between them should be reliable.

Glycerol

Glycerol was used as a viscosity modifier in one of the experiments. A small amount of glycerol was mixed into the water to slightly increase the viscosity in order to see if it had an effect on the particle trajectory.

A cone and plate rheometer was used to find the viscosity of the glycerol-water solution. In a cone and plate rheometer the water solution is placed on a plate and a shallow cone is placed on top of it. The angle between plate and cone is typically 1°. To measure the viscosity one of the plates are rotated while the other is kept still and the force needed to obtain a specific rotational speed is measured.

Salt Water Solution

The preferable solution to modify the density of the fluid, but not the viscosity, turned out to be a sodium chloride (NaCl) solution, also called a salt water solution [44]. To get a solution with density equal to the tracer particle approximately 16 weight% sodium chloride was needed.

In the neutral density particle experiments several particles were injected at the same time and the PET scanner was continuously detecting them for 5 to 6 minutes.

5.4 Data Analysis

Several parameters of the experimental results have been analysed. The particle trajectory was studied to see if the increased viscosity had an impact on the particle flow pattern. The radial and axial positions of the tracer particle and the time the particle spends in each part of the cyclone have been studied. This have been done to achieve a better understanding of the particle flow and to detect flow abnormalities in the hydrocyclone. Axial and tangential velocity profiles have been analysed by comparing them with theory for the flow pattern and for models of the flow. The Burgers model of flow, Equation (2.9), has been used to fit the tangential velocity profiles. The velocity variations over time in the hydrocyclone have also been analysed.

5.4.1 The Algorithm

The PEPT algorithm determines the position of the tracer particle throughout the hydrocyclone. The program was adapted and implemented in a Fortran program from the algorithm developed by Hoffmann et al. [24]. The position of the tracer particle is determined every millisecond. Data for calculating the coordinates of the two sensors is

first read into a list-mode by the program. LOR's and their 2D cut-points are obtained from the coordinates. A reference point is then determined by averaging the position of all the cut-points. Cut-points at a distance further away from the point than a specific distance are eliminated. The averaging and elimination of cut-points continue in turns several times until the spatial window is narrowed down to a few square millimetre. LOR's had to have at least one cut-point in the current averaging window or it would be eliminated. Finally, to determine the position of the tracer particle in the plane the positions of the remaining cut-points are averaged.

The number of LOR's and cut-points in the final average depends on the location of the tracer particle in the field of view in the scanner, and on the activity on the tracer particle. To get the position in three dimensions the cut-points between the LOR's remaining after the elimination process described above is averaged [21].

5.4.2 Gaussian Filter

Signals from the PET scanner can be scattered due to disturbances in the field of view. This can come from Compton scattering or pair production. The PEPT algorithm remove some of the corrupt signals, but does not take care of the scattering. It is of interest to smooth out the signals so that the scattering is filtered out. For this project a Gaussian filter has been used for smoothing.

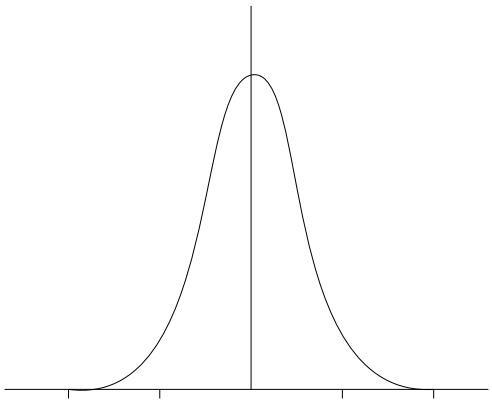

Figure 5.10: The Gaussian function weigh the points according to the distance from the original point

In a Gaussian filter the points are set to a weighted average of it's neighbouring points. The original point is heaviest weighted, then the neighbouring points get less weight as the distance from the original point increase, Figure 5.10 [45].

5.4.3 Other Programs Developed for Analysis of the Particle Tracks

An algorithm to determine the particle position and the velocities in cylindrical coordinates has also been developed in the group. The program determines the center axis of the hydrocyclone. This is done by finding the cyclone axis as the line minimising the sum of the squared distances of all the particle positions during the period that the particles are in the cyclone body.

A Fortran program for fitting the tangential velocity of the particle to the Burgers vortex equation (2.9) has also been developed in the group.

Chapter 6

Numerical Setup

Over the last decades a new approach for solving fluid dynamic problems has been developed; the numerical method. The numerical method serves as a supplement to real experiment and theory. The numerical models have improved over the years but cannot fully replace either theory nor experiments. In this thesis Computational Fluid Dynamics (CFD) simulations have been used to supplement the experiments and to further explain and validate the experimental results. The particles have been simulated by using the Lagrangian Multiphase model and the turbulence in the hydrocyclone was modelled by using large eddy simulations (LES).

6.1 Computational Fluid Dynamics

Pure experiments and pure theory has been used to study fluid dynamics for most of the twentieth century, but high speed digital computers along with accurate numerical algorithms for solving physical problems open a new possibility in the field. Computational fluid dynamics is the third approach for studying fluid dynamics.

Today, analysis and solutions of fluid dynamic problems consist of equal parts of experiments, theory and CFD, Figure 6.1. CFD is the newest approach in the fluid dynamics but can never replace either the experiments nor theory. It can, however, be of use for understanding and interpreting the theory and the experiments, and vice versa [46].
CFD is based on the three fundamental governing equations in fluid dynamics:

1. The continuity equation, mass is conserved.
2. The momentum equation, Newton's second law, F=ma.
3. The energy equation, energy is conserved.

The integrals and partial derivatives in these three equations are replaced with discrete algebraic forms in CFD. The discrete algebraic forms are then calculated to get values of the flow field in time and/or space at discrete points [46]. The CFD program continues to iterate until it comes to a solution that satisfy the initial conditions and the stopping criteria set for the problem. CFD are dependent on high speed computers because the solutions to the numerical problems generally require calculation of many thousands (or millions) of numbers, a task impossible to humans.

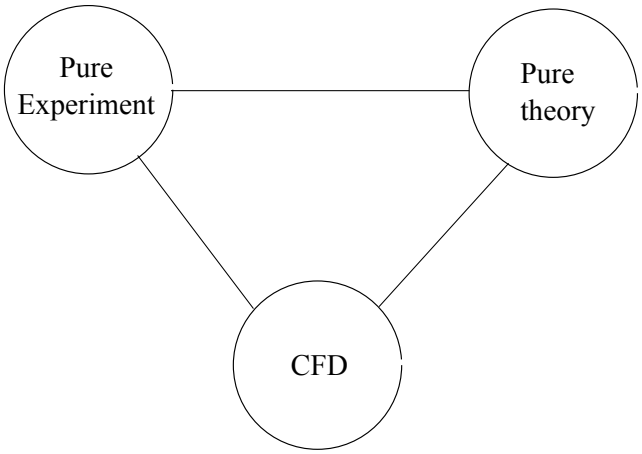

Figure 6.1: The three approaches for solving fluid dynamics, pure experiments, pure theory and computational fluid dynamics adapted from [46]

6.2 CFD Software and Numerical Model

The commercial CFD program STAR-CCM+ version 6.06.017 from CD-Adapco was used for the computational simulations. The program includes a large number of different models for simulations of the flow. The program also has a built in Computer-aided design (CAD) model for construction of simple shapes and more complex geometries, and provides several meshing models so that the calculations can be very accurate at important parts of the model.

6.2.1 Developed Numerical Model

The first that was done when developing the simulation model in STAR-CCM+ was to draw the geometry in the CAD program. The cyclone was first drawn in two dimensions, Figure 6.2, then revolved to get it in three dimensions.

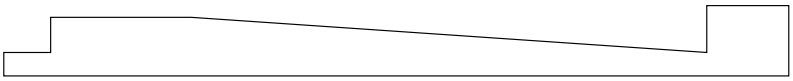

Figure 6.2: The 2D-drawing of the hydrocyclone drawn in the Star-CCM+ CAD program

The overflow and underflow were extruded from the drawn 3D-model to get the complete geometry, Figure 6.3. Then the boundary conditions for the different faces were decided.

When building the grid for the simulation the grid models had to be selected. In the developed simulation model the following grid models have been used:

- Prism Layer Mesher
- Surface Remesher

- Trimmer

To set the cell size of the grid in the simulations a grid dependency test was carried out. The cell size were varied from 1.0 to 2.0 mm with an interval of 0.5 mm. The coarsest grid, which gave little variation in the inlet velocity, was chosen. Simulations with this grid size also gave converting residuals. Residuals are the difference between one iteration and the iteration before.

From the results of the grid dependency test, Table 6.1, the base size of the grid was set to 1.5 mm, Figure 6.3. The grid in the inlet was refined to be 45% of the grids base size, Figure 6.4, because it is an advantage with a finer grid in the inlet when injecting particles into the flow.

Table 6.1: Results from the grid dependency test. The base size of the grid was set to 1.5 millimetre. This was the coarsest grid that gave negligible difference in inlet velocity.

Experiment	Base size [mm]	Cell amount	Inlet velocity [m s^{-1}]
1	2.0	116619	3.8421
2	1.5	251193	3.8434
3	1.0	777128	3.8432

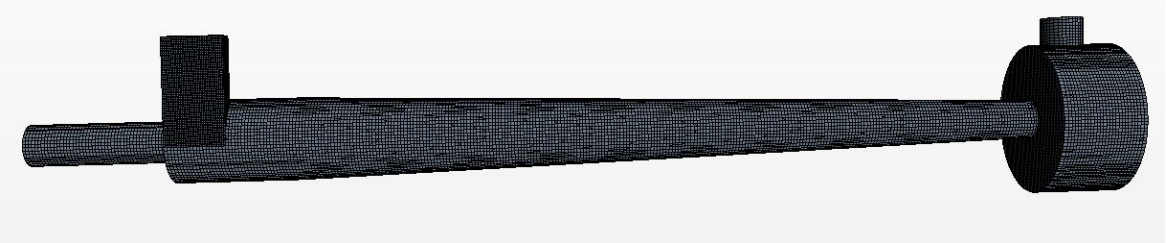

Figure 6.3: Illustration of the grid used for CFD simulation. The base size of the grid was set to 1.5 mm

The flow in the cyclone was modelled as a liquid with constant density and with segregated flow. The turbulence in the cyclone was modelled with large eddy simulation.

The LES model solves a filtered form of the continuity equations and momentum equations for the larger scales in the flow to avoid the problem of solving the turbulence field over the spectrum of length scales. For the smaller scales in the flow an eddy viscosity model is applied. Flow fields generated by LES models are used for simulations with particle trajectories and dispersion patterns [47].

LES was used for the simulations because it simulates the particle transport much more realistic than the Reynolds-averaged Navier-Stokes (RANS) model, and the particle trajectories do not need further modelling [36]. It is difficult to simulate the complexity of the two flow vortices when turbulence and flow abnormalities such as EoV is taken into account. J.J. Derksen [36] and Cortès and Gil [8] studied several different simulation models to determine which of the models gave sufficient results compared to real

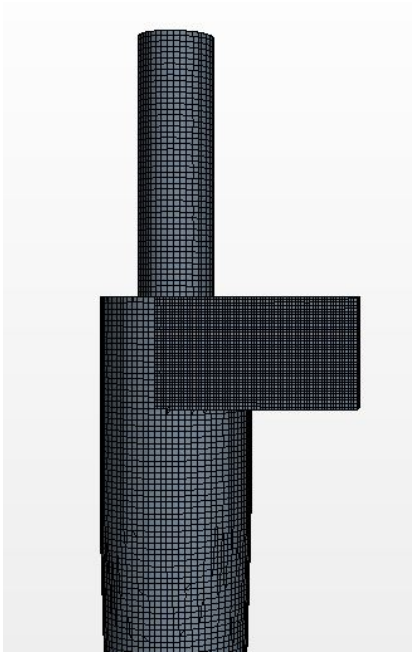

Figure 6.4: Illustration of the refined grid in the inlet of the hydrocyclone. The base size of the grid is 1.5 mm and the inlet is refined to be 45% of the base size

experiments. In both cases LES was concluded to be a good model for simulating the complex flow in cyclones.

The simulations were solved with an implicit unsteady solver with a time step of 0.01 seconds and with second-order discretisation.

Particle Tracking

The injected particles in the flow was simulated with the Lagrangian multiphase model. The particle was modelled as a solid spherical particle with diameter of 500 μm and a constant density of 1070 kg m^{-3}. The diameter and the density was measured in the group.

The particles were modelled with two-way coupling and the drag force was calculated by the Sciller-Naumann drag coefficient. The particles were modelled with constant velocity and flow rate. After the simulations were finished the particle trajectories were filtered until one single trajectory was left in the hydrocyclone.

6.3 Numerical Simulations

Several parameters were varied for the simulations according to the experiments that were simulated, Table 6.2. The simulated experiments were a selection of experiments with varying underflow, fluid, inlet velocity and inlet pressure.

The simulation of experiment 21 was run twice, the second time for a longer physical time, for validation of the result.

Table 6.2: Simulated experiments by CFD. A selection of experiments with varying underflow, fluid, inlet velocity and inlet pressure

Experiment	Viscosity [cP]	Flow rate [$m^3\ h^{-1}$]	Inlet velocity, v_{in} [$m\ s^{-1}$]	Inlet pressure [bar]	Underflow % of the flow rate	Physical time [s]
3	1.01	3.4	3.05	1.00	10	2
9	15	3.3	3.63	0.78	5	2
11	15	3.3	3.38	0.79	0	2
17	1.01	2.0	3.22	0.40	0	2
21	1.01	3.0	3.15	0.7	10	2
21	1.01	3.0	3.15	0.7	10	5
25	1.40	3.2	1.85	1.0	22	2

Chapter 7

Results and Discussion

The particle trajectories obtained from the experiments in this thesis show that it is possible to follow a high-speed particle through a flow field. This is also showed by e.g. Hoffmann et al. [24] and previously in this project by Chang et al. [21]. Investigation of the particle trajectories promotes understanding of the complex flow field in the hydrocyclone.

Different flow abnormalities have been detected in this thesis. By studying the conditions of the experiments the flow abnormalities can to some extent, be predicted. This is important in further development of cyclone design and in finding the optimal operating conditions for cyclones in the industry.

In this thesis the experiments differ in several operating conditions in order to investigate the influence of the parameters. The fluids viscosity along with the underflow conditions appear to be the parameters with highest influence on the flow abnormalities in the experiments performed.

The numerical simulations coincide well with the experimental results and the flow abnormalities observed in the experiments can also be seen in the CFD simulations.

The results from a representative selection of the 25 experiments, marked * in Table 7.1, are presented in this chapter. The rest of the results are presented in Appendix A.

Table 7.1: Overview of all the experiments. The viscosity and flow rates were known, the inlet velocity, inlet pressure, the overflow and underflow pressure were found by the PEPT algorithm. Reynolds number were calculated from the results. Experiments marked * are presented in this chapter

Experiment	Viscosity [cP]	Flow rate [m^3h^{-1}]	Inlet velocity v_{in} [m s^{-1}]	Inlet pressure [bar]	Overflow pressure [bar]	Underflow pressure [bar]	Reynolds number
1	1.01	3.4	2.9	1.20	0.54	0.53	57426
2	1.01	3.4	3.16	1.20	0.54	0.53	62574
3*	1.01	3.4	3.05	1.00	0.28	0.27	60396
4	1.01	3.4	3.6	0.98	0.21	0.24	71287
5	1.01	3.4	1.83	0.10	0.05	0.09	36238
6	1.01	2.8	2.95	0.50	0.15	0.17	58416
7	20	3.3	1.89	0.75	0.20	0.39	1890
8	20	3.3	2.79	0.75	0.20	0.39	2790
9*	15	3.3	3.60	0.78	0.21	0.35	4800
10	15	3.3	3.49	0.78	0.20	0.31	4653
11*	15	3.3	3.38	0.79	0.22	0.35	4507
12	10	3.3	3.75	0.80	0.20	0.29	7500
13	5	3.3	3.90	0.80	0.19	0.25	15600
14	5	3.3	2.95	0.80	0.18	0.24	11800
15*	1.01	3.4	3.21	0.81	0.17	0.24	63564
16*	1.01	3.4	3.61	0.99	0.25	0.31	71485
17*	1.01	2.0	3.22	0.40	0.11	1.50	63762
18	1.01	3.4	3.05	0.81	0.18	0.20	60396
19	1.01	3.4	3.52	0.81	0.17	0.20	69703
20	1.01	3.0	3.42	0.63	0.01	0.205	63477
21*	1.01	3.0	3.15	0.7	0.01	0.226	60702
22	1.01	2.1	1.90	0.4	0.01	0.151	40008
23	1.01	2.1	2.53	0.4	0.01	0.15	53761
24	1.01	2.1	2.09	0.5	0.01	0.25	46106
25*	1.40	3.2	1.85	1.0	0.2	0.425	26395

7.1 The Particle Trajectories

The particle trajectories in the hydrocyclone are obtained by the PEPT algorithm developed in the group, and presented in both a Cartesian coordinate system and in a cylindrical coordinate system. The numerical CFD trajectories are simulated by the developed numerical model in STAR-CCM+.

The center of the cyclone is determined in order to express the particle positions and velocities in cylindrical coordinates. As seen in Figure 7.1, the center of the hydrocyclone is in the origin of the coordinate system. The radial, tangential and axial positions of the particle and the velocities in radial, tangential and axial directions can be obtained from the cylindrical coordinates.

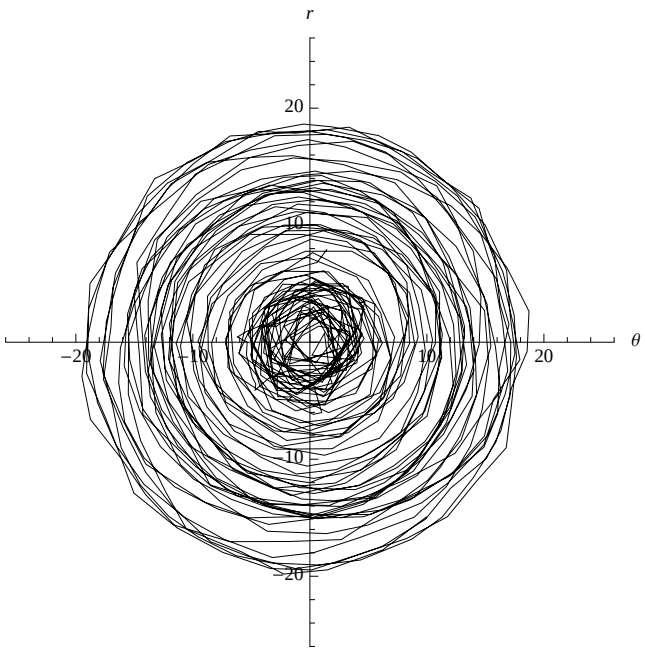

Figure 7.1: Cylindrical coordinates radial, r, and tangential, θ, positions plotted from experiment 21. The center of the hydrocyclone is in the origin

The 2D-trajectory of the particle in the hydrocyclone is obtained as a plot of the axial position and the radial position of the particle. The particle trajectory presented in 2D-view gives a better understanding of the particle movements in the hydrocyclone.

The 2D-trajectories presented are smoothed by a Gaussian filter, Section 5.4.2, to discard scattering in the obtained trajectories. Most of the small peaks are smoothed out and the plot gives a better view of the particle movements. The trajectory line is, however, still slightly uneven which can be due to turbulence in the hydrocyclone.

The complex flow in hydrocyclones is difficult to simulate properly but by use of the LES model the turbulence flow in hydrocyclones can be simulated [8, 36]. The small fluctuations in the trajectory line can also be seen in the simulated 2D-trajectory of experiment 3, Figure 7.4. The plot is not smoothed but small fluctuations are observed that might be due to turbulence in the flow.

7.1.1 Flow Abnormalities Observed

The trajectories obtained show that the particle tracks varies in all the experiments. Some trends in the particle trajectories can, however, be observed.

In most of the trajectories a flow abnormality was observed some distance into the hydrocyclone, Appendix A. The particle moves into the inner vortex and upwards before emerging back out to the outer vortex and continue downwards again. The length the particle travels before turning and how many circles it turns vary between the experiments. The flow abnormality was observed in all the CFD simulations as well. As seen in Figure 7.2 there is a good correlation between the experimental and the numerical results. The flow abnormality exists around the same place in the hydrocyclone both in the CFD simulations and in the experimental trajectories.

The flow abnormality appears to come into existence, in some form, at almost the same place in all the experiments. The geometrical shape shift between cylindrical and conical sections appear to have some effect on the abnormality in the particle flow. Even though the abnormality varies between large and small circles it always appears around the same place in the hydrocyclone. The change in geometry might alter the flow pattern in the hydrocyclone, which causes the particle to move more easily into the inner vortex.

Two main abnormalities in the flow have been detected in this thesis. The flow abnormality at the geometrical shift in the hydrocyclone, from here on called the flow abnormality, and the end of vortex at the lower part of the conical section in the hydrocyclone.

As already stated there is a good correlation between the experimentally obtained particle trajectories and the ones simulated with CFD, which also were observed in the 2D-trajectories. The flow abnormality in experiment 3 can be seen in both the experimental particle trajectory, Figure 7.3, and in the simulated particle trajectory, Figure 7.4. The particle behaves similar in both the length of the flow abnormality and the place where it comes into existence.

The experiments which differs in viscosity and flow rate can be compared to one another by use of the Reynolds number, Equation (2.18). Experiments that differ in underflow opening can, however, not be compared due to the changes in flow pattern and the fact that the underflow settings are not taken into account in the Re. When comparing experiments with similar Re and equal underflow some trends in the flow pattern can be detected.

Experiments 1, 2, 3, 4 and 21 have similar Re and an underflow opening of 10% of the flow, Table 7.1. The particle trajectories for these experiments are rather similar, Appendix A. The flow abnormality is not present or small in all the trajectories, there are also no other flow abnormalities in the trajectories. The trajectories in experiment 3 and 21 are more similar, compared to experiment 1, 2 and 4, due to the existence of the flow abnormality. The experiment 1, 2 and 4 lack the flow abnormality. Experiment 1, 2 and 4 were executed with the exact same conditions and the particles behaved very similar. Experiment 3 and 21 were also performed by approximately the same conditions, but with a slightly difference in flow rate and the particle behaved very similar. This means that even though the particle trajectories appear to vary between the experiments some similarities have been observed in experiments executed with the same conditions

The EoV is present in experiment 17, 18, 19 and 22. These experiments were per-

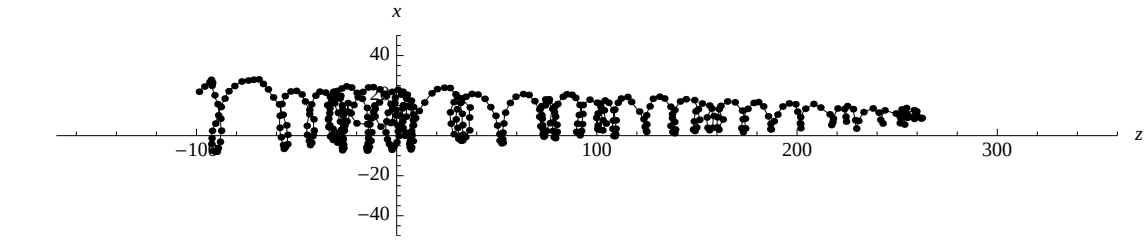

(a)

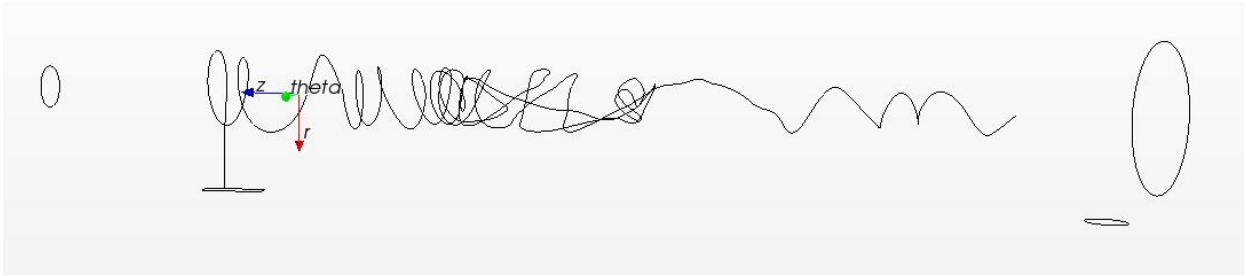

(b)

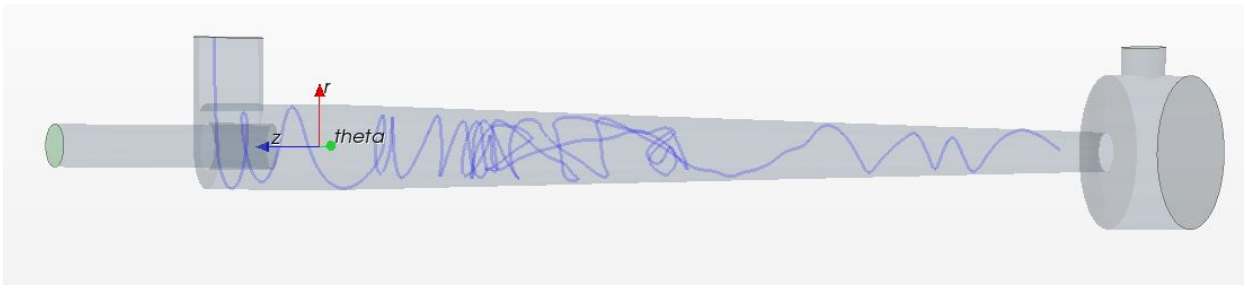

(c)

Figure 7.2: The trajectory in a) is from experiment 3 with 10% underflow and a volume flow rate of 3.4 m^3h^{-1}, presented in a Cartesian coordinate system. The trajectory in b) is from the numerical simulation and image c) shows the numerically computed track inside the cyclone

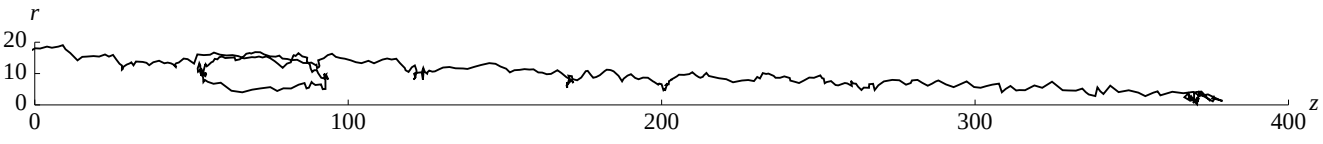

(a)

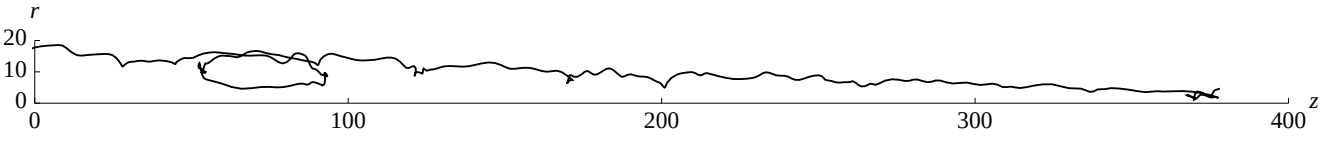

(b)

Figure 7.3: The trajectory in a) is the 2D-trajectory of experiment 3 and the trajectory in b) has been smoothed by Gaussian filter both is presented in cylindrical coordinates

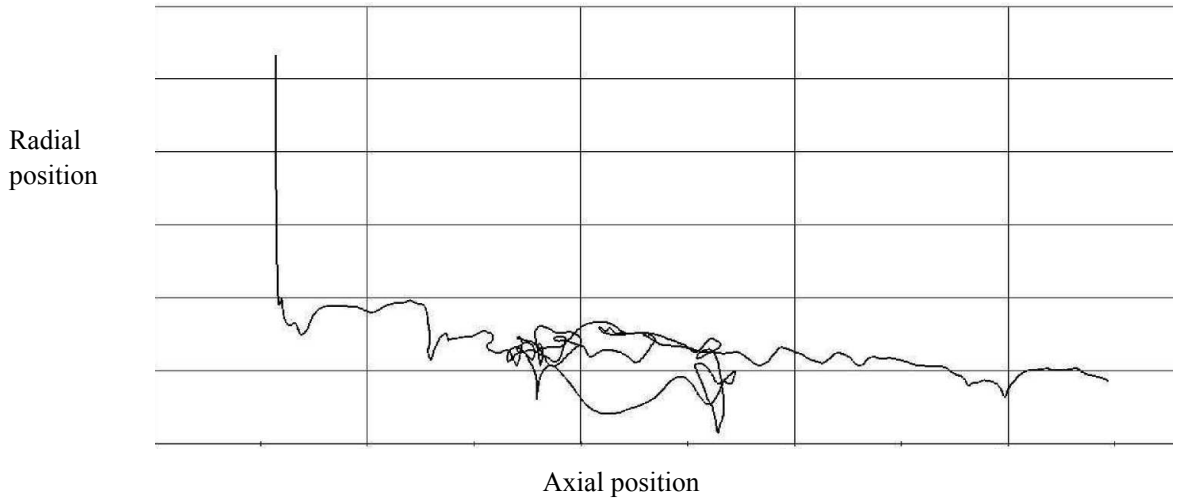

Figure 7.4: 2D-trajectory from CFD simulation for experiment 3 presented in a cylindrical coordinate system

formed under almost equal conditions and they all produced the end of vortex phenomena. The trajectories only differ where the EoV comes into existence. In experiment 18 and 19 it becomes existent higher in the conical section than in experiment 17 and 22. This might be due to the differences in flow rate. The two experiments where the EoV exists higher in the conical section were carried out with a higher flow rate.

7.1.2 Effect of Viscosity

Experiments preformed with increased viscosity have a lower Re than the ones with lower viscosity, which is natural. The overall tendency in the experiments with higher viscosities is that the observed flow abnormalities are larger than in the low viscosity experiments. There are also similarities between experiments with similar Re and equal underflow, for instance experiments 7, 9 and 12. The Re varies slightly for these experiments due to the differences in viscosity, from 20 to 10 cP, but the particle trajectories are fairly similar. Experiment 8 and 11 also have fairly similar particle trajectories and Re but the underflow opening differs, which changes the flow pattern. The similarities in these two experiments are probably due to the particle size relative to the cutsize of the hydrocyclone.

Although most of the experiments experience the flow abnormality, the length and circles vary. Some trends can, however, be observed. In the experiments where the fluid is water (low viscosity), Figures 7.2 and 7.13, the flow abnormality is significantly shorter than in experiments with higher viscosity, Figure 7.5. A reason might be that the particle used in the high viscosity experiment was much smaller and lighter than the one used in the low viscosity experiments.

Another reason might be that the viscosity of the fluid made an impact on the flow abnormality. The circulative movement is larger and more distinct in each of the experiments with high viscosity (15 cP or higher). In [44] it was observed that the experiments with higher viscosity had significantly increased residence time. The flow abnormality observed in experiments with high viscosity is consistent with this observation. When

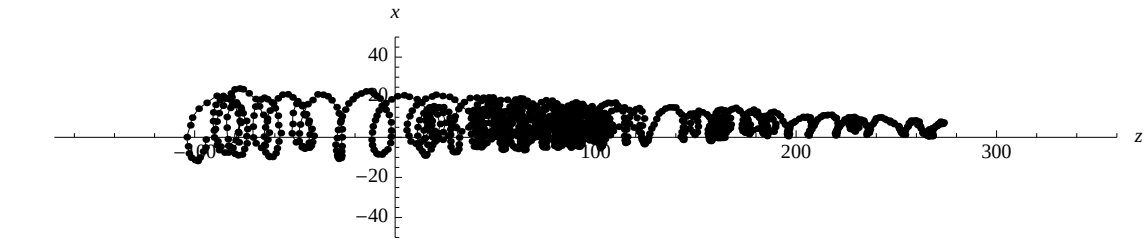

(a)

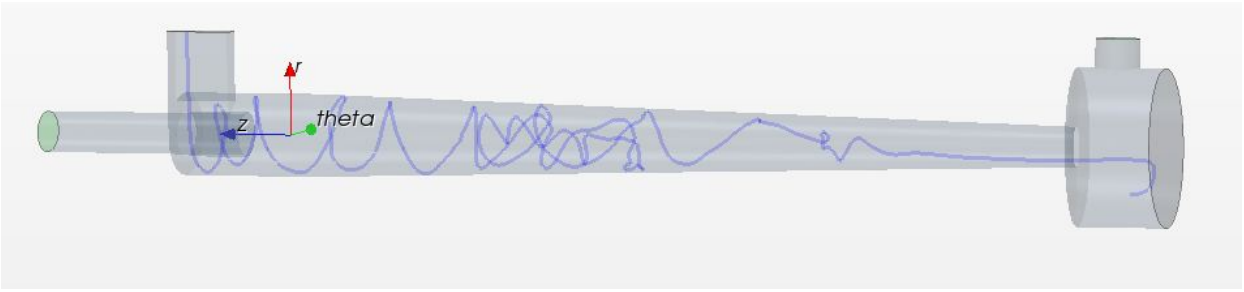

(b)

Figure 7.5: The trajectory in a) is from the experimental result of experiment 9 with 5% underflow and a volume flow rate of 3.3 m^3h^{-1}, presented in Cartesian coordinates. The trajectory in b) is obtained from the CFD simulation of experiment 9

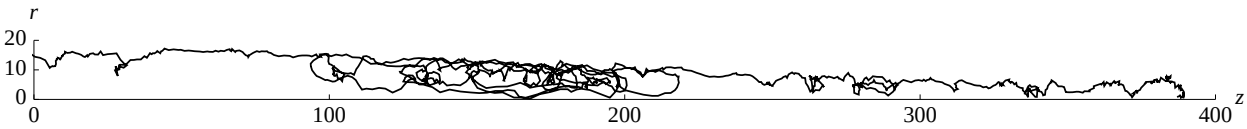

(a)

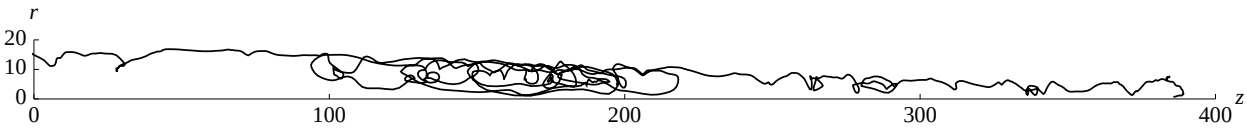

(b)

Figure 7.6: The trajectory in a) is the 2D-trajectory of experiment 9 and the trajectory in b) has been smoothed by Gaussian filter both presented in cylindrical coordinates

the particle circulate the residence time will be prolonged for the particle through the hydrocyclone. In [15] it is found that the cutsize increases with increasing viscosity which can be observed in Figure 2.13. This might be the reason for the larger flow abnormality in the high viscosity experiments. As seen in Figure 2.11 the particles with a diameter equal to the cutsize lies on the locus of zero vertical velocity. It is fair to believe that particles with diameter close to the cutsize, due to high viscosity fluid, is easier moved between the two vortices.

Particle trajectories similar to the particle trajectories obtained in this thesis was observed by Wang et al. [26]. They observed that the particle with the longest residence time behaved like the ones discussed earlier; it moved in circles in the inner and the

outer vortex before descending to the underflow. Wang et al. thought the reason could be that the particle fell into the locus of zero vertical velocity and that fluctuating radial velocity due to turbulence in the hydrocyclone flow made the impact on the particle. Observations of this behaviour was mainly for small particles.

The observations in [26] are interesting and might explain the unexpected flow abnormality. The particles may fall into the locus of zero axial velocity and follow the inner vortex flow some distance before entering the outer vortex flow again. An investigation of Figures 7.15 and 7.6 give rise to the thought that a smaller and lighter particle, or a particle that appear lighter in the fluid, will fall into the inner vortex more frequently and stay there longer before emerging to the outer vortex, compared to a larger particle.

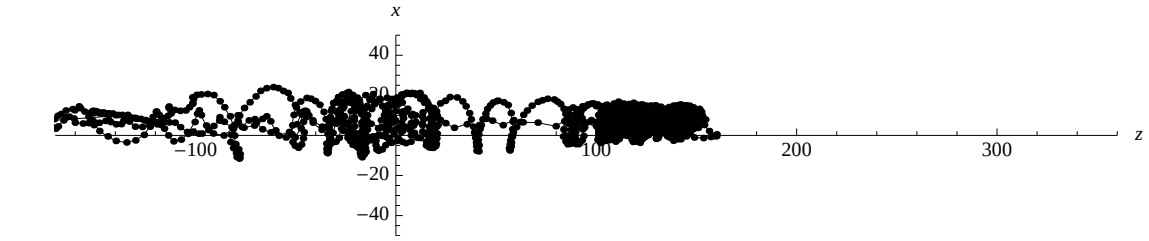

(a)

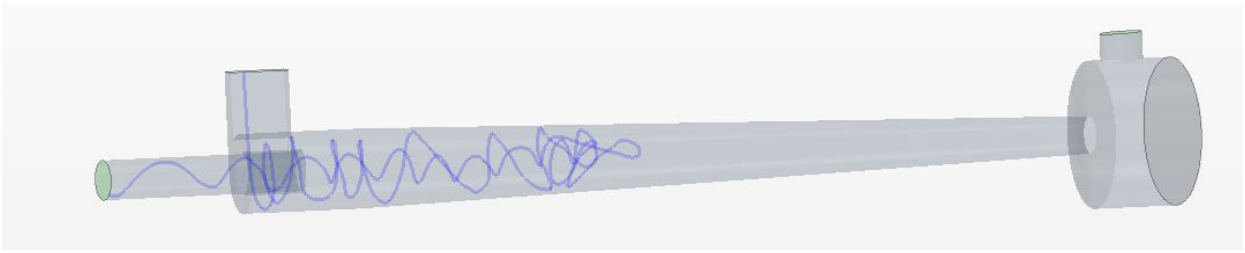

(b)

Figure 7.7: The trajectory in a) is from the experimental result of experiment 11 with 0% underflow and a volume flow rate of 3.3 m^3h^{-1}, presented in a Cartesian coordinate system. The trajectory in b) is obtained from the CFD simulation of experiment 9. The particle exits through the overflow both in the experiment and in the CFD simulation

In experiment 11, Figures 7.7 and 7.8, the particle follows the outer vortex some distance into the cyclone before it moves inward, enters the inner vortex and exits through the overflow. This was an unexpected behaviour for this experiment according to the settings. The particle was expected to follow the outer flow all the way down the cyclone body and exit out through the underflow. Experiment 11 had a high viscosity fluid of 15 cP and the reason for the unexpected behaviour can be connected to the high viscosity. In Figure 2.13 it can be observed that the cutsize increases with increasing viscosity [15].

The Stokes number, Equation(2.19), for the experiments in [15] were calculated for use in calculation of the cutsize in the hydrocyclone for this thesis, so-called Stokesian scaling, Section 2.7. The Stokes number for x_{50} is approximately the same over a wide range of Re. This is why the Stokes number is important for scaling of hydrocyclones and cyclones [2].

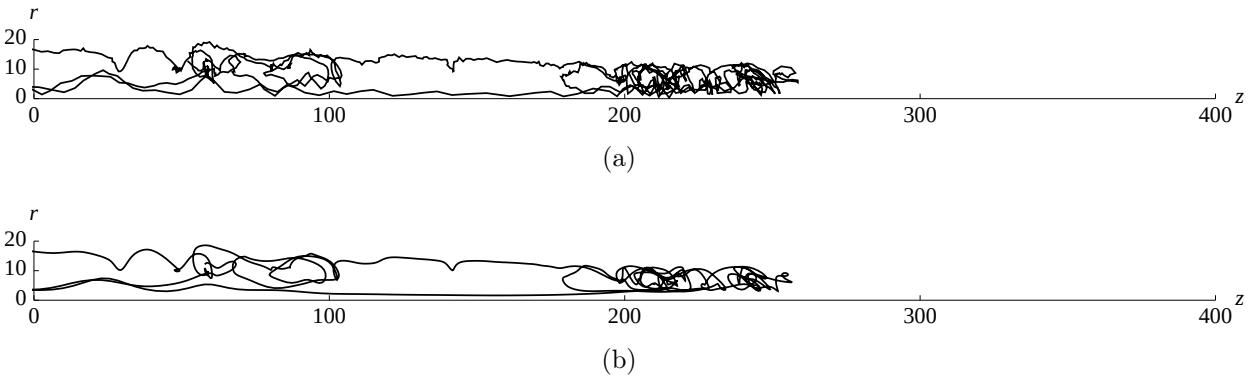

Figure 7.8: The trajectory in a) is the 2D-trajectory of experiment 11 and the trajectory in b) has been smoothed by Gaussian filter. Both trajectories are presented in a cylindrical coordinate system

Table 7.2: Experimental data taken from [15] p. 64 and the calculated Stokes number, Equation (2.19), for an experiment with μ equal to 15 cP (0.0151 kg (ms)$^{-1}$).

Property	Viscosity 15 cP
ρ [kg m^{-3}]	1224
ρ_p [kg m^{-3}]	2650
$\Delta\rho$ [kg m^{-3}]	1426
μ [kg (ms)$^{-1}$]	0.0151
x_{50} [m]	34.32×10^{-6}
Q [m^{3}h^{-1}]	6.12
v_{in} [m s^{-1}]	5.768
D [m]	0.04
Stk	8.911×10^{-4}

The Stokes number calculations from Equation (2.19):

$$Stk = \frac{1426 \times (34.32 \times 10^{-6})^2 \times 5.768}{18 \times 0.0151 \times 0.04} = 8.911 \times 10^{-4}$$

For the calculations of the cutsize for the hydrocyclone in this thesis the Stokes number calculated from experimental data in [15], Table 7.2, was used. The cutsize for experiments 8 and 11 could then be calculated from $Stk = 8.911 \times 10^{-4}$. The density of the particle in water was calculated in the group from settling in water. The calculations gave varying densities from 1068 to 1120 kg m^{-3}. The cutsize for experiment 11 was calculated using the highest and lowest measured density value.
Example of cutsize calculation of experiment 11 with density of 1120 kg m^{-3}:

$$8.911 \times 10^{-4} = \frac{120 \times {x_{50}}^2 \times 3.38}{18 \times 0.015 \times 0.04}$$

$$x^2 = 2.3727 \times 10^{-8}$$

$$x = 154.0 \times 10^{-6} = 154\mu\text{m}$$

Table 7.3: Experimental data for experiment 8 and 11 needed for calculation of the cutsize.

Property	ρ [kg m^{-3}]	ρp [kg m^{-3}]	$\Delta\rho$ [kg m^{-3}]	μ [kg (ms)$^{-1}$]	v_{in} [m s^{-1}]	D [m]
Experiment 8	1000	1120	120	0.020	2.79	0.04
Experiment 11	1000	1068	68	0.015	3.38	0.04
Experiment 11	1000	1120	120	0.015	3.38	0.04

Table 7.4: Calculation of the cutsize for Experiment 8 and Experiment 11

	ρ [kg m^{-3}]	Stk	x_{50} [µm]
Experiment 8	1120	8.911×10^{-4}	196
Experiment 11	1120	8.911×10^{-4}	154
Experiment 11	1068	8.911×10^{-4}	205

The cutsize for experiment 11 was 205 µm for the lowest density measured and 154 µm for the highest measured density, Table 7.4. The size of the Amberlyst A21 Hydroxide Form particle is measured to be 430 $\pm$ 56 µm. Hence the particle size is in the neighbourhood of the cutsize which may be the reason why the particle exits through the overflow. According to the grade-efficiency curve Figure 2.13, some of the particles will exit through the overflow. As the particle size increases the percentage of particles that exits through the overflow increases.

There are many uncertainties connected to the cutsize calculation, especially in the particle density calculation. The particle is porous which means the pores will be filled when the particle is suppressed in water. The density of the particle in water have been measured in the group by settling of particles in water. The diameter of the particle injected was not measured. Since there are great uncertainties in the density it gives reason to believe that the particle in experiment 11 was in the neighbourhood of the cutsize and was therefore separated out through the overflow.

The CFD simulation for experiment 11, Figure 7.7, also shows that the particle exits through the overflow. In the simulation a density of 1070 kg m^{-3} was used which gives a calculated cutsize of 201 µm. The cutsize in the simulation was also in the neighbourhood of the cutsize, and hence the particle exits through the overflow.

Particle behaviour similar to experiment 11 is also observed in experiment 8, Figure A.8. The experiment had a higher viscosity (20 cP) which gives reason to believe that the particle in this experiment also was in the neighbourhood of the cutsize. Cutsize calculations for experiment 8 with the highest density (1120 kg m^{-3}) shows that the cutsize of 196 µm lies between the two cutsizes for experiment 11, Table 7.4. This gives reason to believe that the particle in this experiment also was close to the cutsize.

Experiment 7, Figure A.7, was, however, executed with the same conditions as experiment 8, Table 5.2, but the particle did not exit through the overflow. Since the size of particle is in the neighbourhood of the cutsize some of the particles will exit through the underflow and some through the overflow. There can also be large variations in particle size of the injected particles. The particle injected in experiment 8 might be small, and

hence closer to the cutsize, while the particle injected in experiment 7 might be large. This is just assumptions since the particle size was not measured.

7.1.3 Effect of Underflow

(a)

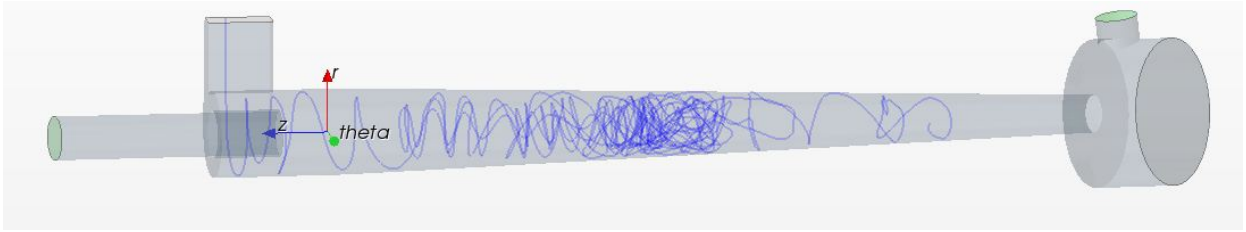

(b)

Figure 7.9: The trajectory in a) is from the experimental result of experiment 17 with 0% underflow and a volume flow rate of 2.0 m^3h^{-1}, Presented in Cartesian coordinates. The trajectory in b) is obtained from the CFD simulation of experiment 17. The end of vortex is present in both trajectories

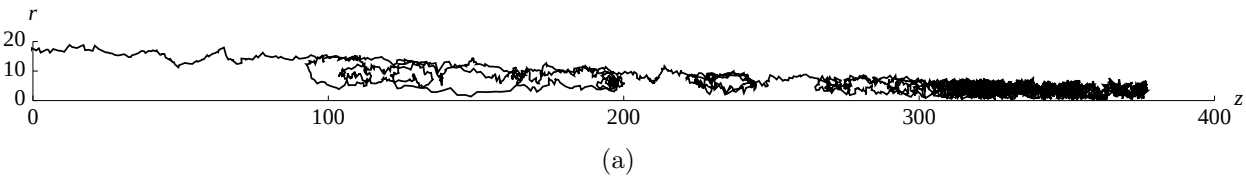

(a)

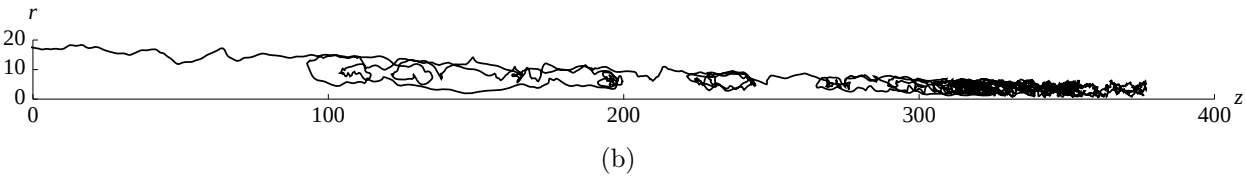

(b)

Figure 7.10: The trajectory in a) is the 2D-trajectory of experiment 17 and the trajectory in b) has been smoothed by Gaussian filter. Both trajectories are presented in a cylindrical coordinate system. The end of vortex phenomenon is present in the lower part of the conical section of the hydrocyclone

End of vortex is a phenomenon that appears when the hydrocyclone is operated under certain conditions. The EoV can be observed as the particle circulate up and down at almost the same spot. The phenomenon is observed in several of the experiment in this

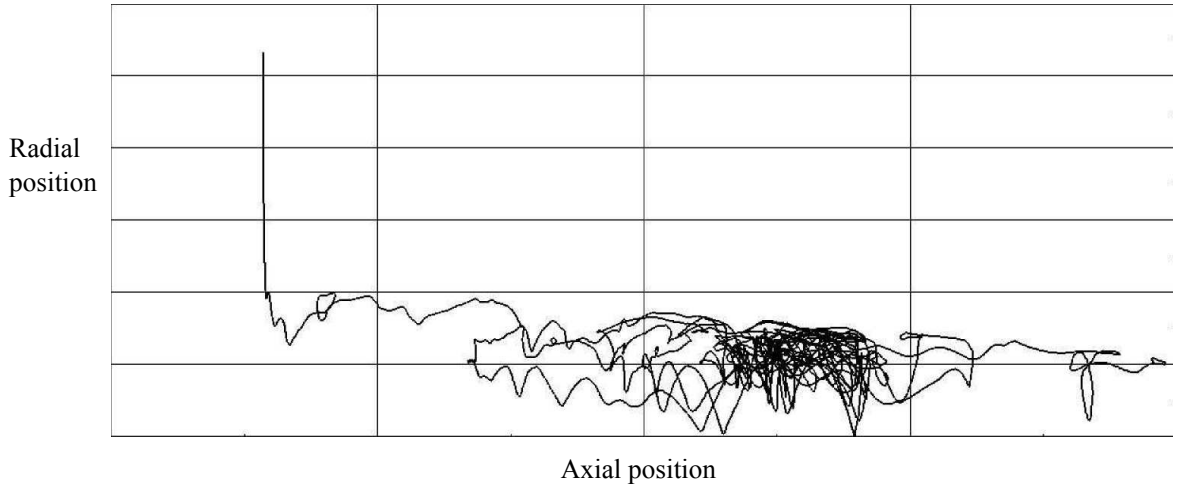

Figure 7.11: 2D-trajectory from CFD simulation for experiment 17 presented in cylindrical coordinates

thesis, i.e. experiments 17, 18, 19 and 22. All of the experiments where the EoV is present was operated under similar conditions, i.e. no underflow, and with the same fluid, Table 5.2.

The phenomenon is also present in the CFD simulation of experiment 17 although the inner core attach to the wall higher in the conical section than in the experimental particle track. The low pressure core in the pressure profile, obtained form the simulation, bend and attach to the wall, Figure 7.12.

The experiments where the EoV was present were all operated with an underflow of 0% and water as fluid. The flow rate varied which indicates that the flow rate in the hydrocyclone had zero, or marginal, influence on the existence of EoV.

Analyses of all the experiments showed that the EoV was not present in any of the experiments with increased viscosity, Appendix A.

Differences in Numerical and Experimental Results

In some of the experiments the numerical results differ from the experimental. Low in the cyclone in experiment 21 and 25, after the flow abnormality, the swirling vortex flow is stronger in the experimental results than in the CFD results. This can be seen in Figures 7.13 and 7.16. A reason for this might be that the EoV is present in the CFD simulation but not in the experimental result and that the weak vortex comes from a secondary induced vortex. The pressure profiles form the CFD simulations show that the low pressure core in the cyclone might bend slightly to the wall in simulation of experiment 21, Figure 7.14 a). This is not the case in the simulation of experiment 25, Figure 7.18. The simulation of experiment 21 was therefore run for a second time with the same settings but with a longer physical time, Table 6.2. The pressure profile then showed that the core did not bend to the wall, Figure 7.14 b).

Experiment 21 was performed with an underflow of 10% of the feed flow rate. The underflow opening might have some influence on the flow pattern in the simulations of the hydrocyclone. The simulation of this experiment does not coincide with the experi-

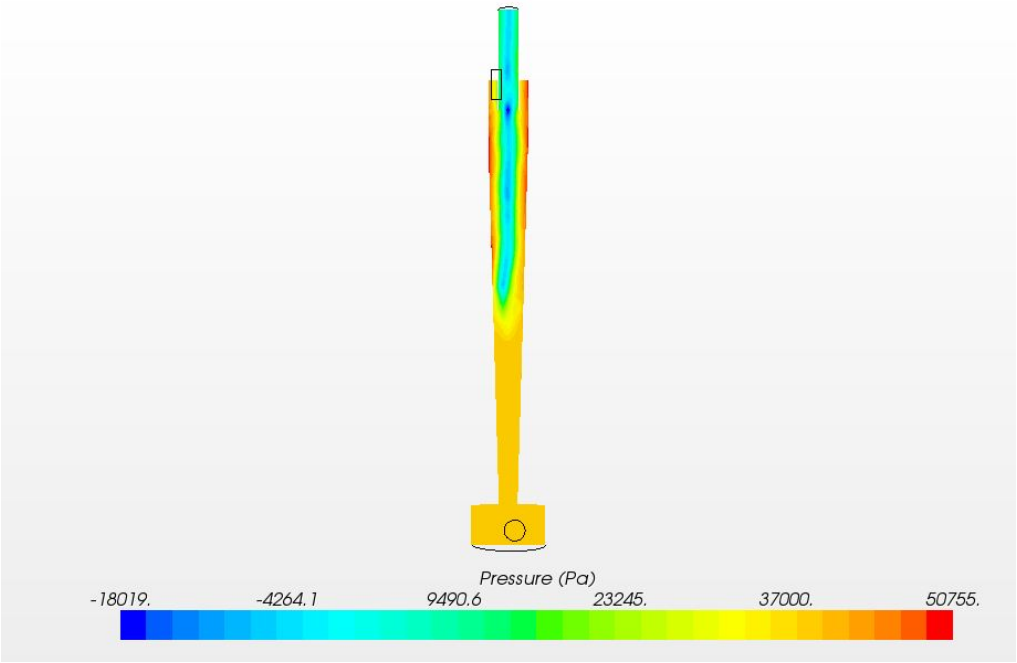

Figure 7.12: Pressure profile from the CFD simulation of experiment 17. The low pressure core in the hydrocyclone bends to the wall of the hydrocyclone which is an indication that the end of vortex is present

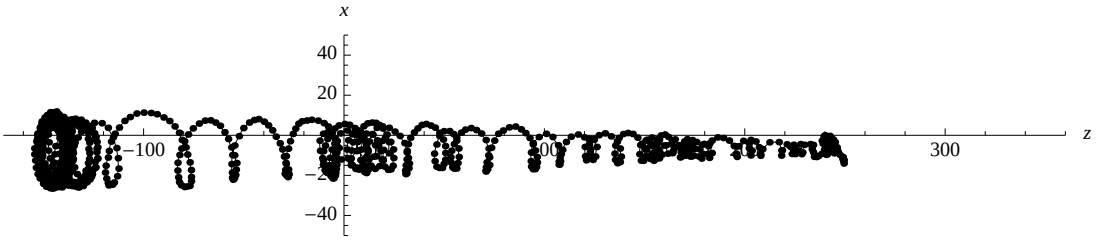

(a)

(b)

Figure 7.13: The trajectory in a) is from the experimental result of experiment 21 with 10% underflow and a volume flow rate of 3.0 m^3h^{-1}, presented in a Cartesian coordinate system. The trajectory in b) is obtained from the CFD simulation of experiment 21

mental results if the EoV is present in the simulation.

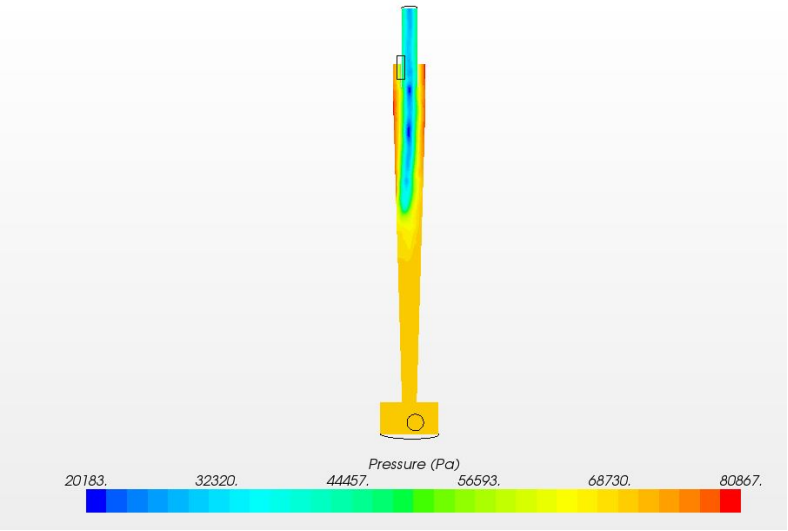

(a)

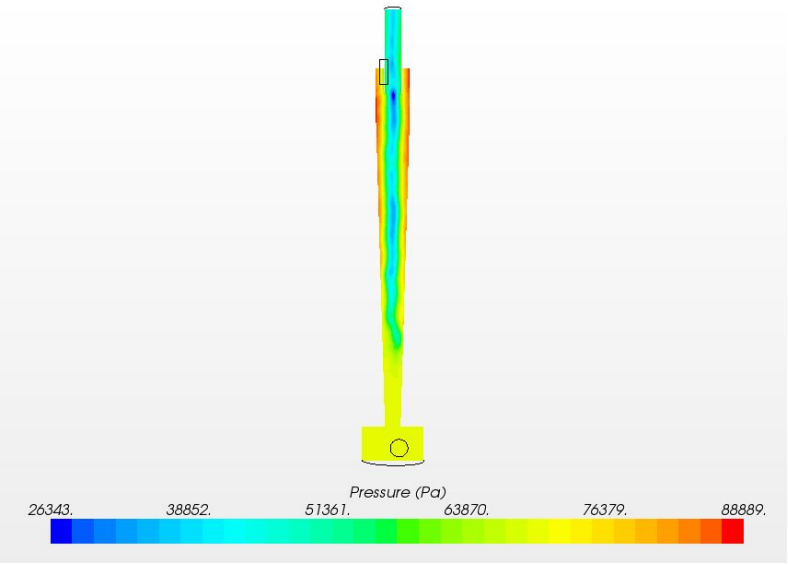

(b)

Figure 7.14: Pressure profile from the CFD simulation of experiment 21. In a) It can be seen that the low pressure core in the hydrocyclone bends slightly to the wall of the hydrocyclone which is an indication that the end of vortex is present. The simulation was run for 2 seconds. The simulation in b) has been run for 5 seconds, the low pressure core do not bend to the wall

In experiment 25, Figure 7.16, the flow abnormality is small and almost non existent in both the experimental and simulated trajectories. Experiment 25 have a slightly higher viscosity due to some glycerol mixed into the water, which may affect the particle track. The experiment is also performed with a large underflow which also influence the particle trajectory. The particle trajectory is, however, fluctuating considerably more than in the other experiments presented in this section. The fluctuations in the trajectory might be due to increased turbulence intensity. The turbulence might be increased by the larger flow through the underflow or by the increased feed flow rate,

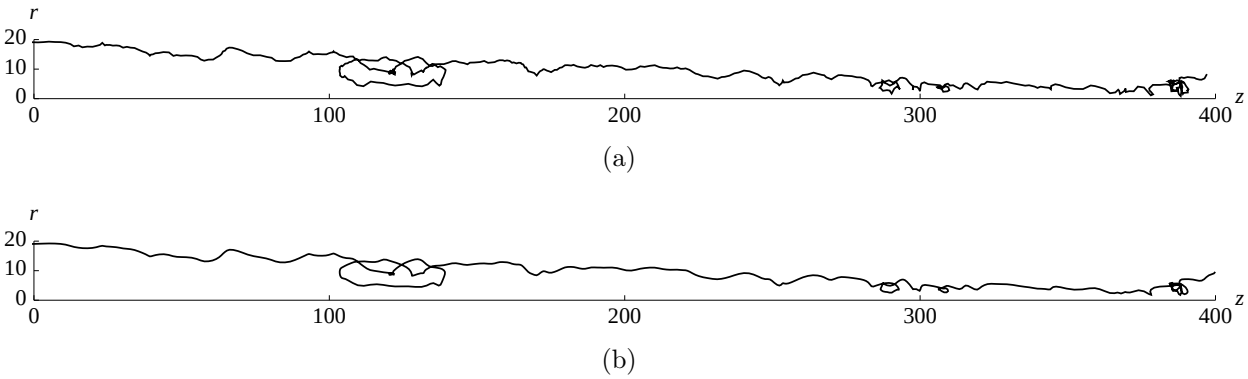

(a)

(b)

Figure 7.15: The trajectory in a) is the 2D-trajectory of experiment 21 and the trajectory in b) has been smoothed by Gaussian filter. Both trajectories are presented in a cylindrical coordinate system

which is not likely since there are other experiments operated with higher feed flow rate where this effect is absent.

The large underflow in experiment 25 might be the reason for the weak vortex in the lower part of the hydrocyclone in the simulation. The simulation of this experiment does not has good correlation with the experimental result even though the EoV is not present in the simulation.

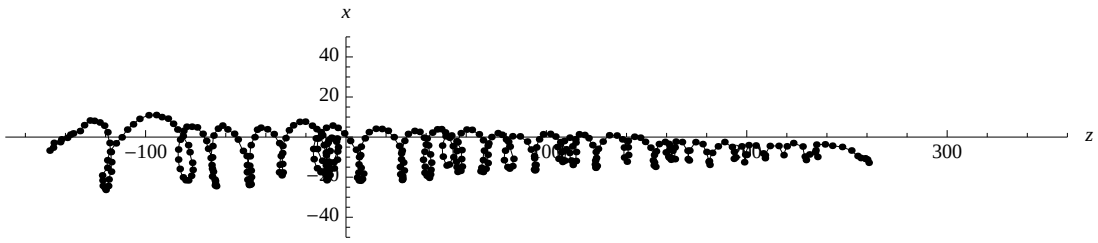

(a)

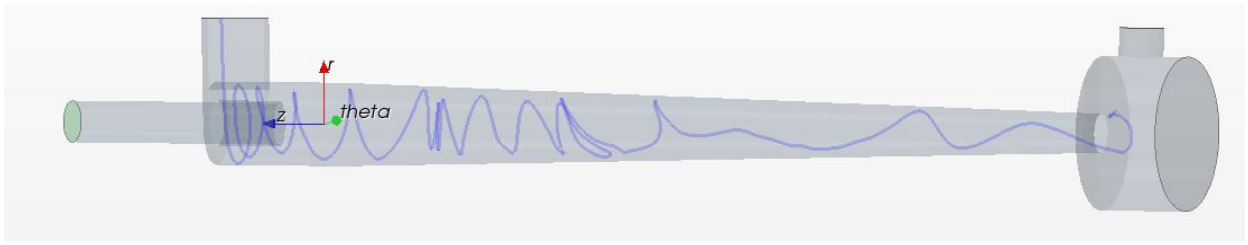

(b)

Figure 7.16: The trajectory in a) is from the experimental result of experiment 25 with 22% underflow and a volume flow rate of 3.2 m^3h^{-1}, presented in a Cartesian coordinate system. The trajectory in b) is obtained from the CFD simulation of experiment 25

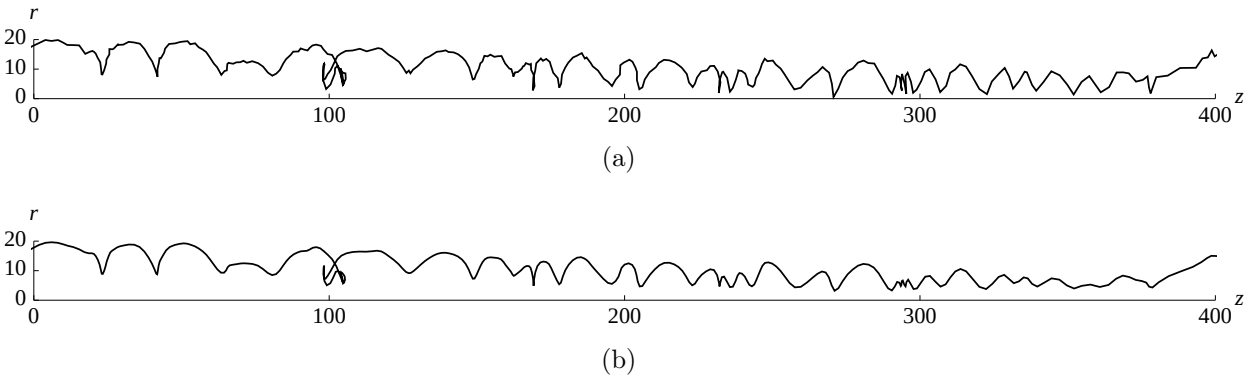

Figure 7.17: The trajectory in a) is the 2D-trajectory of experiment 25 and the trajectory in b) has been smoothed by Gaussian filter.Both trajectories are presented in a cylindrical coordinate system

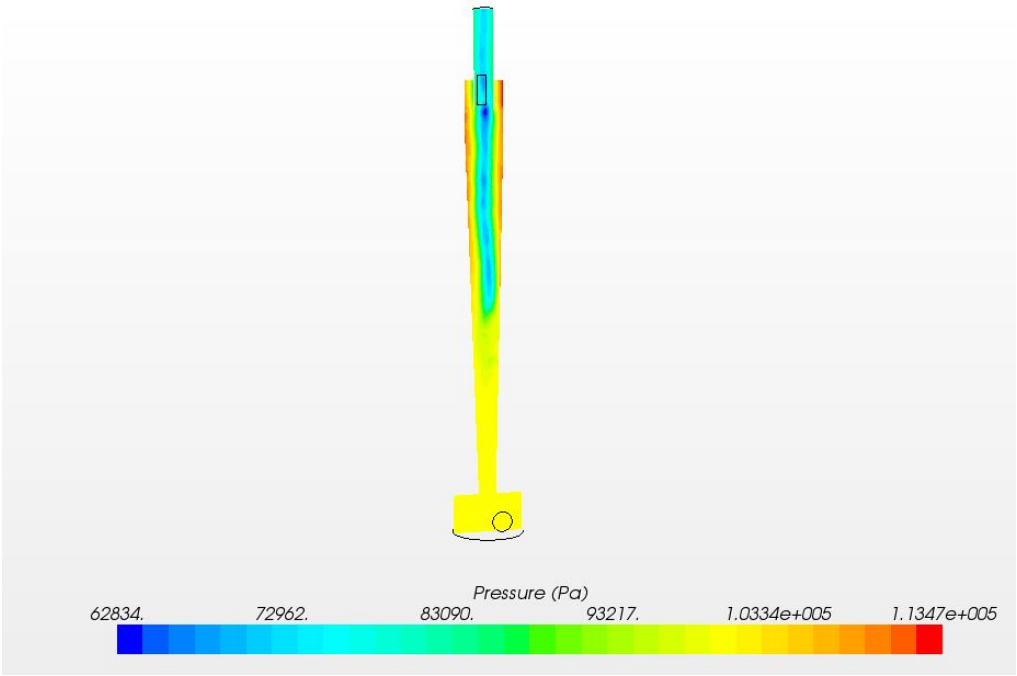

Figure 7.18: Pressure profile from the CFD simulation of experiment 25. It can be seen that the low pressure core in the hydrocyclone does not bent to the wall which indicates that the EoV is not present in the simulation

7.2 Residence Time

A selection of the residence times of the particles in the hydrocyclone are presented in Figures 7.19, 7.20 and 7.21. Every time the particle occurred in a specific area of the cyclone it was counted. The results were illustrated by a histogram.

In the histogram for experiment 17, Figure 7.20, the particle stays in the lower part of the conical section for a long time which supports the statement that the end of vortex is present. The flow abnormality observed in almost all the particle tracks can also be

observed in the histograms.

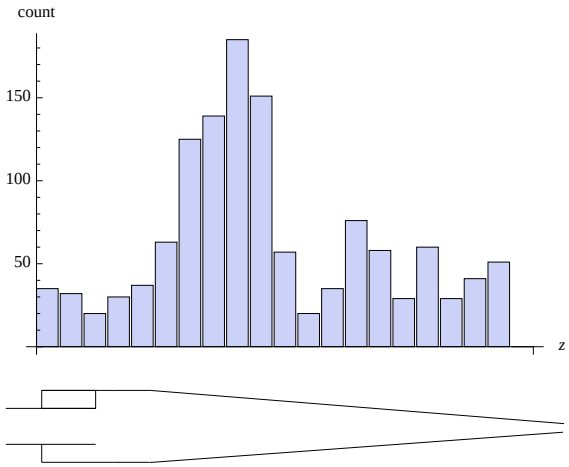

Figure 7.19: Histogram of the particle residence time in different sections of the hydrocyclone in experiment 9

The particle injected in experiment 9, Figure 7.19, occurs more frequently in the part where the flow abnormality appears compared to the particle injected in experiment 21, Figure 7.21. The difference can be due to viscosity differences which is previously discussed.

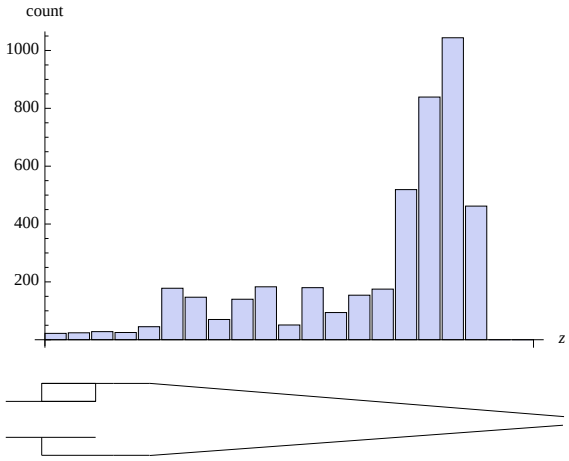

Figure 7.20: Histogram of the particle residence time in the different sections of the hydrocyclone in experiment 17. The end of vortex is present which can be seen as the particle spends a long time in the lower part of the conical section before it exits through the underflow

The residence time is interesting because it is important for the separation efficiency. In experiment 21, Figure 7.21, the particle spends longer time at the end of the cylindrical part of the hydrocyclone. A reason for this might be the flow abnormality which appear where the geometrical shape shifts from cylindrical to conical. The particle also stays longer in the lower part of the conical section which can be a sign that the EoV might

be present. When considering the particle trajectory for experiment 21, Figure 7.10, the EoV is, however, not present.

The EoV phenomenon can in some of the experiments be observed. The flow abnormality can, as mentioned, be seen low in the conical section in experiment 17, Figures 7.9 and 7.10. The particle moves up and down in this part of the hycdrocyclone several times before entering the underflow, and as seen in Figure 7.20 the particle spends a long time in the lower part of the conical section.

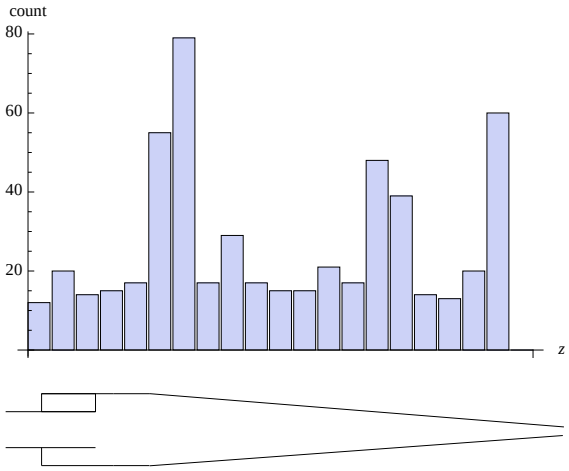

Figure 7.21: Histogram of the particle residence time in the different sections of the hydrocyclone in experiment 21

The flow abnormalities observed in the experiments performed in this thesis prolong the residence time of the particle. When dealing with heavy particle load in the feed, longer residence time might cause problems such as clogging of the hydrocyclone which can lead to reduced capacity and reliability. The presence of the end of vortex in the hydrocyclone is also harmful for the equipment. The EoV attaches itself to the inner wall and turns at the same place at the wall causing depositions or erosion on the inner wall. Depositions can lead to clogging of the hydrocyclone and erosion can decrease the lifetime of the hydrocyclone.

7.3 Neutral Density Particle

A neutral density particle was made by making the fluid density equal to the particle density. This was done by making a salt water solution with 16 weight% NaCl dissolved in water.

In both experiments with a neutral density particle, Figures 7.22 and 7.24, the particles follow the fluid out through the overflow in the hydrocyclone. In experiment 15 the particle circulates in the same area in the hydrocycone before it follows the inner vortex out through the overflow. In experiment 16 the particle follows the outer vortex further into the hydrocyclone before it moves inwards to the inner vortex. In the 2D-trajectories for these two experiments the flow abnormality can be observed, Figures 7.23 and 7.25. Both experiments are operated with the same settings, but different underflows. Experiment 15 and 16 are operated with an underflow of 10% and 5% of

the flow rate, respectively. The difference in the underflow might be the reason for the particle in experiment 16 to move further into the hydrocyclone.

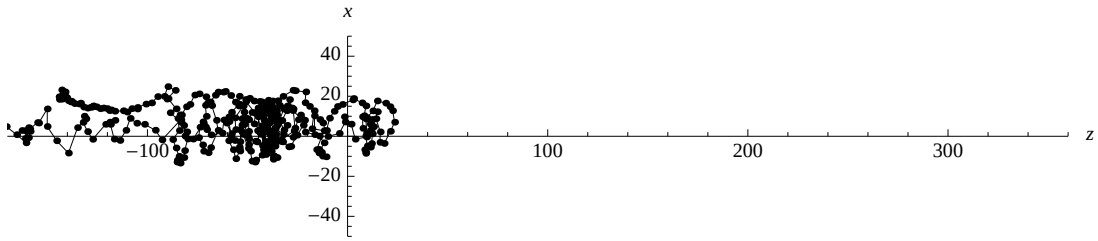

Figure 7.22: Neutral density particle trajectory in a salt solution from experiment 15 with 5% underflow and a volume flow rate of 3.4 m^3h^{-1}, presented in a Cartesian coordinate system

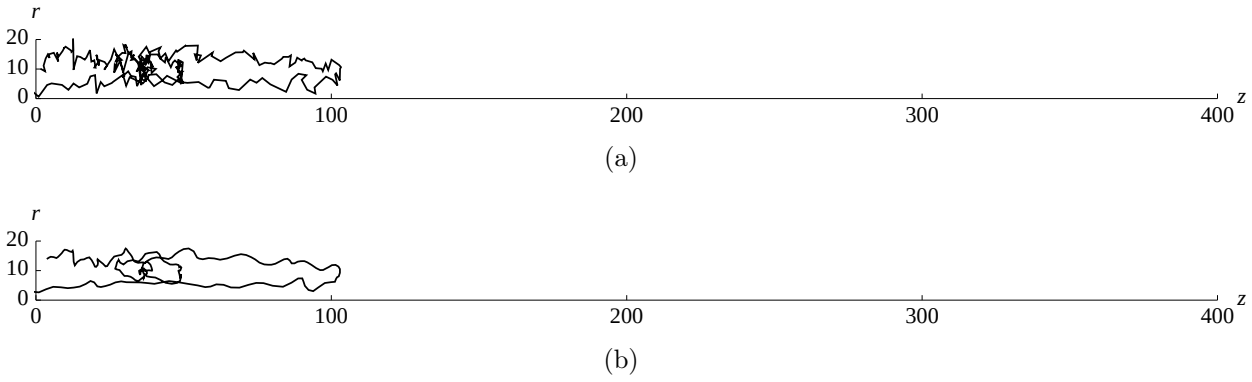

Figure 7.23: The trajectory in a) is the 2D-trajectory of the natural density particle in experiment 15 and the trajectory in b) has been smoothed by Gaussian filter.Both trajectories are presented in a cylindrical coordinate system. The particle exits through the overflow

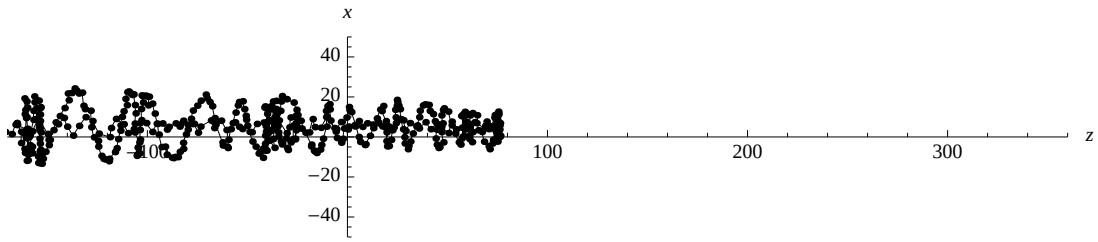

Figure 7.24: Neutral density particle trajectory in a salt solution from experiment 16 with 10% underflow and a volume flow rate of 3.4 m^3h^{-1}, presented in Cartesian coordinates

A neutral density particle should follow the fluid in the hydrocyclone, which means that the particle should exit through the overflow. The particle in both Figures 7.22

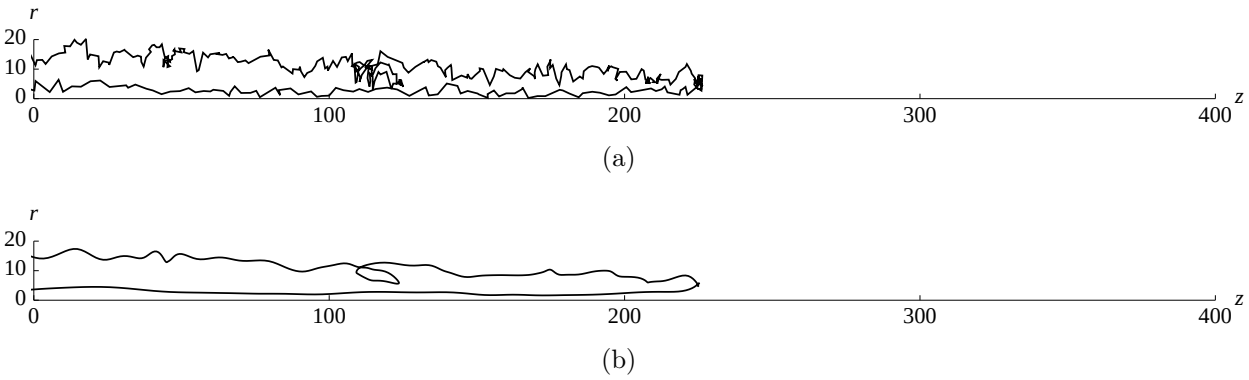

Figure 7.25: The trajectory in a) is the 2D-trajectory of the natural density particle in experiment 16 and the trajectory in b) has been smoothed by Gaussian filter. Both trajectories are presented in a polar coordinate system. The particle exits through the overflow

and 7.24 follows the outer vortex some distance downwards in the hydrocyclone before it travels into the inner vortex and exits out through the overflow. Hence, the neutral density particle moves as expected.

There were, however, only executed two experiments with neutral density particles which had good enough results to obtain particle trajectories. That are not enough replicates to claim that a neutral density particle will exit through the overflow in all cases. There is, however, a tendency that the neutral density particle will exit through the overflow.

There were executed several experiments with neutral density particles to study whether the particle behaves as in theory or not, but the activity on the particle was too low to obtain a sufficient particle trajectory. The reason for the low activity could be that the activity had leaked out into the fluid. When using the salt water solution as fluid it was experienced that the activity leaked out into the solution more quickly than with water. The activity of the particle was not measured at the radiology department at the hospital and it was therefore difficult to determine if the experiments was good or bad before analysing them. Hence only two experiments had enough activity to be detected properly.

7.4 Flow Pattern

The axial and tangential velocity profiles was investigated to see whether or not the velocity profiles coincided with the theory. The flow pattern models, Rankine and Burgers model, for tangential velocity was both investigated.

The axial and tangential velocities for the particle were plotted as a function of the radial position in the hydrocyclone. To visualise the velocity profiles from the experimental points in the figures, a polynomial was fitted to each of the two velocities, Figures 7.26 and 7.27. For the axial velocity the polynomial Equation (7.1) was used to fit the points and Equation (7.2) was fitted to the tangential velocity profile. The polynomials were chosen because they appeared to be a good fit for the theoretical velocity models.

$$v_z = a + bx + cx^2 + dx^3 \tag{7.1}$$

$$v_\theta = ax + bx^2 + cx^3 + dx^4 \tag{7.2}$$

The axial velocity results for experiment 9, Figure 7.26, shows that the polynomial, Equation (7.1), fitted to the experimental points is a good fit. A resemblance to the theoretical sketch, Figure 2.9, was also observed for the axial velocity profiles for all the experiments.

The point where the axial velocity profile crosses the horizontal axis represents the fluid crossing over from inner vortex to outer vortex. In Figure 2.9 it crosses over approximately 8 mm from the hydrocyclone axis. The CS can be assumed to be the non-existing axis between the inner and outer vortex. Hence the polynomial is a good fit for the axial velocity as the curve crosses the horizontal axis close to the CS.

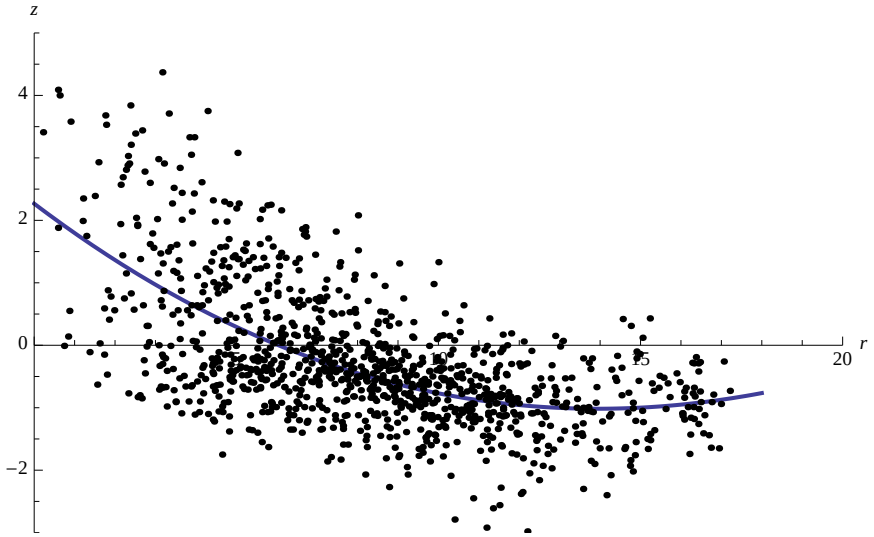

Figure 7.26: Polynomial equation (7.1) fitted to axial velocity values from experiment 9

In Figure 7.27 a polynomial, Equation (7.2), has been fitted to the tangential velocity profile. For the tangential velocity profile there is some resemblance to both Rankine model and Burgers model, Figure 2.5, discussed in Section 2.3.

As can be seen in Figure 2.4 the tangential velocity profile for an ideal flow has a peak at the beginning of the profile before descending. In Figure 7.27 the tangential velocity profile for the experiment has one peak then descends before it reaches a lower peak. The reason for a weaker curve for the experimental data than the theory might be that the hydrocyclone used for the experiments has a long cone. If the tangential velocity is measured by considering a fluid element in the hydrocyclone, the fluid element has an area of friction at the top and at the bottom. The friction area at the wall, the bottom of the fluid element, will be larger with a long cone than with a shorter more angled conical section.

It is a trend throughout all the experiments that the tangential velocity profile curve is lower than the theoretical Rankine model. The curve have more resemblances to the

Burger model and the model is therefore used for further investigations of the tangential velocity profile.

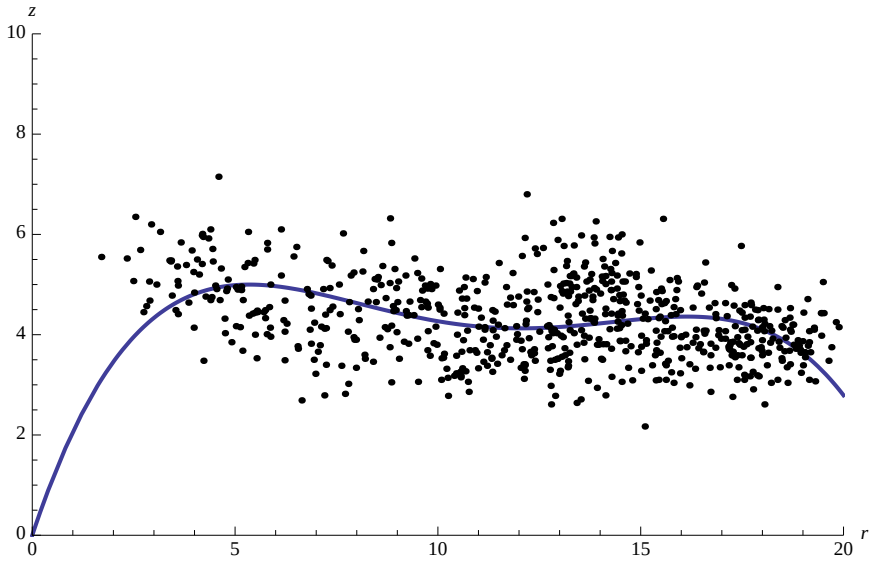

Figure 7.27: Polynomial equation (7.2) fitted to tangential velocity values from experiment 21

The Burgers equation (2.9) defines the equation for tangential velocity for the Burgers vortex. The parameters c and re are found by a programming code, developed in the group. The code fits Equation (2.9) to the experimental results, Figure 7.28. The parameters found by this method is presented in table 7.5.

From Equation (2.8) the Γ can be calculated from the inlet velocity, v_{in}, and the radius, r, of the cyclone. According to Equation (2.8) can the Γ be compared to the parameter c. The calculated circulation values are presented in Table 7.5.

The experimental data is fitted to the Burger equation (2.9) and the circulation Γ is calculated from Equation (2.8) for all the experiments in Table 7.5. The values of the parameter c and the circulation Γ should in theory be the same. The table shows, however, that the values differs and the difference is not consistent throughout the table. The tendency is that the circulation lies in the same magnitude as the parameter c. It seems that the Burgers equation gives a good model of the flow in the hydrocyclone.

The parameter re is representing the radial position at the highest point in the fitted curve.

Experiment 5 is excluded from the table because the measurements of tangential velocities were fluctuating between high and low values, which is not likely to happen, and can be due to low activity on the particle. The fitted values were therefore unreasonably high.

Table 7.5: Burgers vortex Equation (2.9) fitted to the experimental results and calculated circulation by Equation (2.8) for each experiment.

Experiment	Parameter, c [m^2s^{-1}]	Inlet velocity, v_{in} [m s^{-1}]	Circulation, Γ [m^2s^{-1}]	Parameter, re [m]
1	0.0655	2.90	0.0580	0.00600
2	0.0781	3.16	0.0632	0.00754
3	0.0734	3.05	0.0610	0.00702
4	0.0656	3.60	0.0720	0.00734
6	0.0491	2.95	0.0590	0.00667
7	0.0423	1.89	0.0378	0.00658
8	0.0579	2.79	0.0558	0.00824
9	0.0435	3.60	0.0720	0.00684
10	0.0375	3.49	0.0698	0.00512
11	0.0375	3.38	0.0676	0.00479
12	0.0484	3.75	0.0750	0.00683
13	0.0522	3.90	0.0780	0.00700
14	0.0565	2.95	0.0590	0.00710
15	0.0596	3.66	0.0732	0.00654
16	0.0650	3.61	0.0722	0.00768
17	0.0391	3.22	0.0644	0.00823
18	0.0570	3.05	0.0610	0.00655
19	0.0745	3.52	0.0704	0.00838
20	0.0655	3.42	0.0684	0.00838
21	0.0610	3.15	0.0630	0.00745
22	0.0407	1.48	0.0296	0.00776
23	0.0664	2.11	0.0422	0.00110
24	0.0341	2.09	0.0418	0.00666
25	0.0604	1.85	0.0370	0.00767

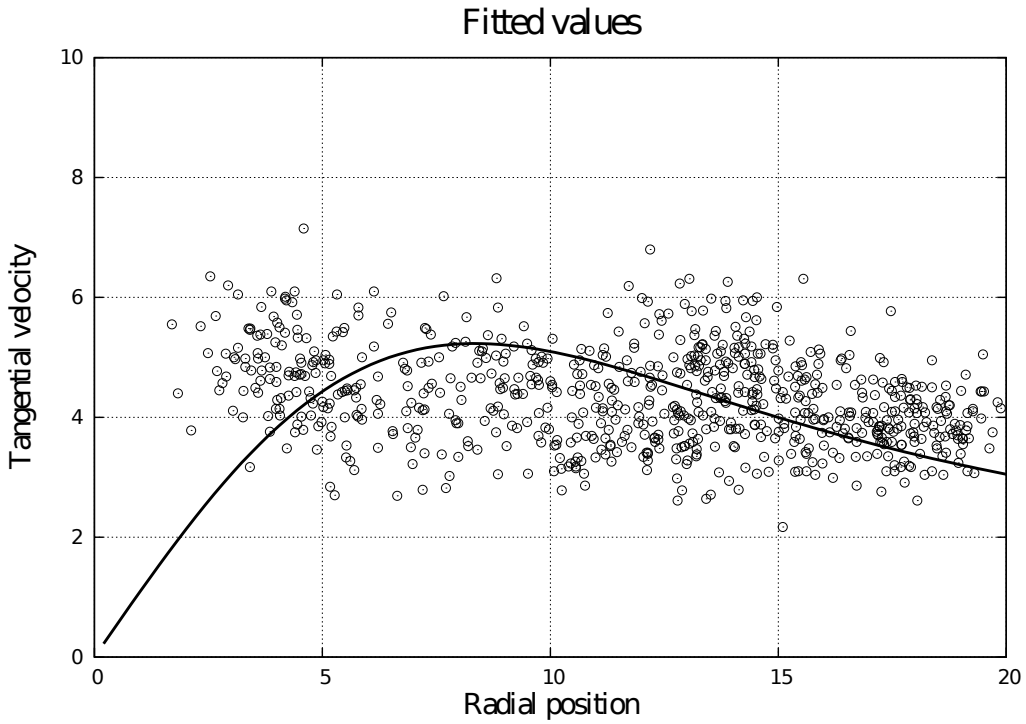

Figure 7.28: Fitted Burgers vortex to experimental values of tangential velocity, experiment 21

7.5 Velocity and Time Profile

How the tangential velocity developed over time was investigated in order to understand how the tangential velocity develop throughout the hydrocyclone. The tangential velocity fluctuate through the whole cyclone and the flow abnormality is visible as an increase in velocity.

Figure 7.29 shows the tangential velocity as a function of time for experiment 3. The first plot is smoothed by a Gaussian filter and the second plot presents the CFD result. There is a good correlation between the CFD simulation and experimental results.

Right after entering the cyclone the inlet velocity drops, Figure 7.29. It then fluctuates over an interval of 6 m s^{-1}. When the particle enters the cyclone it hits the wall several times and looses momentum every time which can explain the huge velocity drop in the inlet. The tangential velocity fluctuates throughout the whole hydrocyclone, Figure 7.29.

There is a good resemblance between the experimental and the numerical plot. If the peaks in each of the plots are counted they have an equal number of peaks before the disturbance in the curve. The disturbance coincides with the flow abnormality. As seen in Figure 7.29 the flow abnormality is also visible in the velocity versus time plot. The velocity in the flow abnormality is higher and the velocity does not fluctuates as much in the abnormality. This is as expected since the velocity in the inner vortex is higher than in the outer vortex.

If the number of peaks is compared to the particle trajectory of experiment 3, Figure 7.2, they may represent the circles the particle follows in the outer vortex so that each

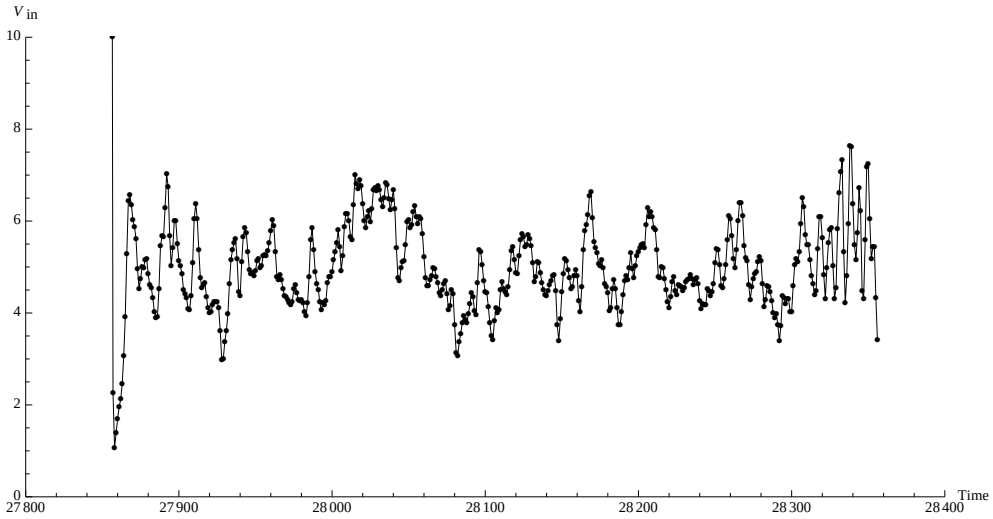

(a)

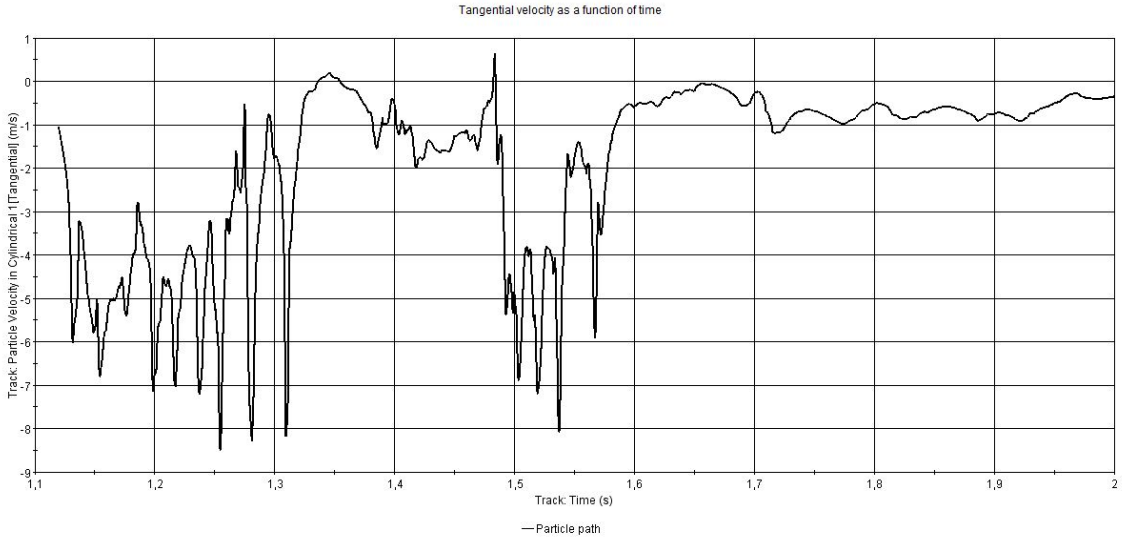

(b)

Figure 7.29: Tangential velocity as a function of time from experiment 3. Tangential velocity in a) is smoothed with Gaussian filter for removal of scattering and b) is obtained from the CFD simulation

peak occurs at a particular angular position. When the flow abnormality occurs the particle has turned seven times at the upper wall both in the experimental and numerical particle trajectory, which is the same number as peaks observed in the Figure 7.29. The velocity fluctuations can be explained by high velocity on one side of the hydrocyclone and low on the other. As the particle turns in the hydrocyclone the tangential velocity will follow these velocity differences, i.e. fluctuate as seen in Figure 7.29.

In Figure 7.30 the plot from Figure 7.29 is combined with the radial position of the particle as a function of time. The fluctuations seen in Figure 7.29 correlates with the fluctuations in the radial position. This is consistent with the statement that there is higher tangential velocity on one side of the hydrocyclone.

Velocity plotted over time from an experiment where the end of vortex is present,

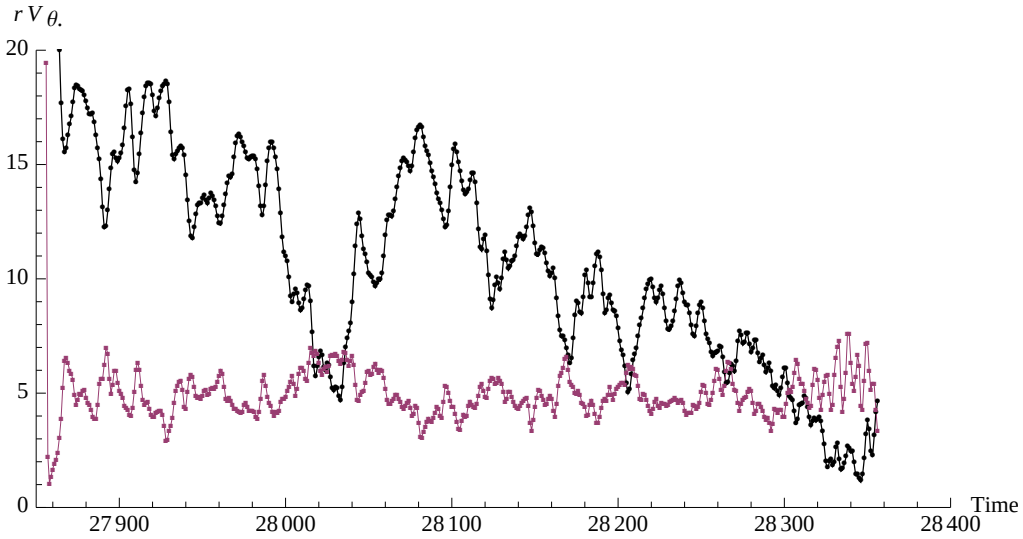

Figure 7.30: Tangential velocity as a function of time combined with the radial position as a function of time. The fluctuations coincide with each other which might be due to higher velocity on one side of the hydrocyclone

experiment 17, is presented in Figure 7.31. The velocity is more stable over time in experiment 17 than in experiment 3, Figure 7.29. Since the particle has a significantly longer residence time through the hydrocyclone due to the end of vortex, there are detected a lot more LOR's in the experiment.

In the CFD simulated velocity and time profile the flow abnormality can be seen as an increase in the velocity. The flow abnormality can also be seen in the experimental profile but less distinct. The velocity in experiment 17 oscillates more frequently after the flow abnormality than in experiments without EoV. The magnitude of the velocity is also lower in experiment 17 both in the experimental and in the numerical results.

When the particle in the bottom of the cyclone moves near the axis of the hydrocyclone the tangential velocity becomes high, which can be seen in the right part of Figure 7.31.

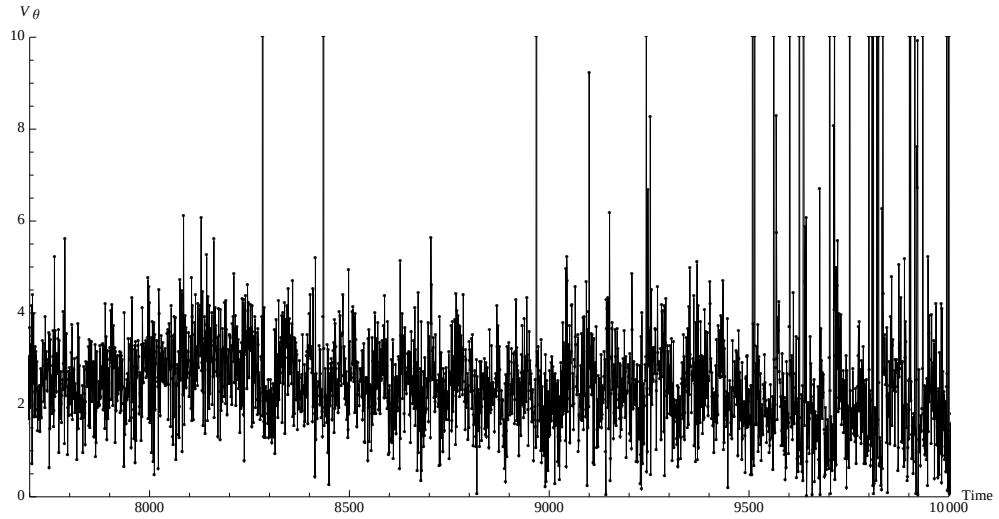

(a)

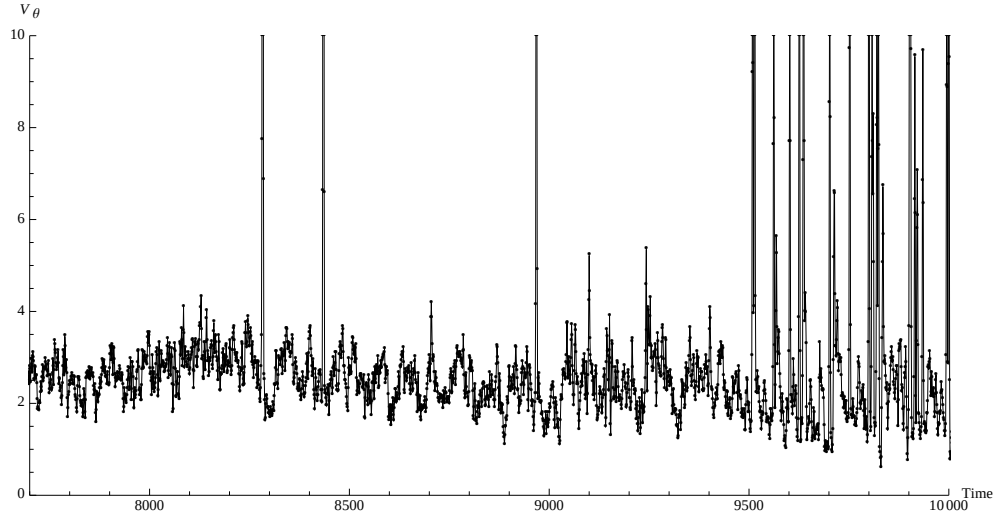

(b)

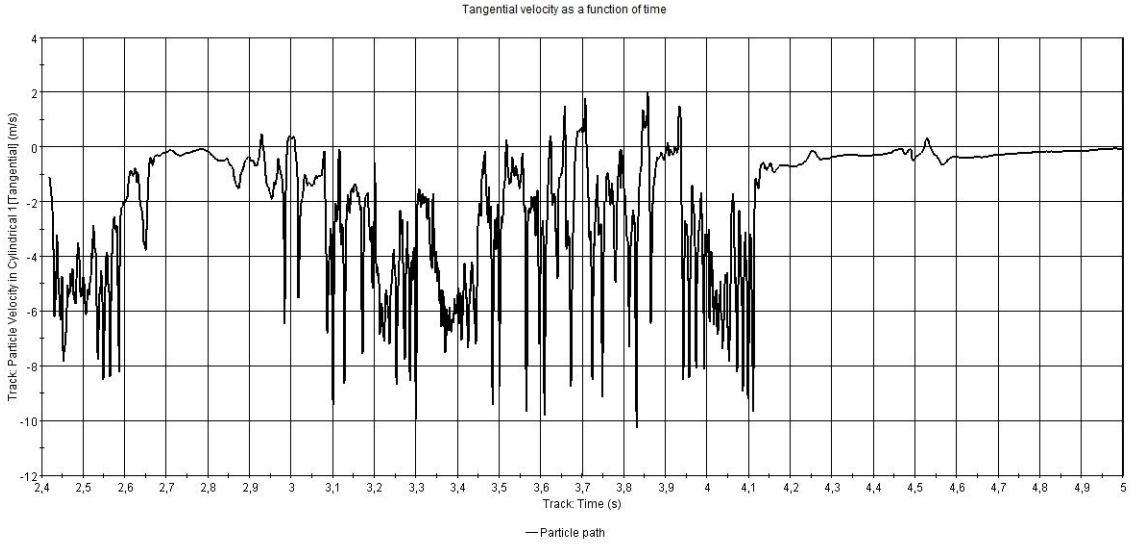

(c)

Figure 7.31: a) Tangential velocity as a function of time from experiment 17, the end of vortex is present, b) is smoothed with Gaussian filter to remove scattering and c) is obtained from the CFD simulation

7.6 Sources of Error

The main sources of error in the experiments and in the comparison to the CFD simulations are listed below.

- Manual adjustments of the valves and the fluctuations in the flow meters, means that there might be uncertainties in the flow rate measurements.
- The alginate solution was slightly temperature dependent and shear thinning which means that the measured viscosities was not accurate.
- Multiple particles going through the field of view at the same time.
- The size of the particle was measured to be 430 $\pm$ 56 µm, a diameter of 500 µm was used for all the simulations.
- There can be deviations between the simulation design and the physical model.
- There can be uncertainties in the particle position in the hydrocyclone due to several effects:

    1. The positron, emitted from ^{18}F, travels a mean distance of 0.6 mm and a maximum distance of 2.4 mm in water before it annihilates with an electron [20].
    2. The direction of the emitted γ-rays might slightly deviate form the distance of 180 ° due to the momentum of the electron and positron before the annihilation.
    3. The LOR's detected can deviate from original annihilation due to Compton scattering. To filter out such events the Siemens TruePoint PET scanner operates with an energy window between 425 and 650 keV. Regardless of this some scattered events with energies higher than the threshold might still be detected.
    4. The spatial resolution of the LOR's are limited by the finite size of the LSO crystal sensors. This means that the precision of the cut-points the particle position is calculated from are restrained.
    5. For a photon to be detected it has to penetrate a distance into the sensor crystal. If the photon is annihilated far from the center of the FOV it will penetrate the crystal at an angle. If the photon penetrates the material of the first sensor crystal and is detected by the neighbouring sensor crystal, a LOR is wrongly drawn between the crystal that detected the photon rather than the crystal it first hit [21].

When an experiment was executed the particle was either collected in the underflow box or gone back to the tank, Figure 5.2. When the particle was collected it was taken out of the hydrocyclone system before the next particle was injected. If it was not collected the new particle was injected while the first was still in the system. This would not be a problem unless two particles were going through the FOV at the same time. The two particles would then disturb each others signals and the detected results would be inconclusive.

The algorithm used in this thesis determines the particle position form a final cut-point window with a radius of 8 mm. Chang et al. [21] measured a single stationary particle in the scanner for 30 seconds. When computing one particle position per millisecond the standard deviation of the particle positions were determined to be below 0.13 mm for both x and y directions. In the z direction it was determined to be below 0.17 mm, Figure 7.32. This confirms the effectiveness of the algorithm and the activity on the tracer particle in this thesis since the same algorithm and labelling technique have been used.

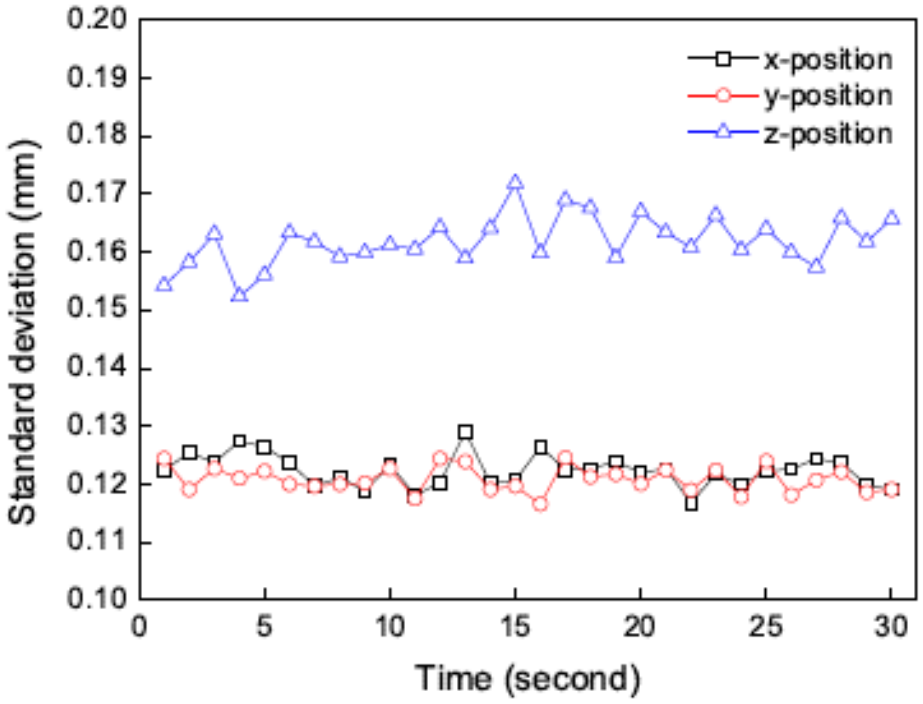

Figure 7.32: Standard deviation for the position of a stationary particle obtained with the algorithm taken from [21]. The standard deviation for the x and y directions are below 0.13 mm and below 0.17 mm in the x direction.

Low activity on the particle can lead to missed signals for the detector which can disturb the particle trajectory and also give rise to a higher standard deviation in the cross triangulated particle position. The experiments executed with salt water solution turned out to give insufficient results and the particle track could not be obtained from most of the experiments. The reason for this could be that the activity leaked out into the fluid and that there was not enough activity left on the particle to detect its position. The activity of the particle could not be tested at the hospital after the particle was injected and therefore the insufficient experiments could not be detected before analysing them. Experiments with too low activity to obtain a proper particle track was, however, discarded.

Chapter 8

Conclusion

The results discovered in this thesis show that following a particle in a hydrocyclone by the PEPT technique gives a detailed view of the particle trajectory. The particle tracks have exposed several flow abnormalities and showed the effect of how high viscosity fluid in the system. The main findings in this thesis is listed below:

- A good correlation between simulated and experimental particle trajectories were found.
- A flow abnormality in the particle trajectory at the geometrical shift from conical to cylindrical sections in the hydrocyclone was discovered in almost every experiment.
- The high viscosity experiments leads to higher residence time in the hydrocyclone due to a larger flow abnormality. The particle appeared lighter in high viscosity experiments which leads to significantly longer flow abnormality and to several more circulations in the flow abnormality.
- The end of vortex did not exist in any of the high viscosity experiments. It was, however, existent in some of the experiments with water both in the experimental and the numerical results.
- Cutsize calculations by Stokesian scaling showed that some of the high viscosity particles was in the neighbourhood of the cutsize for the cyclone, and hence exited through the overflow.
- The Burger vortex model was a good fit for the experimental tangential velocity profiles.
- The tangential velocity profile over time fluctuates throughout the hydrocyclone. The fluctuations coincides with fluctuations in the radial position over time, which give reason to believe that there are variations in the tangential velocity depending on the position in the hydrocyclone.

Chapter 9

Suggestions for Further Work

The particle behaviour in the complex flow in a hydrocyclone has been investigated in this theses, but there are still many undetected aspects of the particle flow.

It would e.g. be interesting to follow multiple particles through a hydrocyclone and see how the particles interact with each other. It would also be interesting to find out why the EoV does not exist in any of the high viscosity experiments.

It would be interesting to study particle trajectories in a cyclone without, or with a very small, cylindrical section to see if the flow abnormality appears at the same place in the cyclone body or if it appear at all.

When the activity on the particle was too low to detect its position it lead to insufficient results. In this thesis the activity of the particle was not measured before the experiments were executed. If this was measured it would be easier to see if the experiments gave good or bad results.

If it was possible to control the activity on the particle better it probably would be easier to carry out the experiments with salt water solution. If the activity on the particles cannot be controlled, another way to modify the density of the fluid that do not change the viscosity significantly should be tested. It would be interesting to see if several replications of the neutral density particle experiments would behave like the ones studied in this thesis.

In this thesis it is seen that the fluctuations in the tangential velocity correlates with the fluctuations in the radial position over time. Further investigations might lead to greater knowledge of the particle flow pattern in the hydrocyclone.

A full CFD analysis of all the experiments would be an interesting investigation. There are several possibilities for CFD simulations of the experimental results in this thesis. Properly simulation of the EoV in a flow containing particles would be interesting. I would also be interesting to investigate the axial and tangential velocity profiles by CFD simulations.

The results form this thesis show that detailed particle tracks can be obtained form a tracer particle followed through a hydrocyclone. It could also be interesting to investigate the particle behaviour by the PEPT technique in other processing equipment.

Appendix A

Results from all the Experiments

Particle path for all the experiments executed in this project. The particle trajectory for experiment 3, 9, 11, 15, 16, 17, 21 and 25 is also presented in Chapter 7, Results and Discussion.

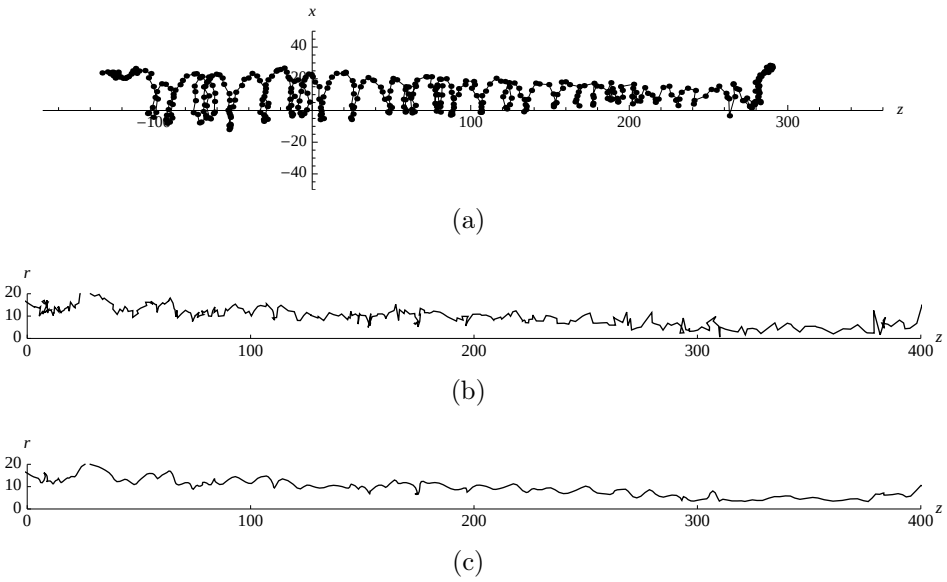

Figure A.1: In a) is the particle trajectory in water from experiment 1 with 10% underflow and a volume flow rate of 3.4 m^3h^{-1}, presented in Cartesian coordinates. In b) is the 2D-trajectory of the particle trajectory in experiment 1 presented and in c) the 2D-trajectory has been smoothed by Gaussian filter. Both b) and c) trajectories are presented in a cylindrical coordinate system

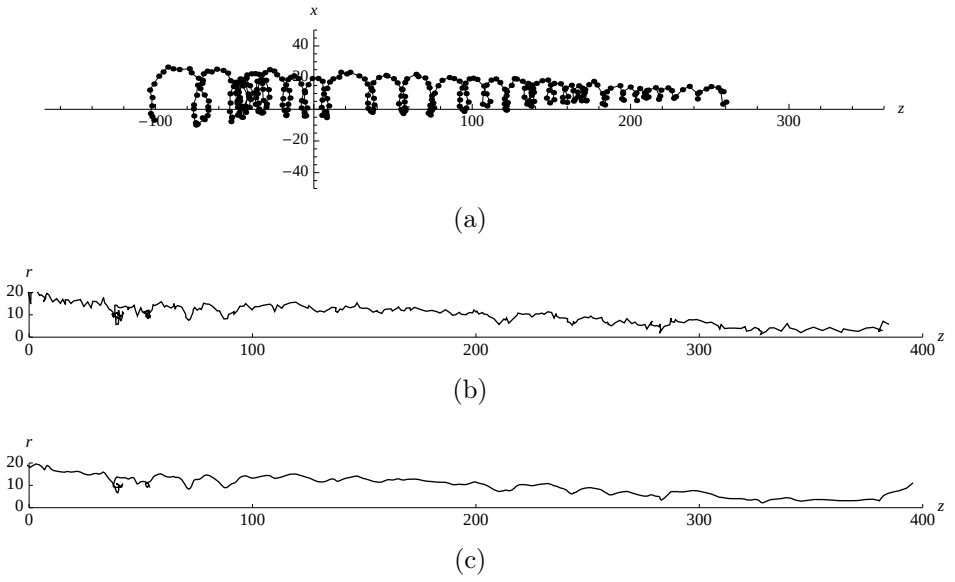

Figure A.2: In a) is the particle trajectory in water from experiment 2 with 10% underflow and a volume flow rate of 3.4 m^3h^{-1}, presented in Cartesian coordinates. In b) is the 2D-trajectory of the particle trajectory in experiment 2 presented and in c) the 2D-trajectory has been smoothed by Gaussian filter. Both b) and c) trajectories are presented in a cylindrical coordinate system

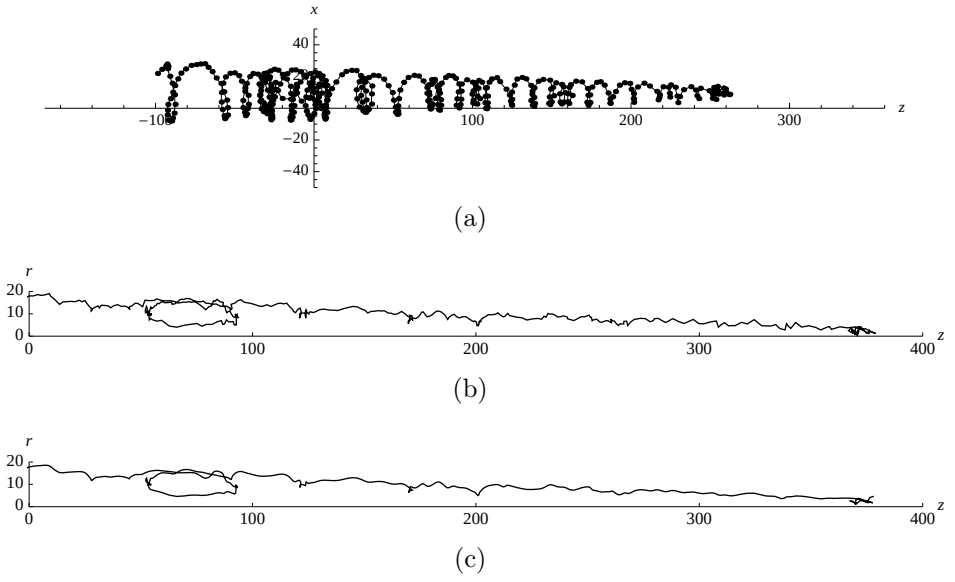

Figure A.3: In a) is the particle trajectory in water from experiment 3 with 10% underflow and a volume flow rate of 3.4 m^3h^{-1}, presented in Cartesian coordinates. In b) is the 2D-trajectory of the particle trajectory in experiment 3 presented and in c) the 2D-trajectory has been smoothed by Gaussian filter. Both b) and c) trajectories are presented in a cylindrical coordinate system

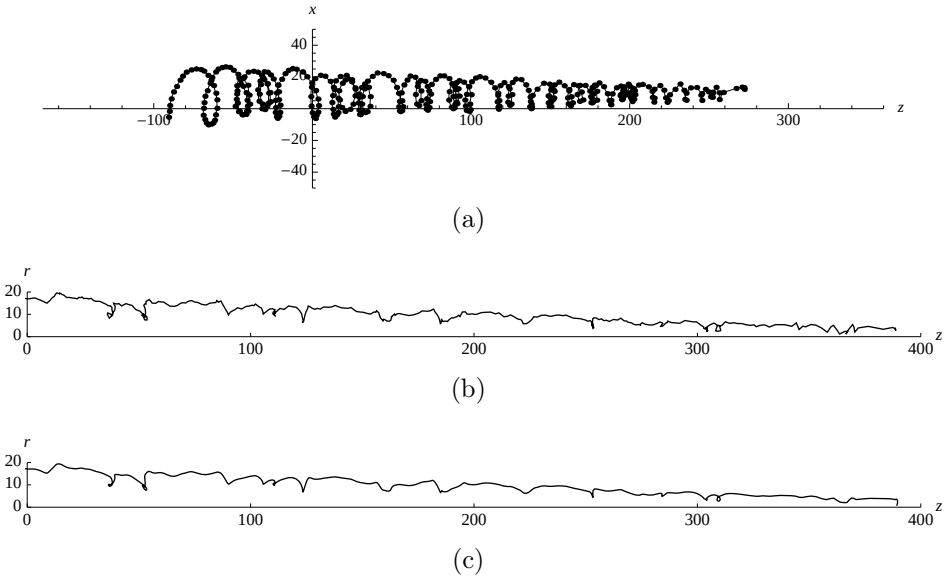

Figure A.4: In a) is the particle trajectory in water from experiment 4 with 5% underflow and a volume flow rate of 3.4 m^3h^{-1}, presented in Cartesian coordinates. In b) is the 2D-trajectory of the particle trajectory in experiment 4 presented and in c) the 2D-trajectory has been smoothed by Gaussian filter. Both b) and c) trajectories are presented in a cylindrical coordinate system

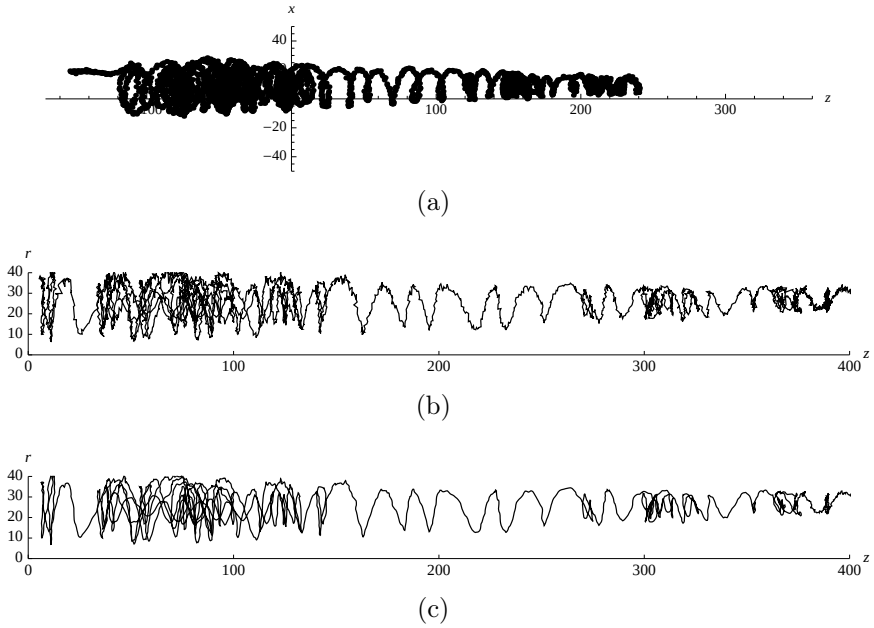

Figure A.5: In a) is the particle trajectory in water from experiment 5 with 0% underflow and a volume flow rate of 1.0 m^3h^{-1}, presented in Cartesian coordinates. In b) is the 2D-trajectory of the particle trajectory in experiment 5 presented and in c) the 2D-trajectory has been smoothed by Gaussian filter. Both b) and c) trajectories are presented in a cylindrical coordinate system

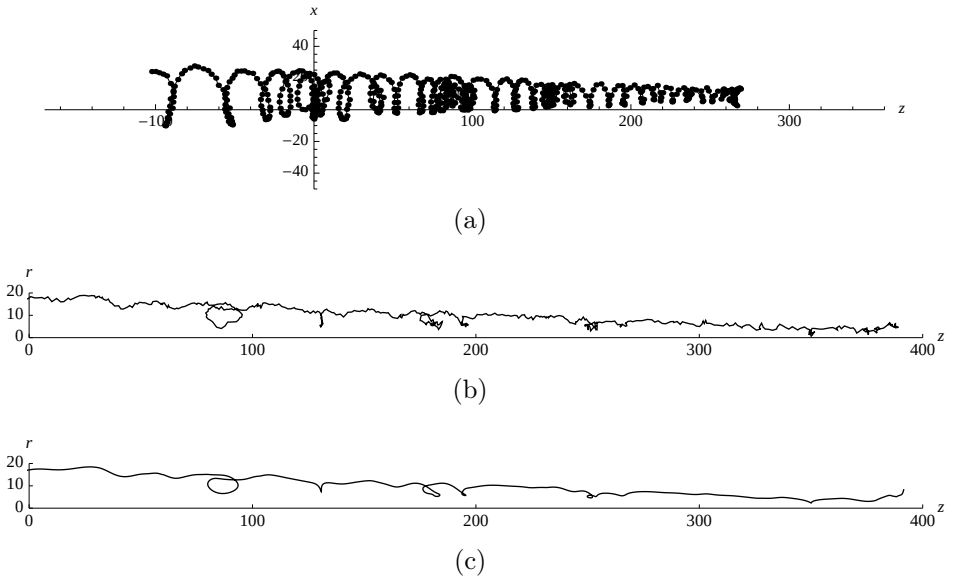

Figure A.6: In a) is the particle trajectory in water from experiment 6 with 5% underflow and a volume flow rate of 2.8 m^3h^{-1}, presented in Cartesian coordinates. In b) is the 2D-trajectory of the particle trajectory in experiment 6 presented and in c) the 2D-trajectory has been smoothed by Gaussian filter. Both b) and c) trajectories are presented in a cylindrical coordinate system

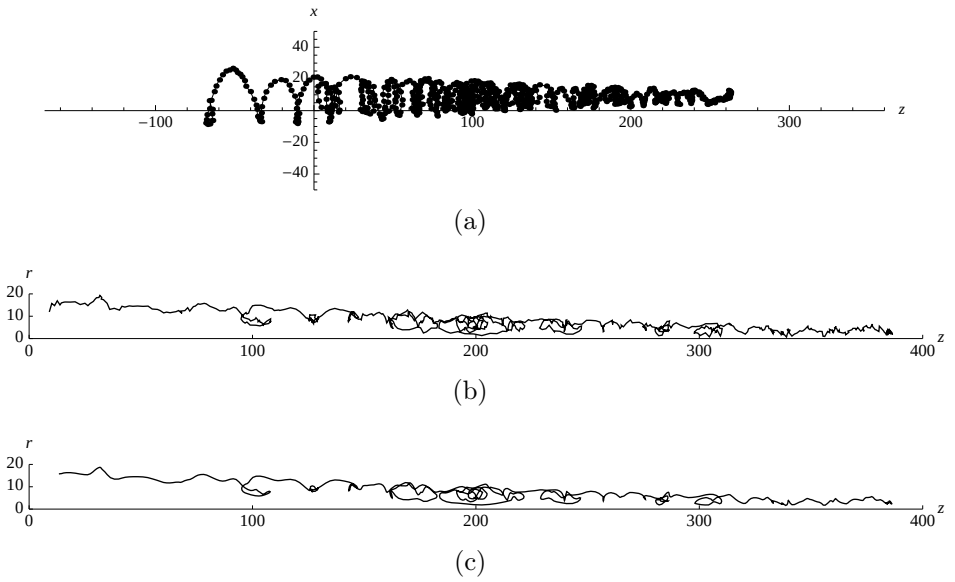

Figure A.7: In a) is the particle trajectory in alginate (20 cP) from experiment 7 with 5% underflow and a volume flow rate of 3.3 m^3h^{-1}, presented in Cartesian coordinates. In b) is the 2D-trajectory of the particle trajectory in experiment 7 presented and in c) the 2D-trajectory has been smoothed by Gaussian filter. Both b) and c) trajectories are presented in a cylindrical coordinate system.

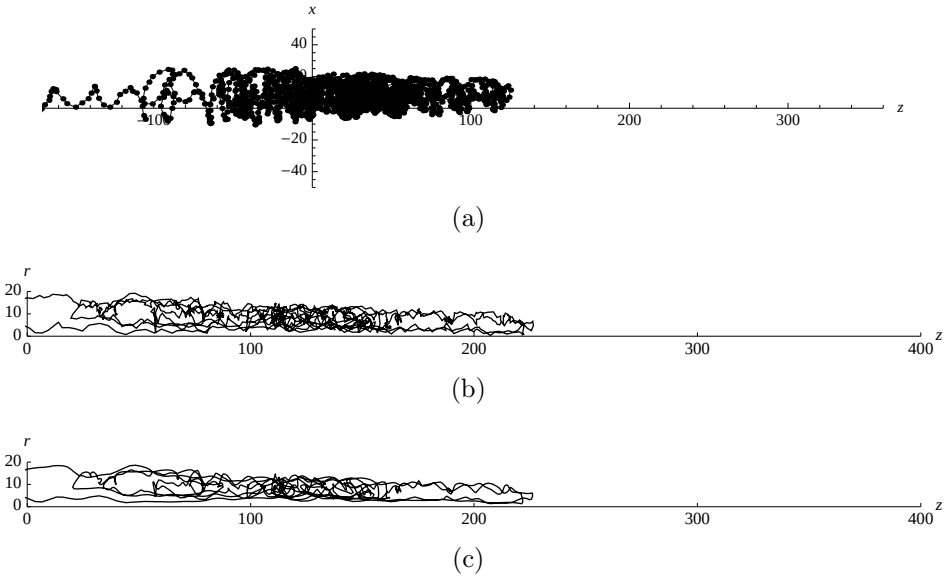

Figure A.8: In a) is the particle trajectory in alginate (20 cP) from experiment 8 with 5% underflow and a volume flow rate of 3.3 m^3h^{-1}, presented in Cartesian coordinates. In b) is the 2D-trajectory of the particle trajectory in experiment 8 presented and in c) the 2D-trajectory has been smoothed by Gaussian filter. Both b) and c) trajectories are presented in a cylindrical coordinate system.

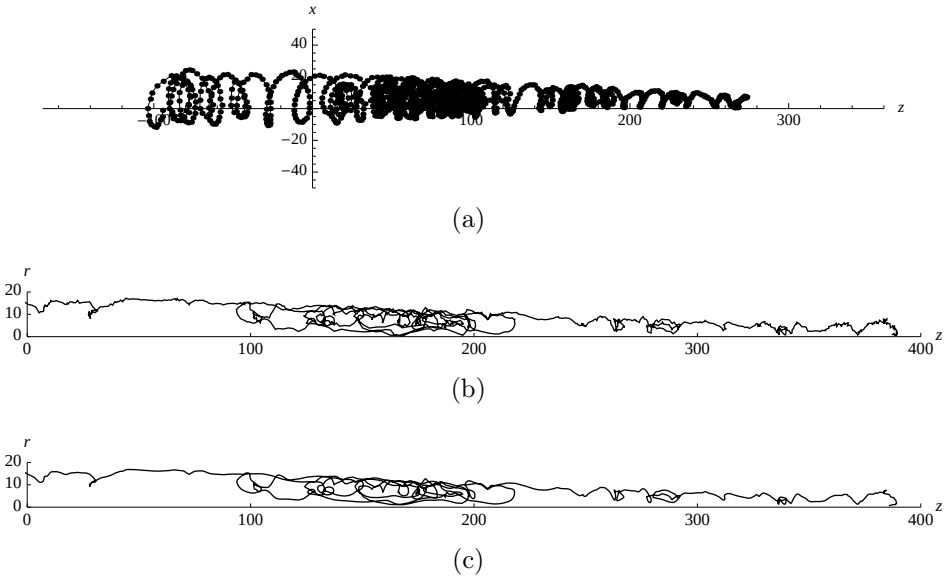

Figure A.9: In a) is the particle trajectory in alginate (15 cP) from experiment 9 with 5% underflow and a volume flow rate of 3.3 m^3h^{-1}, presented in Cartesian coordinates. In b) is the 2D-trajectory of the particle trajectory in experiment 9 presented and in c) the 2D-trajectory has been smoothed by Gaussian filter. Both b) and c) trajectories are presented in a cylindrical coordinate system.

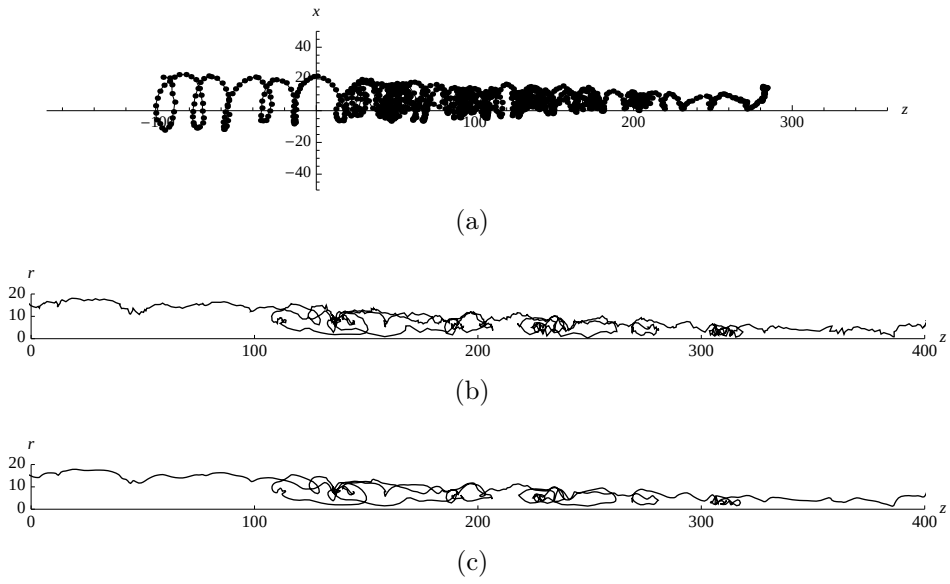

(a)

(b)

(c)

Figure A.10: In a) is the particle trajectory in alginate (15 cP) from experiment 10 with 10% underflow and a volume flow rate of 3.3 m^3h^{-1}, presented in Cartesian coordinates. In b) is the 2D-trajectory of the particle trajectory in experiment 10 presented and in c) the 2D-trajectory has been smoothed by Gaussian filter. Both b) and c) trajectories are presented in a cylindrical coordinate system.

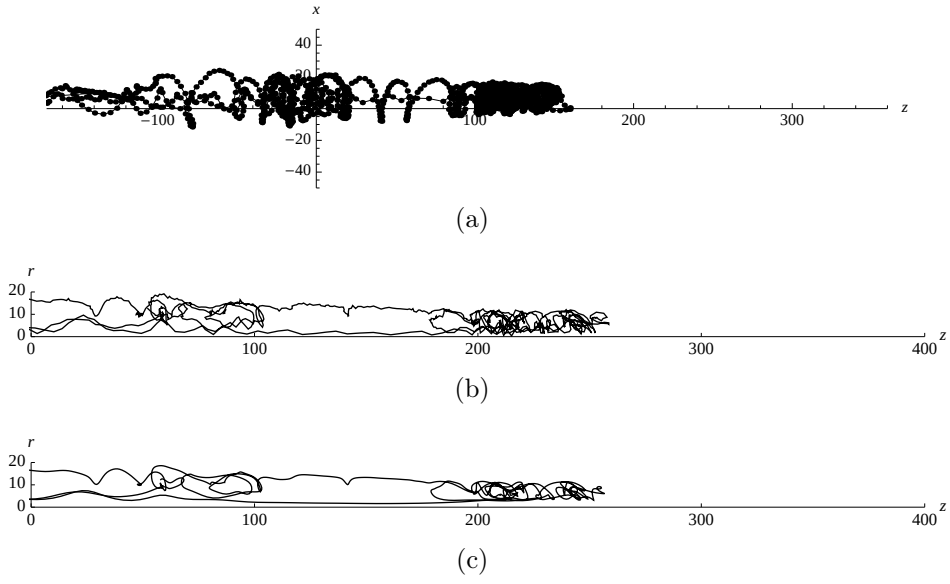

(a)

(b)

(c)

Figure A.11: In a) is the particle trajectory in alginate (15 cP) from experiment 11 with 0% underflow and a volume flow rate of 3.3 m^3h^{-1}, presented in Cartesian coordinates. In b) is the 2D-trajectory of the particle trajectory in experiment 11 presented and in c) the 2D-trajectory has been smoothed by Gaussian filter. Both b) and c) trajectories are presented in a cylindrical coordinate system. The particle exit through the overflow.

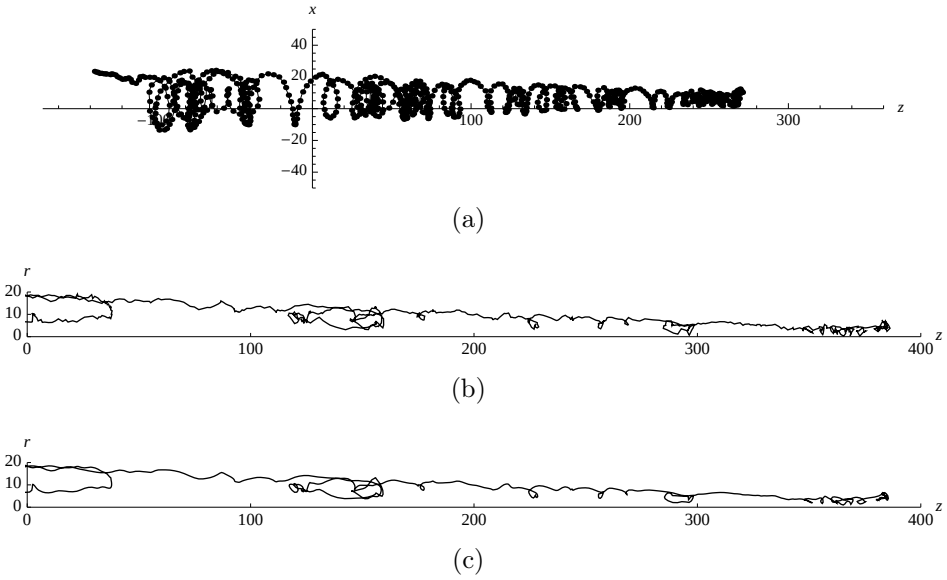

Figure A.12: In a) is the particle trajectory in alginate (10 cP) from experiment 12 with 5% underflow and a volume flow rate of 3.3 m^3h^{-1}, presented in Cartesian coordinates. In b) is the 2D-trajectory of the particle trajectory in experiment 12 presented and in c) the 2D-trajectory has been smoothed by Gaussian filter. Both b) and c) trajectories are presented in a cylindrical coordinate system.

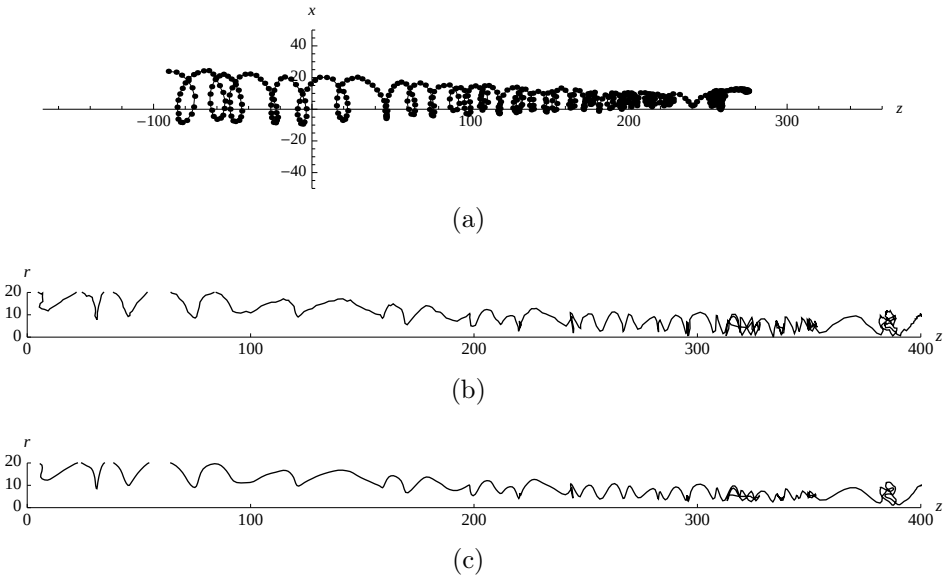

Figure A.13: In a) is the particle trajectory in alginate (5 cP) from experiment 13 with 5% underflow and a volume flow rate of 3.3 m^3h^{-1}, presented in Cartesian coordinates. In b) is the 2D-trajectory of the particle trajectory in experiment 13 presented and in c) the 2D-trajectory has been smoothed by Gaussian filter. Both b) and c) trajectories are presented in a cylindrical coordinate system.

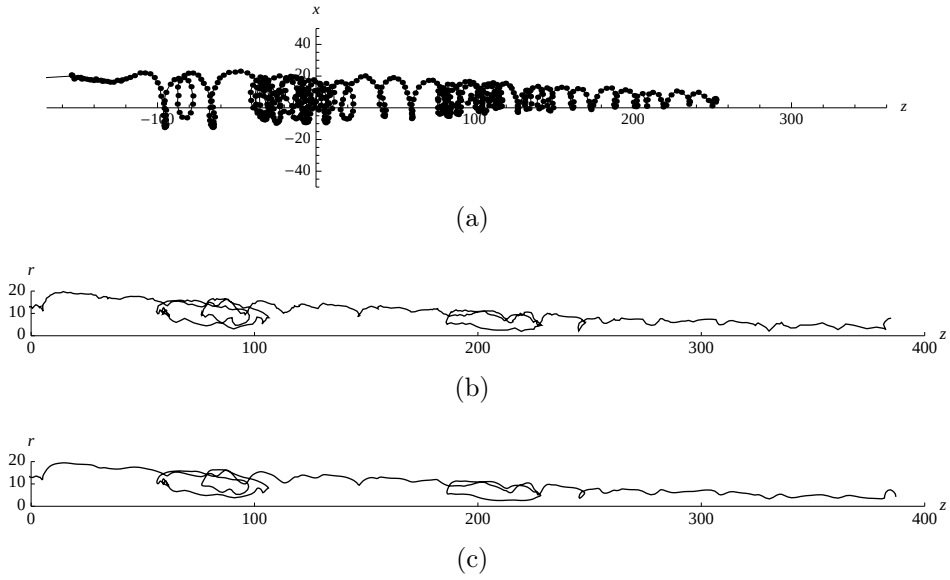

Figure A.14: In a) is the particle trajectory in alginate (5 cP) from experiment 14 with 10% underflow and a volume flow rate of 3.3 m^3h^{-1}, presented in Cartesian coordinates. In b) is the 2D-trajectory of the particle trajectory in experiment 14 presented and in c) the 2D-trajectory has been smoothed by Gaussian filter. Both b) and c) trajectories are presented in a cylindrical coordinate system.

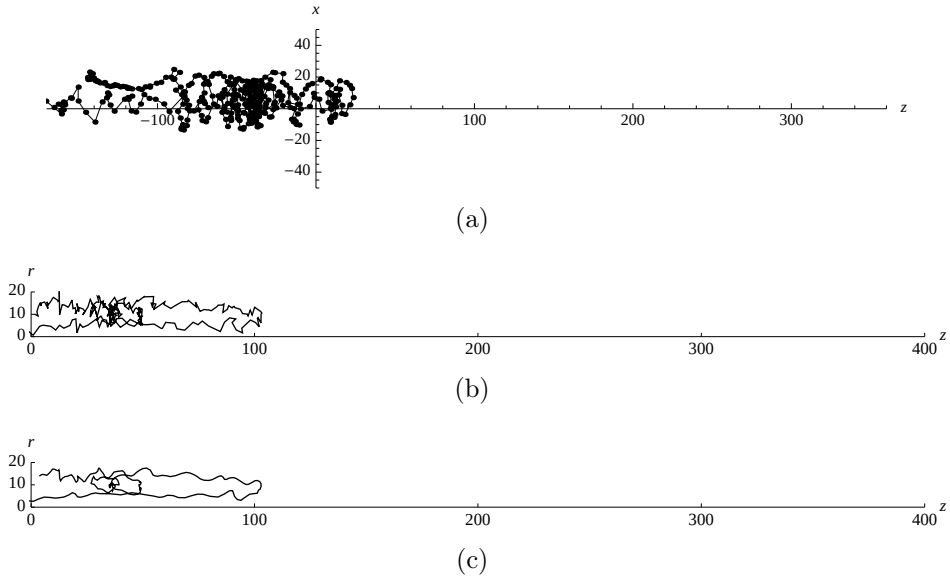

Figure A.15: In a) is the particle trajectory in a salt solution from experiment 15 with 5% underflow and a volume flow rate of 3.4 m^3h^{-1}, presented in Cartesian coordinates. In b) is the 2D-trajectory of the particle trajectory in experiment 15 presented and in c) the 2D-trajectory has been smoothed by Gaussian filter. Both b) and c) trajectories are presented in a cylindrical coordinate system. The particle exit through the overflow.

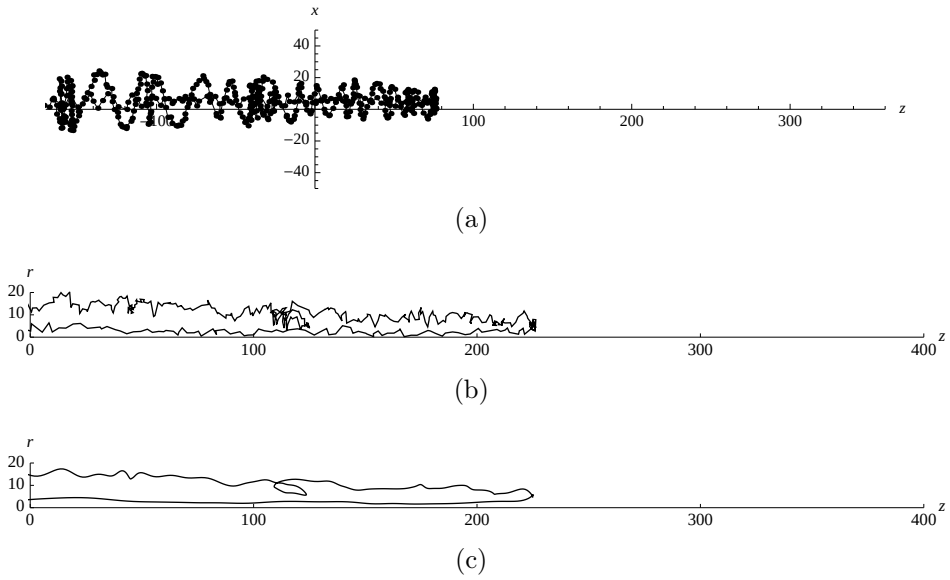

Figure A.16: In a) is the particle trajectory in a salt solution from experiment 16 with 5% underflow and a volume flow rate of 3.4 m^3h^{-1}, presented in Cartesian coordinates. In b) is the 2D-trajectory of the particle trajectory in experiment 16 presented and in c) the 2D-trajectory has been smoothed by Gaussian filter. Both b) and c) trajectories are presented in a cylindrical coordinate system. The particle exit through the overflow.

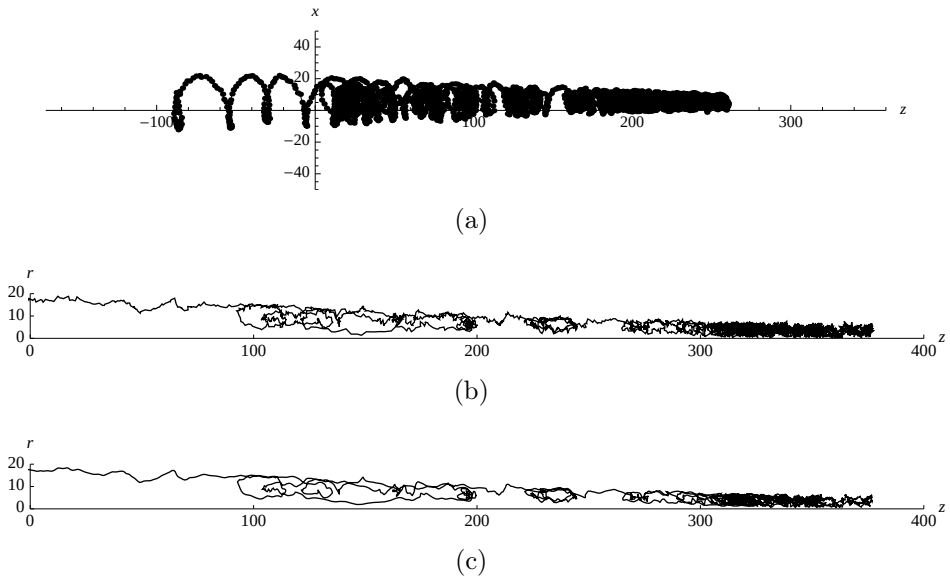

Figure A.17: In a) is the particle trajectory in water from experiment 17 with 0% underflow and a volume flow rate of 2.0 m^3h^{-1}, presented in Cartesian coordinates. In b) is the 2D-trajectory of the particle trajectory in experiment 17 presented and in c) the 2D-trajectory has been smoothed by Gaussian filter. Both b) and c) trajectories are presented in a cylindrical coordinate system. The EoV is present low in the conical section of the hydrocyclone

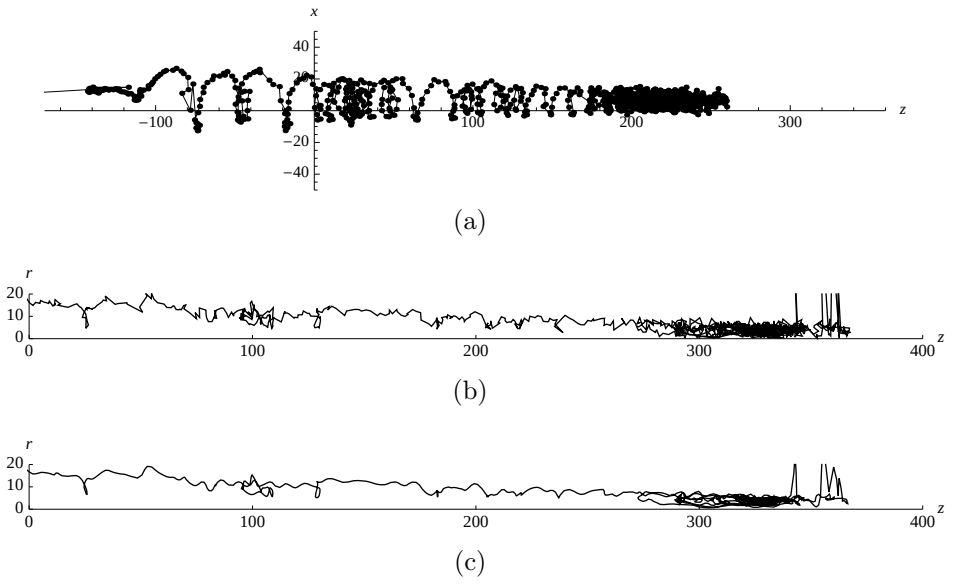

Figure A.18: In a) is the particle trajectory in water from experiment 18 with 0% underflow and a volume flow rate of 3.4 m^3h^{-1}, presented in Cartesian coordinates. In b) is the 2D-trajectory of the particle trajectory in experiment 18 presented and in c) the 2D-trajectory has been smoothed by Gaussian filter, both b) and c) trajectories are presented in a cylindrical coordinate system. The EoV is present low in the conical section of the hydrocyclone

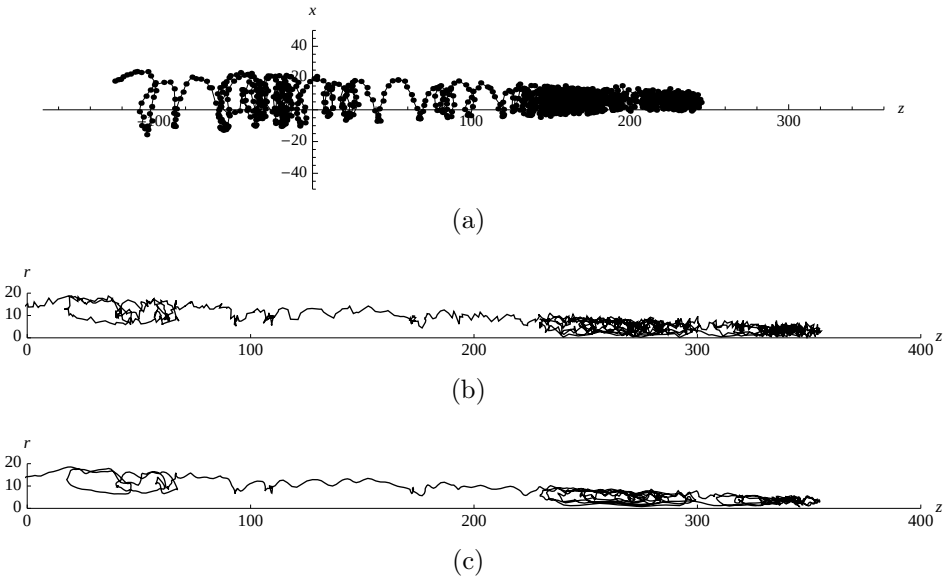

Figure A.19: In a) is the particle trajectory in water from experiment 19 with 0% underflow and a volume flow rate of 3.4 m^3h^{-1}, presented in Cartesian coordinates. In b) is the 2D-trajectory of the particle trajectory in experiment 19 presented and in c) the 2D-trajectory has been smoothed by Gaussian filter, both b) and c) trajectories are presented in a cylindrical coordinate system. The EoV is present low in the conical section of the hydrocyclone

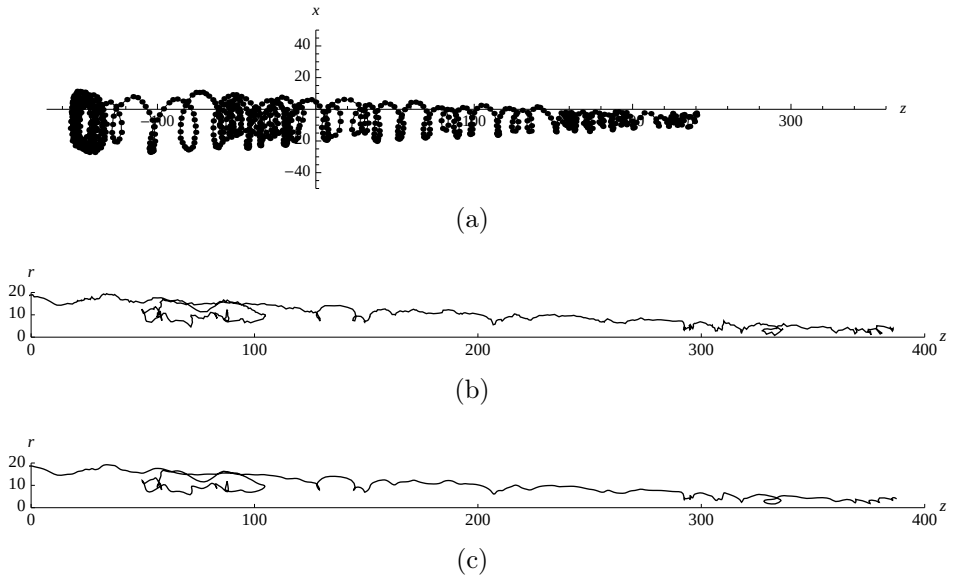

Figure A.20: In a) is the particle trajectory in water from experiment 20 with 5% underflow and a volume flow rate of 3.0 m^3h^{-1}, presented in Cartesian coordinates. In b) is the 2D-trajectory of the particle trajectory in experiment 20 presented and in c) the 2D-trajectory has been smoothed by Gaussian filter. Both b) and c) trajectories are presented in a cylindrical coordinate system

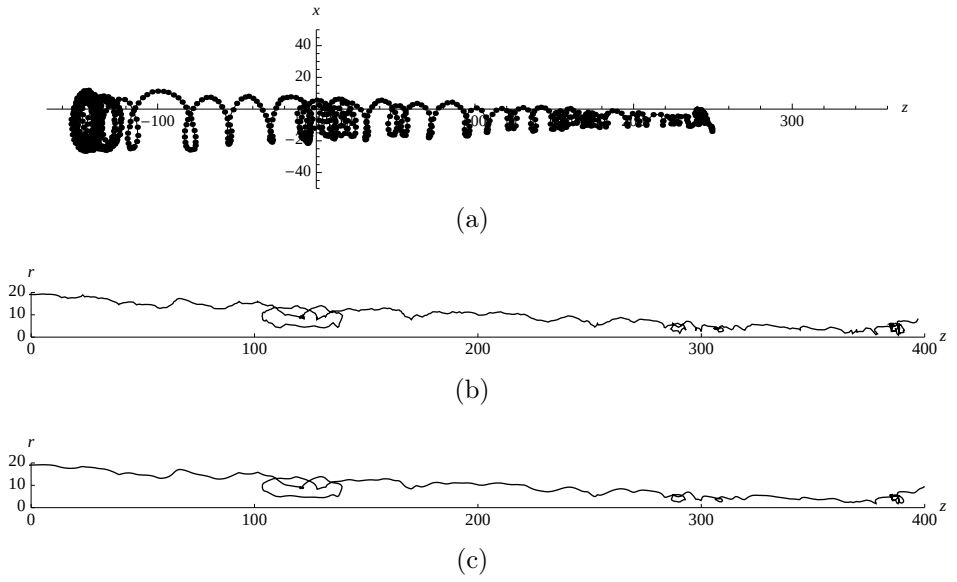

Figure A.21: In a) is the particle trajectory in water from experiment 21 with 10% underflow and a volume flow rate of 3.0 m^3h^{-1}, presented in Cartesian coordinates. In b) is the 2D-trajectory of the particle trajectory in experiment 21 presented and in c) the 2D-trajectory has been smoothed by Gaussian filter. Both b) and c) trajectories are presented in a cylindrical coordinate system

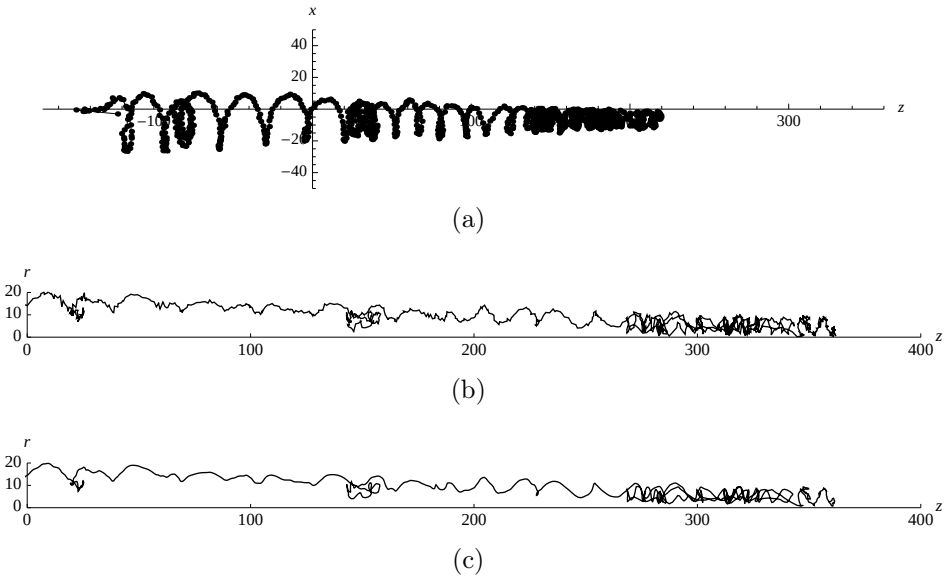

Figure A.22: In a) is the particle trajectory in water from experiment 22 with 0% underflow and a volume flow rate of 2.1 m^3h^{-1}, presented in Cartesian coordinates. In b) is the 2D-trajectory of the particle trajectory in experiment 22 presented and in c) the 2D-trajectory has been smoothed by Gaussian filter. Both b) and c) trajectories are presented in a cylindrical coordinate system. The EoV is present low in the conical section of the hydrocyclone

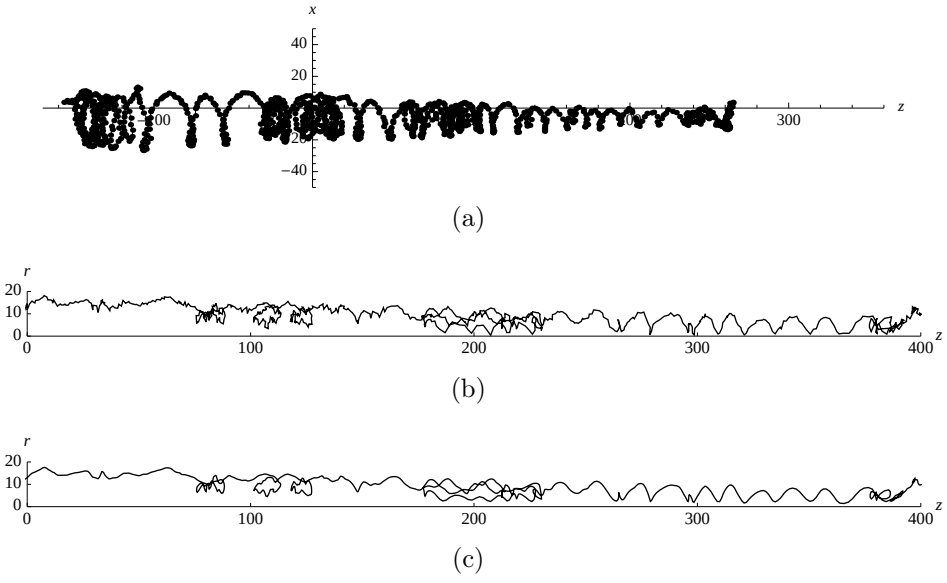

Figure A.23: In a) is the particle trajectory in water from experiment 23 with 10% underflow and a volume flow rate of 2.1 m^3h^{-1}, presented in Cartesian coordinates. In b) is the 2D-trajectory of the particle trajectory in experiment 23 presented and in c) the 2D-trajectory has been smoothed by Gaussian filter. Both b) and c) trajectories are presented in a cylindrical coordinate system.

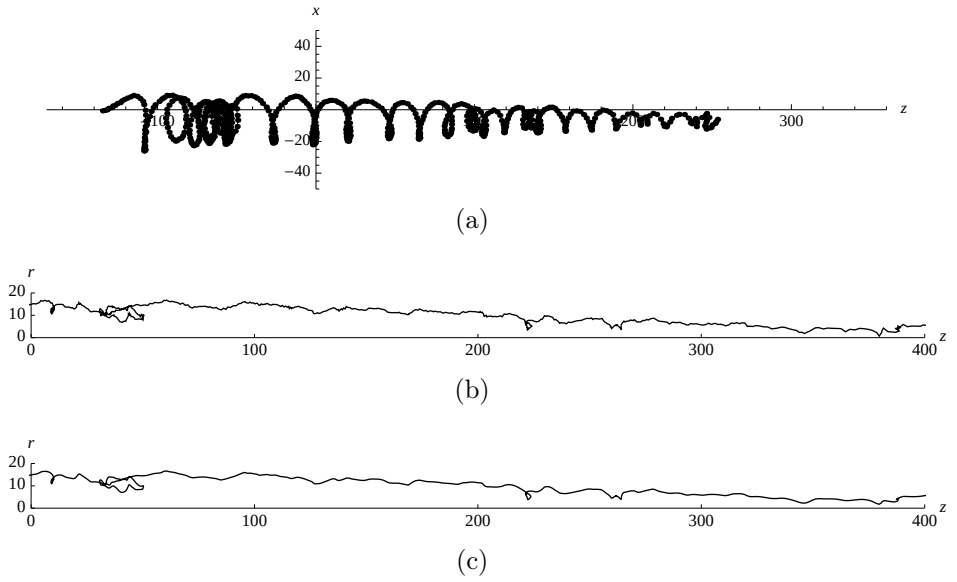

Figure A.24: In a) is the particle trajectory in water from experiment 24 with 24% underflow and a volume flow rate of 2.1 m^3h^{-1}, presented in Cartesian coordinates. In b) is the 2D-trajectory of the particle trajectory in experiment 24 presented and in c) the 2D-trajectory has been smoothed by Gaussian filter. Both b) and c) trajectories are presented in a cylindrical coordinate system.

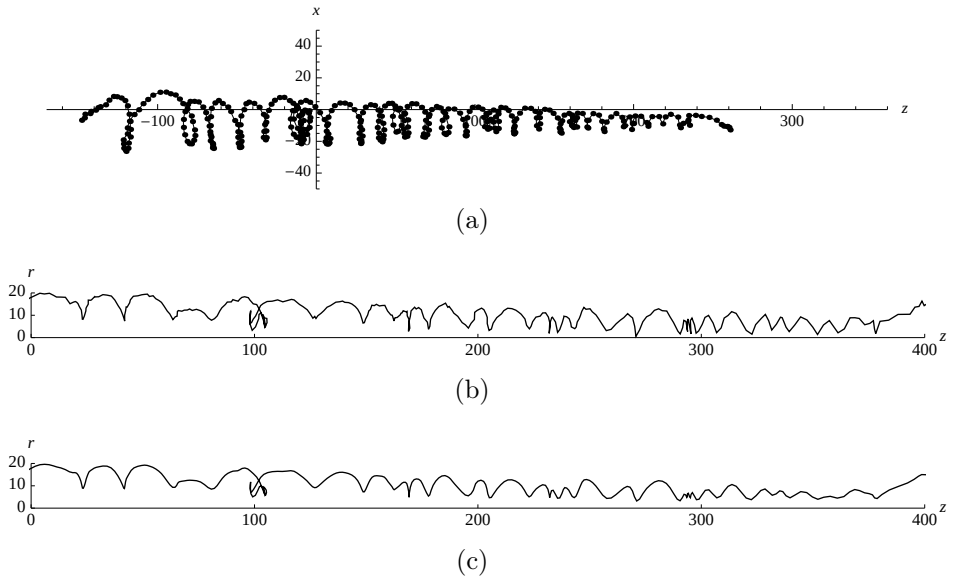

Figure A.25: In a) is the particle trajectory in water from experiment 25 with 22% underflow and a volume flow rate of 3.2 m^3h^{-1}, presented in Cartesian coordinates. In b) is the 2D-trajectory of the particle trajectory in experiment 25 presented and in c) the 2D-trajectory has been smoothed by Gaussian filter. Both b) and c) trajectories are presented in a cylindrical coordinate system.

Bibliography

[1] M. Ray, P. Luning, A. Hoffmann, A. Plomp, and M. Beumer, "Improving the removal efficiency of industrial-scale cyclones for particles smaller than five micrometre," *INTERNATIONAL JOURNAL OF MINERAL PROCESSING*, vol. 53, pp. 39–47, FEB 1998. Engineering-Foundation Conference on Particle Science and Technology in the 21st Century, TATA RES DEV DESIGN CTR, PUNE, INDIA, DEC 17-21, 1995.

[2] A. C. Hoffmann and L. E. Stein, *Gas Cyclones and Swirl Tubes: Principles, Design and Operation*. Berlin, Heidelberg: Springer-Verlag Berlin Heidelberg, second edition ed., 2008.

[3] L. Svarovsky, *Solid-liquid separation*. Oxford: Butterworth-Heinemann, 4th ed. ed., 2000.

[4] L. Svarovsky, *Solid-liquid separation processes and technology*. Amsterdam: Elsevier, 1985.

[5] Z. Stegowski and E. Nowak, "Radiotracer experiments and CFD simulation for industrial hydrocyclone performance," *NUKLEONIKA*, vol. 52, no. 3, pp. 115–123, 2007.

[6] J. Kang and A. Hayatdavoudi, "Analytical model determining the flow pattern and the distribution of d50 in a hydrocyclone," *Society of Petroleum Engineers*, 1985.

[7] R. M. Alexander, *Fundamentals of cyclone design and operation*, vol. 152-153. Proc. Australas. inst. Min. Metall, 1949.

[8] C. Cortés and A. Gil, "Modeling the gas and particle flow inside cyclone separators," *Progress in Energy and Combustion Science*, vol. 33, pp. 409–452, 10 2007.

[9] W. Peng, A. C. Hoffmann, P. J. A. J. Boot, A. Udding, H. W. A. Dries, A. Ekker, and J. Kater, "Flow pattern in reverse-flow centrifugal separators," *Powder Technology*, vol. 127, pp. 212–222, 11 2002.

[10] S. V. Alekseenko, P. A. Kuibin, and V. L. Okulov, *Theory of Concentrated Vortices: An Introduction*. Berlin, Heidelberg: Springer-Verlag Berlin Heidelberg, 2007.

[11] N. Rott, "On the viscous core of a line vortex," *Zeitschrift für Angewandte Mathematik und Physik (ZAMP)*, vol. 9, no. 5, pp. 543–553, 1958-03-01.

[12] D. Bradley, *The hydrocyclone*. Oxford: Pergamon Press, 1965.

[13] G. I. Pisarev, A. C. Hoffmann, W. Peng, and H. A. Dijkstra, "Large Eddy Simulation of the vortex end in reverse-flow centrifugal separators," *APPLIED MATHEMATICS AND COMPUTATION*, vol. 217, pp. 5016–5022, FEB 1 2011.

[14] S. K. Kawatra, A. K. Bakshi, and M. T. Rusesky, "Effect of viscosity on the cut (d50) size of hydrocyclone classifiers," *Minerals Engineering*, vol. 9, pp. 881–891, 8 1996.

[15] S.-A. Marthinusssen, "The effect of fluid viscosity on hydrocyclone performance; design and commissioning of an experimental rig and results," Master's thesis, University of Bergen, 2011.

[16] A. Hoekstra, J. Derksen, and H. Van Den Akker, "An experimental and numerical study of turbulent swirling flow in gas cyclones," *CHEMICAL ENGINEERING SCIENCE*, vol. 54, pp. 2055–2065, JUL 1999. 15th International Symposium on Chemical Reaction Engineering (ISCRE 15), NEWPORT BEACH, CA, SEP 13-16, 1998.

[17] W. L. McCabe, P. Harriott, and J. C. Smith, *Unit operations of chemical engineering.* Boston: McGraw-Hill, 7th ed. ed., c2005.

[18] T. J. Overcamp and S. E. Scarlett, "Effect of reynolds number on the stokes number of cyclones," *Aerosol Science and Technology*, vol. 19, no. 3, pp. 362–370, 1993.

[19] G. B. Saha, *Fundamentals of nuclear pharmacy.* New York: Springer, 6th ed. ed., c2010.

[20] D. L. Bailey, *Positron emission tomography: basic sciences.* London: Springer, c2005.

[21] Y. F. Chang, C. G. Ilea, Ø. L. Aasen, and A. C. Hoffmann, "Particle flow in a hydrocyclone investigated by positron emission particle tracking," *Chemical Engineering Science*, vol. 66, pp. 4203–4211, 9 2011.

[22] D. J. Parker, L. T. W, H. M. N. Fan X, I. A, and Z. Yang, "Positron imaging techniques for process engineering: recent developments at birmingham," *MEASUREMENT SCIENCE AND TECHNOLOGY*, vol. 19, SEP 2008.

[23] D. J. Parker and X. Fan, "Positron emission particle tracking - Application and labelling techniques," *PARTICUOLOGY*, vol. 6, pp. 16–23, FEB 2008. UK-China Particle Technology Forum, Leeds, ENGLAND, APR 01-03, 2007.

[24] A. C. H. et al, "Pet investigation of a fluidized particle: spatial and temporal resolution and short term motion," *Measurement Science and Technology*, vol. 16, no. 3, 2005.

[25] Z. Yang, P. J. Fryer, S. Bakalis, X. Fan, D. J. Parker, and J. P. K. Seville, "An improved algorithm for tracking multiple, freely moving particles in a positron emission particle tracking system," *Nuclear Instruments and Methods in Physics Research Section A: Accelerators, Spectrometers, Detectors and Associated Equipment*, vol. 577, pp. 585–594, 7 2007.

[26] Z.-B. Wang, L.-Y. Chu, W.-M. Chen, and S.-G. Wang, "Experimental investigation of the motion trajectory of solid particles inside the hydrocyclone by a Lagrange method," *CHEMICAL ENGINEERING JOURNAL*, vol. 138, pp. 1–9, MAY 1 2008.

[27] L. P. M. Marins, D. G. Duarte, J. B. R. Loureiro, C. A. C. Moraes, and A. P. Silva Freire, "LDA and PIV characterization of the flow in a hydrocyclone without an air-core," *JOURNAL OF PETROLEUM SCIENCE AND ENGINEERING*, vol. 70, pp. 168–176, FEB 2010.

[28] M. A. Z. Coelho and R. A. Medronho, "A model for performance prediction of hydrocyclones," *Chemical Engineering Journal*, vol. 84, pp. 7–14, 9 2001.

[29] A. C. Hoffmann, R. de Jonge, H. Arends, and C. Hanrats, "Evidence of the 'natural vortex length'and its effect on the separation efficiency of gas cyclones," *Filtration & Separation*, vol. 32, pp. 799–804, 9 1995.

[30] J. Severino, L. Gomez, S. Wang, R. Mohan, and O. Shoham, "Mechanistic modeling of solids separation in solid/liquid hydrocyclones," *SPE Projects, Facilities and Construction*, vol. 5, pp. 121–135, September 2010.

[31] M. A. Hararah, E. Endres, J. Dueck, L. Minkov, and T. Neesse, "Flow conditions in the air core of the hydrocyclone," *MINERALS ENGINEERING*, vol. 23, pp. 295–300, MAR 2010.

[32] D. J. Parker, T. W. Leadbeater, X. Fan, M. N. Hausard, A. Ingram, and Z. Yang, "Positron emission particle tracking using a modular positron camera," *Nuclear Instruments and Methods in Physics Research Section A: Accelerators, Spectrometers, Detectors and Associated Equipment*, vol. 604, pp. 339–342, 6 2009.

[33] C. W. Chan, J. Seville, X. Fan, and J. Baeyens, "Solid particle motion in a standpipe as observed by positron emission particle tracking," *Powder Technology*, vol. 194, pp. 58–66, 8 2009.

[34] T. W. Leadbeater and D. J. Parker, "A modular positron camera for the study of industrial processes," *NUCLEAR INSTRUMENTS AND METHODS IN PHYSICS RESEARCH SECTION A-ACCELERATORS SPECTROMETERS DETECTORS AND ASSOCIATED EQUIPMENT*, vol. 652, pp. 646–649, OCT 1 2011.

[35] C. Chan, J. Seville, X. Fan, and J. Baeyens, "Particle motion in cfb cyclones as observed by positron emission particle tracking," *Industrial and Engineering Chemistry Research*, vol. 48/1, 2009.

[36] J. J. Derksen, "Simulations of confined turbulent vortex flow," *Computers & Fluids*, vol. 34, pp. 301–318, 3 2005.

[37] R. Hreiz, C. Gentric, and N. Midoux, "Numerical investigation of swirling flow in cylindrical cyclones," *Chemical Engineering Research and Design*, no. 0, pp. –, 2011.

[38] H. C. Strutt, S. W. Tullis, and M. F. Lightstone, "Numerical methods for particle-laden dns of homogeneous isotropic turbulence," *Computers & Fluids*, vol. 40, pp. 210–220, 1 2011.

[39] G. I. Pisarev and A. C. Hoffmann, "Effect of the 'end of the vortex'phenomenon on the particle motion and separation in a swirl tube separator," *Powder Technology*, vol. 222, pp. 101–107, 5 2012.

[40] A. Raoufi, M. Shams, M. Farzaneh, and R. Ebrahimi, "Numerical simulation and optimization of fluid flow in cyclone vortex finder," *Chemical Engineering and Processing: Process Intensification*, vol. 47, pp. 128–137, 1 2008.

[41] K. U. Bhaskar, Y. R. Murthy, M. R. Raju, S. Tiwari, J. K. Srivastava, and N. Ramakrishnan, "Cfd simulation and experimental validation studies on hydrocyclone," *Minerals Engineering*, vol. 20, pp. 60–71, 1 2007.

[42] G. I. Pisarev, V. Gjerde, B. V. Balakin, A. C. Hoffmann, H. A. Dijkstra, and W. Peng, "Experimental and computational study of the "end of the vortex"phenomenon in reverse-flow centrifugal separators," *AIChE Journal*, pp. n/a–n/a, 2011.

[43] J. P. Bentley, *Principles of Measurement Systems*. Essex, England: Pearson Education Limited, fourth ed., 2005.

[44] D. G. Fonnes, "Investigation of particle trajectories in hydrocyclones using positron emission tomography and numerical simulations," Master's thesis, University of Bergen, 2011.

[45] R. Haddad and A. Akansu, "A class of fast gaussian binomial filters for speech and image processing," *Signal Processing, IEEE Transactions on*, vol. 39, pp. 723 –727, mar 1991.

[46] J. D. Anderson, *Computational fluid dynamics: the basics with applications*. New York: McGraw-Hill, c1995.

[47] C. Crowe, M. Sommerfield, and Y. Tsuji, *Multiphase Flows with Droplets and Particles*. Boca Rato, Florida: CRC Press, first edition ed., 1998.